Molecular Dynamics (MD) Studies on Phase Transformation and Deformation Behaviors in FCC Metals and Alloys

Thesis by

Yue Qi

In Partial Fulfillment of the Requirement

for the Degree of

Doctor of Philosophy

California Institute of Technology

Pasadena, California

2001

(Submitted April 27th, 2001)

To My parents, Jinjiang Li

&

my son to be born

Acknowledgement

I would like to thank my advisor Professor William A. Goddard III, for his support, encouragement, and guidance, for the trust and freedom he gave me during my graduate work, and for being an extremely fine example of intellectual integrity, creativity, enthusiasm and dedication to science. For the first time, I was told to think as a scientist (by Bill), which enlightened and still will enlighten my life and career.

I also want to thank Professor William L. Johnson. I appreciate the fabulous scientific discussions we have had. He always has brilliant ideas and interpretations about our simulation results, from both experimentalist and theorist points of view. Both Bills have made science fun for me.

My special thanks also go to Tahir Cagin, for being a mentor and a friend, for helping overcome the struggling time, for advice on science and life. I would like to thank Professor Brent Fultz, Harry Atwater, and Michael Ortiz for reading my thesis and being in my committee. I would like to thank everyone in Goddard and Johnson's group for their scientific support and friendship. In particular, Ysitaka Kimura, Hideyuki Ikeda, Konrad Samwer, Alejandro Strachan, Hyon-jee Lee, Guofeng Wang, Darry L. Willick, Nagarajan Vaidehi, Jianwei Che, etc.

Last, I delicate this thesis to my parents, my husband and son to be born. I would like to express my gratitude and my appreciation to my husband, Jinjiang Li, for his love, support, encouragement, and for giving me a happy and complete life. I also dedicate this thesis to my son to be born. It's such an excitement to feel his kicking inside while I am writing this thesis.

Abstract

This thesis focused on the phase transformation and deformation in face center cubic (FCC) metals and alloys. These studies use the new quantum modified Sutton-Chen (QMSC) many-body potentials for Cu, Ni, Ag, and Au and for their alloys through simple combination rules. Various systems and processes are simulated by standard equilibrium molecular dynamics (MD), quasi-static equilibrium MD and non-equilibrium MD (NEMD), cooperated with different periodic boundary conditions. The main topics and their outlines are listed as the following:

1) Melting, glass formation, and crystallization processes in bulk alloys: Using cooling rates in the range of $2*10^{12}$ to $4*10^{14}$ K/s, we find that CuNi and pure Cu always form an FCC crystal while Cu_4Ag_6 always forms a glass (with Tg decreasing as the quench rate increases), which confirms the role of size mismatch in glass formability and validates the accuracy of the force field.
2) The size effects in melting and crystallization in Ni nano clusters, ranging 100 to 8007 atoms: We find a transition from cluster or molecular behavior below ~500 atoms to a mesoscale nanocrystal regime (with well-defined bulk and surface properties and surface melting processes, which leads to $T_{m,N} = T_{m,bulk} - \alpha N^{-1/3}$) above ~750 atoms. Cooling from the melt leads first to supercooled clusters with icosahedral local structure, then for N>500 the supercooled clusters transform to FCC grains, while clusters with N<500 form icosahedral structures.
3) The deformation behavior of metallic nanowires of pure Ni, NiCu and NiAu alloys, under high rates of uniaxial tensile strain, ranging from $5*10^8$/s to

$5*10^{10}$/s: These nanowires are too small to sustain dislocations; instead we find that deformation proceeds through twinning and coherent slipping mechanisms at low strain rate, and amorphization at high strain rate. We find that critical strain rate, beyond which the crystal transformed into glassy state, for NiAu (13% size mismatch) is 100 times slower than that for NiCu (2.5% size mismatch). Thus the critical strain rate also depends on the glass formability.

4) The calculation of the ½<110> screw dislocation in nickel (Ni): From a quadrupolar dislocation system with 3-D periodic boundary conditions, we found the screw dislocation dissociated into two partials on {111} planes, and the core energy is 0.5 eV/b. We also studied motion and annihilation process of opposite signed dislocations with different configurations of dissociation planes. On two intersecting or parallel dissociation planes, a cross-slip process is captured and the energy barriers is 0.1eV/b in our simulations.

5) Friction Anisotropy at Ni(100)/(100) interface: We carried out a series of NEMD simulations for sliding of Ni(100) interfaces under a constant force. We found that the clean, flat, and incommensurate interface has a very small static friction coefficient, as analytical theory predicted. However surface roughness can increase the static friction on the incommensurate interfaces dramatically, and increase the friction on the commensurate interfaces to a lesser extend. The dynamic frictional coefficients are comparable to the experimental values and show the same anisotropic behavior, thus explain the difference between theory and experiment.

Table of Contents

Chapter 1 Introduction

1.1 Why simulations of metals and alloys?

Humans started to use alloys from Bronze and Iron Ages, thousands of years before the modern materials scientist understood the macro and micro structures of the materials. There are two dimensions in materials science, length and time scale. The relaxation times associate with the various chemical and physical processes operating at the material's differing structural length scales, such that a material's structure and properties depend on how it was made and what conditions it endured in service.[1-1]

The materials design approach is a powerful logical structure connecting processing, structure, properties, and technological performance. The system-driven computational design approach will save the cost of discovery, by using computers to design, characterize, and optimize materials before beginning the expensive experimental processes of synthesis, characterization, processing, assembly, and testing. This will not be dream anymore, while theories quantum mechanics, molecular dynamics, statistical mechanics and continuum theory will properly incorporate on various length and time scales to design new alloys or other new materials.

This thesis will focus on two basic materials' science problems, phase transformation and plastic deformations, in some metal and alloys systems, such as Ni, Cu, NiCu, CuAg, NiAu. We used a realistic potential to describe the interactions between atoms and state of art molecular dynamics to simulate various processes,

such as heating and cooling, tensile testing, sliding, etc. These studies will show how atomic simulation related to properties at macro scale, how atomic simulation bridges quantum and continuum theory, and how properties at nano scale differ from bulk systems.

1.2 Molecular dynamics simulations

By averaging over the electron wave functions to obtain parameters for a potential, which only depends on the atomic positions, quantum mechanics can be approximated with molecular dynamics, which solves Newtonian equations rather than *Schrödinger* equations, to predict the motions of systems ranging from hundreds to millions of atoms. Such atomistic simulation of structure, energy, physical and chemical properties of atomic and molecular systems provides a straightforward, reliable and accessible method for many investigations in materials sciences, biotechnology, chemical technology and nanotechnology. [1-2]

In chapter 2 we shall give a brief introduction of the simulation methods, such as the accurate force field, molecular dynamics techniques, and computation of physical properties. These methods are the fundamentals of the processing simulations in this thesis. However, many important problems require explicit treatment of 10^5~10^7 atoms. These problems include the grain boundary, dislocation, cracks, void, vacancy, and other defects, which are critical to understand the plastic behavior and mechanical properties of solid; the shock wave propagation and phase transition during shock, high speed impact and spallation; and shear band formation in metallic glasses. All these problems require to model ever-increasing system sizes, at least

millions of atoms, which is beyond the capacity of any single computer available currently. To solve these problems, a massively parallel simulation program (MPiSIM), paralleled by message passing interface (MPI), is developed. This general molecular dynamics simulation tool is designed to handle systems range 10^3~10^7 of atoms by taking advantage of distributed computer architectures. It has shown good scaling performance over simulation size and processors in use, portability on various platforms and expandability to other MD methods and atomic potentials [1-3].

It's now routine to carry out MD simulations on a system, since it's well development during 80^{th}. However, how to creatively construct the suitable models and apply simple MD methods to simulate various processes are still the main challenges for simulation work. In this thesis, various applications cover simulations of heating and cooling processes [1-4], where a series of TtN or ThN MD were carried out as a function of temperature, constant uniaxial strain rate tensile tests [1-5], where a quasi-equilibrium MD were performed to enable the system to have certain time to respond to the applied strain, and friction process, where a pair of opposite signed constant force were applied to upper and lower level of two objects [1-6], leading to non-equilibrium MD (MEMD) simulation.

A classical MD simulation proceeds by constructing a finite model system with N atoms in any configuration (crystal or amorphous) in a primary computational cell. The cell is replicated in all spatial dimensions generating its own periodic images. This method is the periodic boundary condition (PBC), and it is introduced to remove the undesirable effects of the artificial surface associated with the finite size of the simulation system. For example, to use 500 atoms with 3D PBC to model a bulk

system, either in crystal phase or amorphous state. And another example is the dislocation study, since the interaction between the dislocation and the surface is long range, to eliminate the surface effects, we constructed dislocation dipole and quadrupole in the simulation cell, to have zero displaced atoms on the boundary then use periodic boundary condition [1-7]. However, to simulate structures at nano-scale, the surface effects cannot be ignored. So we have used 2-D PBC for thin film, 1-D PBC for nano-wire and no-PBC for cluster with free surface. The surface effects cause the behavior of nano-clusters to change dramatically from a bulk system, as discussed in chapter 4 [1-8].

1.3 Phase transformations

The crystallization will always occur in equilibrium solidification; however, if the homogenous nucleation of crystals in the undercooled liquid melt is prevented on laboratory time scale, a metastable glassy phase can form. It's well known that this glass phase can be obtained either from a liquid or a gas phase by fast quenching, which reduces the atomic mobility so as to prevent nucleation and growth of crystal phase. For this reason, the glass transformation is system and rate dependent [1-9]. In chapter 3, we study the traditional melting, glass formation, and crystallization processes in metal alloys in bulk alloys. These studies use the new quantum Sutton-Chen (QMSC) many-body potentials for Cu, Ni, and Ag to examine the Cu_4Ag_6 and CuNi alloys. Using cooling rates in the range of $2*10^{12}$ to $4*10^{14}$ K/s, we find that CuNi and pure Cu always form a face-centered cubic (FCC) crystal while Cu_4Ag_6 always forms a glass (with Tg decreasing as the quench rate increases). The crystal

formers have radius ratios of 1.025 (CuNi) and 1.00 (Cu) while the glass former (CuAg) has a ratio of 1.13, confirming the role of size mismatch in biasing toward glass formation. These studies also show the accuracy of the force field to describe the liquid phase and different alloys, even though the force field is developed based on pure metal properties under very low temperature.

Crystallization requires the liquid to undergo supper-cooled region for nucleation; on the contrary, its reverse process, melting, doesn't need super heating and it's even harder to obtain supper-heated solid, since surface is an existing defect for melting to start [1-10]. When the size of a material reaches nano scale, the large surface and volume ratio will change a lot of behavior of phase transformation compared to bulk material. Most experiments were conducted at nanometer scale [1-11][1-12], where the analysis is based on thermodynamics theory, while simulation work focuses on hundreds of atoms, where the molecular behavior and stable structure for each size were studied [1-13]; however, no study has bridged these two regimes. In chapter 4, we investigated the surface effects in melting and crystallization by studying phase transitions in Ni nano clusters, ranging from hundred atoms up to 8007 atoms (5.7 nm). We find a transition from cluster or molecular behavior below ~500 atoms to a mesoscale nanocrystal regime (well-defined bulk and surface properties) above ~750 atoms (2.7 nm). We find that the mesoscale nanocrystals melt via surface processes, leading to $T_{m,N} = T_{m,bulk} - \alpha N^{-1/3}$, dropping from $T_{m,bulk}$ =1760K to $T_{m,336}$ = 980K. Cooling from the melt leads first to supercooled clusters with icosahedral local structure. For N > 500 the supercooled clusters transform to FCC grains, but smaller values of N lead to a glassy structure with substantial icosahedral character.

Generally the strategy for forming amorphous metals involves alloying with elements that are dissimilar in size and bonding (chemical disorder) or by introducing various defects [1-14] followed by sufficiently rapid decreases in the temperature that there is no time for crystal nuclei to form. In contrast to these processes, under high strain rate, where the atoms don't have time to relax to form the stable structure, including dislocation, twinning, and other plastic deformed structure, a disordered structure, amorphous, can be formed. Indeed we found that a homogenous perfect crystalline nanowire at constant temperature can be transformed continuously to an amorphous metal by application of sufficiently large strain rates in chapter 5. The critical strain rate at which the "nanowire crystals" flow like a "liquid" depends on the amorphous formability of the alloy. Such that, since NiAu has a 13% size mismatch whereas NiCu only 2.5%, the critical strain rate for NiCu is100 times larger than that for NiAu. We also calculated the elastic constants at each strain state for all strain rates to identify the relation between mechanical "shear" instability and deformation process. Thus there are now three orthogonal processes for forming amorphous metals: rapid quenching from a liquid, introduction of chemical or physical disorder, and application of rapid strain rates.

1.4 Deformations

Due to the time and size scale of atomic MD simulations, we can obtain the detailed microscopic information which can or cannot be obtained experimentally, such as deformation of nano-systems under extreme conditions. Such high strain rate is comparable to shock load/impact conditions [1-15]. Unfortunately, experiments

under these conditions tend to have many factors all playing roles simultaneously, whereas simulations can separate these effects. In chapter 5, we used quasi-static equilibrium molecular dynamics methods to study the deformation behavior of metallic nanowires of pure Cu, NiCu and NiAu alloys, under high rates of uniaxial tensile strain, ranging from $5*10^8$/s to $5*10^{10}$/s. These nanowires are only 2 nm thick and hence cannot sustain dislocations; instead we found that deformation proceeds through twinning and coherent slipping mechanisms at low strain rate, and amorphization at high strain rate.

The nano-wire system is too small to accommodate any dislocations; However, the mechanical properties of materials are governed by dislocation motion [1-17], which needs multi-scale simulation. At atomic level, we studied the energy and detail annihilation processes of dislocation in FCC metals, which will be used in the dislocation dynamics and continuum theory. In chapter 6, we have studied the ½a<110> screw dislocation in nickel (Ni). The relaxed structures show dissociation into two partials on {111} planes. The equilibrium separation distance between the two partials is 2.5 nm, which is larger than the derived value according to experimental data, due to low stacking fault energy given by the QMSC force field. From our calculations the core energy for the ½<110> screw dislocation is 0.5 eV/b, and the core structure is planar. We found the annihilation process of opposite signed dislocations greatly depends on the configurations of dissociation planes: same slip plane, intersecting slip planes and parallel slip planes. The process of cross-slip and associated energy barriers are also calculated from these simulations.

Simulations should not only reproduce the experiments and provide the numbers, but to help us understand the physics. A good example of how atomic simulation contributes to the theory of friction is given in chapter 7. The origin of friction comes from the atomic interaction at interfaces. Analytic theories indicated that there is no static friction on clean incommensurate interfaces [1-18][1-19], while a recent experiment revealed that the static friction coefficient was anisotropic with respect to the lattice orientation, but did not vanish on two clean Ni(100) mis-orientated surfaces [1-20]. To understand this friction anisotropy and the difference between theory and experiment, we carried out a series of Non Equilibrium Molecular Dynamics (NEMD) simulations for sliding of Ni(100) interfaces under a constant force. We found that the clean, flat, and incommensurate interface indeed has a very small static friction coefficient. Surface roughness can increase the static friction on the incommensurate interfaces dramatically and increase, to a lesser extent, the friction on the commensurate interfaces. The dynamic frictional coefficients are comparable to the experimental values as that observed in experiments for the $\theta=0°$ and the $\theta=45°$ orientated interfaces, and show the same anisotropic behavior.

References:

[1-1] G. B. Olson, Science, Science **288**, 993 (2000)

[1-2] M. P. Allen and D. J. Tildesley, Computer Simulation of Liquids (Oxford, 1987)

[1-3] Y. Qi, T. Cagin and W. A. Goddard III, Computer Aided Materials Design, submitted

[1-4] Y. Qi, T. Cagin, Y. Kimura and W. A. Goddard, III. Phys. Rev. B **59**, 3527-3533 (1999)

[1-5] H. Ikeda, Y. Qi, T. Cagin, K. Samwer, W.L. Johnson and W. A. Goddard III, Phys. Rev. Lett. **82**, 2900-2903 (1999)

[1-6] Y. Qi, T. Cagin, Y-T. Cheng and W. A. Goddard III, in preparation.

[1-7] Y. Qi, A. Strachan, T. Cagin and W. A. Goddard III, Mat. Sci. and Eng. A, **309**, 156 (2001)

[1-8] Y. Qi, T. Cagin, W. L. Johnson and W. A. Goddard, J. Chem. Phys. accepted.

[1-9] "Metallic Glasses" American Society for Metals, Metals Park, Ohio, (1978)

[1-10] P. Buffat and J-P Borel, Phys. Rev. A **13**, 2287 (1976)

[1-11] S. L. Lai, J. Y. Guo, V. Petrova, G. Ramanath and L. H. Allen, Phys. Rev. Lett. **77**, 99 (1996)

[1-12] T. Bachels and H.J. Guntherodt, Phys. Rev. Lett. **85**,1250 (2000)

[1-13] C. L. Cleveland, W. D. Luedtke and U. Landman, Phy. Rev. B **60**, 5065 (1999) and C. L. Cleveland and U. Landman, J. Chem. Phys. **94**, 7376 (1991)

[1-14] K. Samwer, H. Fecht and W. L. Johnson in "Glassy Metals III" ed. by H. Beck and H.J. Guntherodt (Springer, Berlin 1994)

[1-15] G.T. Gray III, Acta. Met. **36**, 1745 (1988)

[1-16] T.H. Blewitt, R.R. Coltman and J.K. Redman, J. Appl. Phys. **28**, 651 (1957)

[1-17] John P. Hirth and Jens Lothe, Theory of Dislocations, 2nd Edition, Krieger Publishing Company, Malabar (1982)

[1-18] Y. I. Frenkel and T. Kontorova, *Zh. Eksp. Teor. Fiz.* **8**, 1340 (1938) and K. Shinjo and M. Hirano, *Surf. Sci.*, **283**, 473 (1993)

[1-19] M. O. Robbins and E. D. Smith, Langmuir, **12**, 4543, (1996)

[1-20] J. S. Ko and A. J. Gellman, Langmuir **16**; 8343 (2000)

Chapter 2 Molecular Dynamics Simulation Methods

2.1 Introduction

Computer simulation has been extensively used in the last several decades and is becoming an indispensable part of scientific research. Computer simulations can provide linkage between microscopic and macroscopic properties for any system, and it helps us to understand experiments in different ways. We could calculate the response of the system in order to compare to the experimental observed values thereby checking the validity of the potential and methods employed to describe the system. Or we could calculate the response of the system in lieu of performing experiments; that is we could simulate the system under conditions where experiments have not been performed or cannot be performed easily. We also can obtain the detailed microscopic information which cannot be obtained experimentally and which may be helpful in constructing theories and in understanding experimental results. Among various simulation methods, molecular dynamics (MD) is one of the most widely used simulation methods for studying the properties of liquid, solids and molecules [2-1]. In MD simulation, the motion of individual atoms within an assembly of N atoms or molecules is modeled on the basis of either Newtonian deterministic dynamics or a Langevin-type stochastic dynamics, given their initial positions and velocities.

As the computer gets more powerful today and more accurate inter atomic potentials were developed, modeling of more realistic and more complicated system becomes possible. General materials always contain defects, such as grain boundary,

dislocation, cracks, void, vacancy, impurities, etc. To study these materials requires to model ever-increasing system sizes, at least millions of atoms, which is beyond the capacity of current computer facilities. While massively parallel (MP) computing hardware got improved in last 10 years, it also requires that the development of new parallel algorithms for simulation methods.

In this chapter, we'll first discuss the accurate force field development for some FCC metals, the fundamentals of molecular dynamics on various ensembles, and the calculation methods of some important physical quantities. Then a new parallel algorithm of MD simulation on distributed memory machine will be described.

2.2 Potential and parameters

The foundation of MD simulation is to use an inter-atomic potential, which contains the physics of the model system, to calculate the energetics and dynamics of a system. The significance and the accuracy of the simulation results, and the extent to which they represent the real behavior of the system, depend critically on a realistic choice of a potential energy function.

To describe the interactions between atoms accurately, we used a quantum effects modified Sutton-Chen type of many-body potential (QMSC) for FCC metals and alloys in our simulation. This force field has a similar electron density term, like embedded-atom method (EAM), which was developed by Daw and Baskes [2-2]. EAM is proposed based on density functional theory, and provides a new means of calculating ground state properties of realistic systems. According to EAM, the energy needed to embed an atom in a lattice site is taken to be a function of the

electron density at that particular site, then the cohesive energy was represented by a two-body term and a many body term as a function of electron density. The many body term overcomes the shortage of simple two-body potential like Lannard-Jones, and Morse potential, where the elastic constants always have Cauchy relation C12=C44, which is seldom true even in real metals.

But EAM has very complicated form and sometimes a simple analytical form is not even available. Finnis-Sinclair(FS) type potential [2-3] developed for transition metals, simply writes the repulsive energy as square root of electron density term, which came from an analogy with the second moment approximation to the Tight Binding Model (TBM). Even the origin of FS potential and EAM are different; they shear the same electron density term. And the simple empirical N-body FS potential works well for transition metals. But the interaction range is very short, only until second nearest neighbors, such that it's not good to describe surface properties.

Sutton-Chen (SC) developed long range force field for FCC metals based on Finnis-Sinclair potential [2-4]. The long range expansion of this interaction has an attractive $1/r^6$ pair term, like normal Van der Wals interaction. The long range property of SC potential makes it more accurate for surface and interface studies than Finnis-Sinclair potential. And the simple power law is faster to calculate than general embedded atom method.

In the SC-type many body FF, the total potential energy is expressed as

$$U_{tot} = \sum_i U_i = \sum_i D\left[\sum_{i \neq j} \frac{1}{2} V(r_{ij}) - c_i \rho_i \right] \qquad (2\text{-}1)$$

where r_{ij} is the distance between atom i and j, and $V(r_{ij})$ is a pair-wise potential

$$V(r_{ij}) = \left(\frac{\alpha}{r_{ij}}\right)^{n} \tag{2-2}$$

representing the repulsion between the atom I and j and j, and ρ_i is the local density associated with atom i defined as

$$\rho_i = \left(\sum_{j \neq i} \phi(r_{ij})\right)^{1/2} \tag{2-3}$$

$$\phi(r_{ij}) = \sum_{j \neq i} \left(\frac{\alpha}{r_{ij}}\right)^{m} \tag{2-4}$$

Where α is a length parameter leading to a dimensionless form for V and ρ, c is a dimensionless parameter scaling the attractive term, while D sets the overall energy scale. The pair-wise V(r) term (2) describes the short-range Pauli repulsion interactions between atoms i and j (arising primarily from Pauli repulsion between the core electrons).

To extend the SC model to alloys, Rafii-Tabar and Sutton have showed that it's not necessary to fit any new parameters for the alloy potentials [2-5]. Simply employing the combination rules of the parameters fitted for pure elemental metal, one can derive the interactions between unlike atoms. The combination rules we used to represent the interaction between a pair are the geometry average for D and a, arithmetic average for m and n, and the value of c is determined by the element of central atom i.

In Sutton-Chen potential the parameters are only fitted for lattice parameter, cohesive energy exactly, and bulk modulus closely. Recently we re-parameterized the

empirical many-body force field of the Sutton-Chen (SC) type for some FCC metals [2-6]. These parameters were obtained by fitting the lattice parameter, cohesive energy, bulk modulus, elastic constant, and phonon dispersion curves and tested for accurate values of surface energies, vacancy formation energy, equation of state, thermal expansion and specific heat. We refer to the new set of SC parameters as the QMSC FF. The QMSC parameters, which will be used in the simulations in this thesis, are shown in Table 2-1.

Table 2-1 Modified Sutton-Chen (M-SC) Force Field Parameters

	D (meV)	C	m	n	α (Å)
Ag	4.0072	94.948	6	11	4.0691
Cu	5.7921	84.843	5	10	3.6030
Ni	7.3767	84.745	5	10	3.5157
Au	7.8052	53.581	8	11	4.0651

The effective pair potential was cut off at twice of the lattice parameter (ranging from 7.2A to 9A in above elements and their alloys).

Although we got the parameters at low temperature in solid state (0K), it worked well to predict the melting temperature and other good properties in liquid state. This is because the potential took inverse power function in the pair potential term (V in equation 2-2) and the density term (ϕ in equation 2-4), so the third derivative to the potentials are continuous too. Such continuity is essential if the temperature dependence of the potentials is to be incorporated to model thermodynamics properties at elevated temperatures. Since we also took the efforts to fit the

parameters to various properties, the M-SC will give more accurate results than original SC potential in general.

The QMSC potential with new parameters has successfully simulated the melting, glass transition and crystallization processes in Cu-Ag and Cu-Ni alloys [2-7]; surface effects in phase transformation in Ni nano particles [2-8]; deformation behavior under high strain rate in NiAu, Ni and NiCu systems [2-9]; dislocation motion and energies in Ni [2-10]; viscosity of liquid Cu-Au system [2-11] and other thermal, mechanical and transport properties [2-12].

From the representation of the energy, we can calculate the force, pressure, and elastic constants directly. The many body force on atom I along a direction α=(x,y,z) or (1,2,3) is given as

$$F_{i\alpha} = -\frac{\partial U_{tot}}{\partial r_{i\alpha}} = -D\left(\sum_j^* u'(r)\frac{r_{ij\alpha}}{r_{ij}} - \frac{c_i}{2}\frac{\sum_j^* \phi'(r) r_{ij\alpha}/r_{ij}}{\rho_i} + \sum_j^* \frac{c_j}{2\rho_j}\phi'(r)\frac{r_{ji\alpha}}{r_{ji}} \right) \tag{2-5}$$

where $'$ denotes $\partial/\partial r$ and $*$ represents the exclusion of i=j from the summations.

The anisotropic stress tensor including the contribution from kinetic term and the many body potential is calculated from

$$VP_{\alpha\beta} = \sum_i \frac{p_{i\alpha}p_{i\beta}}{m_i} - \frac{D}{2}\sum_i \left(\sum_j^* u'(r)\frac{r_{ij\alpha}r_{ij\beta}}{r_{ij}} - c_i \frac{\sum_j^* \phi'(r) r_{ij\alpha}r_{ij\beta}/r_{ij}}{\rho_i} \right) \tag{2-6}$$

where V is the volume of the simulation cell, p_{ia} is the momentum of atom i along direction a.

The potential energy contribution to the elastic constants, the hypervirial tensor $\chi_{\alpha\beta\varepsilon\phi}$, with $\alpha,\beta,\varepsilon,\phi$ range 1, 2 and 3, is given as

$$V\chi_{\alpha\beta\varepsilon\phi} = \frac{D}{2}\sum_i \left(\begin{array}{l} \sum_j^* \left(u'' - \frac{u'}{r_{ij}} \right) \frac{r_{ij\alpha} r_{ij\beta} r_{ij\varepsilon} r_{ij\phi}}{r^2{}_{ij}} - c_i \frac{\sum_j^* \left(\phi'' - \frac{\phi'}{r_{ij}} \right) \frac{r_{ij\alpha} r_{ij\beta} r_{ij\varepsilon} r_{ij\phi}}{r^2{}_{ij}}}{\rho_i} \\ + \frac{c_i}{2} \frac{\sum_j^* \phi' \frac{r_{ij\alpha} r_{ij\beta}}{r_{ij}} \sum_k^* \phi' \frac{r_{ik\varepsilon} r_{ik\phi}}{r_{ik}}}{\rho_i^3} \end{array} \right) \tag{2-7}$$

2.3 Molecular dynamics simulation

Molecular dynamics (MD) is a computer simulation technique used to solve the Newton's laws of motion for the time evolution of a collection of atoms interacting via a potential U (for example the potential introduced in 2.1). The equation of motion for all the atoms in the system are integrated numerically by various finite difference methods at a set of time step. This technique will generate detailed phase space information, such as atomic position and velocities at each time step, which is also called the trajectory of the system. The trajectory generated from MD simulation, provides linkage between microscopic properties and average thermodynamic properties, such as pressure, temperature, internal energy, etc.

There are several different forms of molecular dynamics to simulate different ensembles. The original form of molecular dynamics generates the macrocanonical ensemble, or constant volume and constant total energy dynamics (NVE) [2-13]. Nosé [2-14] added an extra degree of freedom to describe the thermal bath behavior, such that the temperature of the system will fluctuate with respect to the thermal bath

temperature, this method can achieve canonical ensemble, or constant volume and constant temperature dynamics (NVT). Hoover [2-15] developed Nosé method to make the NVT calculation simpler. Andersen [2-16] developed a procedure to carry out isobaric-isoenthalpic ensemble, or constant pressure and constant enthalpy dynamics (HPN), by making the volume a dynamics variable.

Parrinello and Rahman [2-17] generalized Andersen method to allow the changes in box the size and shape of the simulation cell. They define a new matrix h by h=(**a**,**b**,**c**), where **a**, **b** and **c** are the three vectors spanning the periodic repeating parallelpiped simulation cell. In Parrinello and Rahman's theory, h becomes a dynamical variable to describe the shape and size changing of simulation cell. The introduction of h into the theory allows one to give a full description of the elastic properties of the system, such that one can define the strain and stress tensor as a new pair of extensive and intensive variables as V and P for a thermodynamics system, which lead to constant thermodynamic tension and constant enthalpy dynamics (HtN), or isobaric-isoenthalpic ensemble. The introduction of h also clarified that the original EVN dynamics is actually EhN, and original Nosé constant-TVN is actually ThN form of molecular dynamics, since the simulation box is kept unchanged not only in size but also in shape.

Ray and Rahman have presented [2-18] a detailed form of TtN dynamics, which combines Nosé constant-temperature theory with Parrinello-Rahman variable shape-size form of molecular dynamics. One can also combine Nosé's theory and Andersen's changing volume dynamics to achieve constant TPN dynamics. TPN

dynamics is suitable for isotropic liquid and gas phases, while TtN dynamics can simulate elastic deformation of solid state.

In our discussion, we'll focus on four ensembles E*h*N, T*h*N, H*t*N and T*t*N. We'll use Ray and Rahman's single Hamiltonian formulation which includes all of these different forms of MD. The Hamiltonian for the T*t*N form of MD has the form

$$H(s,\pi,h,\Pi,f,P)=\sum_i \frac{\tilde{\pi}_i G^{-1}\pi_i}{2m_i f^2}+U+\frac{Tr(\tilde{\Pi}\Pi)}{2W}+V_0 Tr(t\varepsilon)+\frac{P^2}{2M}+(3N+1)K_B T_0 \ln(f) \tag{2-8}$$

where (s_i,π_i) are the scaled coordinates and conjugate momentum of particle i, (h,Π) are the coordinates and momentum of the molecular dynamics cell, and (f, P) are the Nose mass scaling variable and its conjugate momentum. U is the potential energy, which is a function of the position of the atoms. The constants W, called "piston mass" and M, called "thermal inertia," are parameters to make h and f satisfy dynamical equations. The tilde indicates matrix transpose. T_0 is the thermal reservoir temperature, ε is the strain matrix which is gotten by

$$\varepsilon=(\tilde{h}_0^{-1}Gh_0^{-1}-1)/2 \tag{2-9}$$

where G is the metric tensor, $G=\tilde{h}h$, and h_0 is the reference state of the cell matrix h at zero tension. V_0 is the reference volume, calculated from $V_0=\det(h_0)$.

The usage of h matrix maps the simulation cell with any shape into a unit cell. Such that the physical particle position and momentum (r_i, p_i) are related to the scaled particle variables (s_i,π_i) by $r_i=hs_i$ and $p_i=\tilde{h}^{-1}\pi_i/f$, and s_i range from 0~1. Therefore, the particle kinetic energy is represented by the first term in Hamiltonian (if we define the physical momentum of the particle as $p_i=m_i fh\dot{s}_i$, then

$KE = \sum_i p_i^2 / 2m_i$), and the first two terms in eq. (2-8) is the Hamiltonian for N particles in the simulation system.

The elastic energy of the system given in the 4th term in eq. 2-8, and the 3rd term in eq. 2-8 is similarly to the kinetic energy with the momentum of the *h* matrix. The last two terms are similar kinetic term and potential term for *f*, the mass scale variable to achieve constant temperature dynamics.

The equation of motion derived from Hamiltonian in eq. (2-8) has the form of

$$m_i f^2 \ddot{s}_{i\alpha} = -\sum_{j \neq i} \frac{(\partial U / \partial r_{ij}) s_{ij\alpha}}{r_{ij}} - m_i (f^2 G^{-1} \dot{G} + 2 f \dot{f}) s_{i\alpha} \tag{2-10a}$$

$$W \ddot{h}_{\alpha\beta} = P_{\alpha\beta} V \tilde{h}^{-1} - h V_0 h_0^{-1} t \tilde{h}_0^{-1} \tag{2-10b}$$

$$M \ddot{f} = \frac{2KE}{f} - \frac{(3N+1) k_B T_0}{f} \tag{2-10c}$$

where $P_{\alpha\beta}$ is the microscopic stress tensor as we defined in the eq. 2-6 for the specified QMSC force field, and the second term in 2-10b is related to the applied tension to the system. It's the difference of the system tension and applied tension that causes the fluctuation of *h* matrix.

With no constrains, TtN dynamics require the solutions of 3N+9+1 equation of motions. (N are the number of movable particles with 3 degrees of freedom, *h* matrix has 9 independent components, and one more degree of motion of *f*.) We can get the equation of motion of the other three dynamics from TtN dynamics with constrains. If the Nosé variable *f* satisfies $\dot{f} = 0, f = 1$, only equation of motions of 2-10a and 2-10b are needed to solve, so we reduce constant TtN to constant HtN dynamics.

Similarly constrain on h as $\dot{h} = 0, h = cons\tan t$ leads to the equation of motion reduced to the combination of 2-10a and 2-10c, such that a constant ThN dynamics is achieved. If f and h satisfy that $\dot{f} = 0, f = 1$ and $\dot{h} = 0, h = cons\tan t$, the only equation of motion is 2-10a, which gives constant EhN dynamics.

2.4 Obtain thermodynamic, structural and transport properties from MD

MD generates a series of phase functions, which can be identified in each time step, such that the basic thermodynamic properties of the modeled system can be calculated as averages in any convenient ensemble. Thermodynamic properties such as enthalpy H, total potential energy E, kinetic energy KE, density D, temperature T, pressure P, etc., can be calculated straightforward from the average. For example, the internal energy and enthalpy can be calculated from

$$E = \langle KE \rangle + \langle U \rangle \tag{2-11}$$

and

$$H = \langle E \rangle + Pext\langle V \rangle \tag{2-12}$$

Other properties such as heat capacity Cp or Cv and isothermal elastic constants $C_{\alpha\beta\varepsilon\phi}$, thermal expansion coefficient α_P, and isothermal compressibility β_T represents the response function of a system, which can be connected to the thermal fluctuations in different ensembles. For example, the total internal energy fluctuation is related to the constant-volume heat capacity, enthalpy fluctuation is related to constant-pressure heat capacity, volume fluctuation is related to isothermal compressibility, strain stress

fluctuation is related to elastic constants, and cross-correlation of volume and enthalpy is related to thermal expansion.

$$C_V = \left(\frac{\partial E}{\partial T}\right)_V = \frac{\langle \delta E^2 \rangle_{NVT}}{k_B T^2} \tag{2-13}$$

$$C_P = \left(\frac{\partial H}{\partial T}\right)_P = \frac{\langle \delta H^2 \rangle_{NPT}}{k_B T^2} \tag{2-14}$$

$$\beta_T = \frac{-1}{V}\left(\frac{\partial V}{\partial P}\right)_T = \frac{\langle \delta V^2 \rangle_{NPT}}{k_B T V} \tag{2-15}$$

$$\alpha_P = \frac{1}{V}\left(\frac{\partial V}{\partial T}\right)_P = \frac{\langle \delta V \delta H^2 \rangle_{NPT}}{k_B T^2 V} \tag{2-16}$$

$$\begin{aligned} C^T{}_{\alpha\beta\varepsilon\phi} &= -\left(\frac{\partial t_{\alpha\beta}}{\partial \varepsilon_{\varepsilon\phi}}\right)_T = \frac{k_B T}{V\langle \delta\varepsilon_{\alpha\beta}\delta\varepsilon_{\varepsilon\phi}\rangle_{TtN}} \\ &= V\frac{\langle \delta P_{\alpha\beta}\delta P_{\varepsilon\phi}\rangle_{ThN}}{k_B T} + \frac{2Nk_B T(I_{\alpha\beta}I_{\varepsilon\phi} + I_{\alpha\phi}I_{\varepsilon\beta})}{V} + \langle \chi_{\alpha\beta\varepsilon\phi}\rangle \end{aligned} \tag{2-17}$$

The time average of fluctuations is given by $\langle \delta A \delta B \rangle = \langle AB \rangle - \langle A \rangle \langle B \rangle$, where A and B are any dynamic variable. The elastic constants is given in strain fluctuation in constant stress ensemble and stress fluctuation in constant shape ensemble, where $P_{\alpha\beta}$ is the microscopic stress given in eq. 2-6, and the second term is the kinetic energy contribution ($I_{\alpha\beta}$=1 when $\alpha = \beta$, and $I_{\alpha\beta}$=0 when $\alpha \neq \beta$), and the third term is the Born term, defined in eq. 2-7.

Since MD can provide detailed atomic information about the structure, which can be either related to the macrostructure in experiments or describe the structures cannot be observed in experiments. To observe the symmetry, order and a collective

behavior of atoms in the system, the correlation functions of a variety of physical quantities over real space or reciprocal space are needed.

First we define the pair correlation function g(r), or radial distribution function (RDF), as

$$g(r) = \frac{V}{N^2} \sum_{i,j>i} \delta(r_{ij} - r) \tag{2-18}$$

This function gives the probability of finding a pair of atoms a distance r apart, normalized to the probability expected for a completely random distribution at the same density. RDF is very useful to find the glass transition; it will show the peaks in a crystal structure, but not the second nearest neighbors peak in crystal for a disordered phase. The second peak in liquid RDF will split when a local order exists, which characterizes the glass phase.

In reciprocal space, we can first define a vector, K,

$$K = (\tilde{h}^{-1})(n_{a,} n_{b,} n_c) \tag{2-19}$$

where na, nb and nc are integers, then the spatial Fourier transform of the number density is given as

$$\rho_K(r_i) = \sum_{i=1}^{N} \exp(-iKr_i) \tag{2-20}$$

The fluctuation of ρ(K) is directly related to the structure factor, S(K), in Bragg diffraction at a specific reciprocal vector K by

$$S(K) = \frac{1}{N} \langle \rho(K)\rho(-K) \rangle = \frac{1}{N} \sum_{i,j} \left\langle e^{i2\pi K r_{ij}} \right\rangle \tag{2-21}$$

In crystal a long range translation order exists, for some specific K vector, all atoms can contribute to S(K), such that S(K) can accumulate to the number of atoms, while for some other specific K vectors, the overall diffraction of the atoms can lead to a vanished S(K). Such a diffraction pattern can be compared with the experiments. However, S(K) can only reache a fraction of number of atoms if only a short range translation order exists.

The correlation function of any variables measured at different time can give a picture of the dynamics properties of the system. These time correlation functions can be related directly to macroscopic transport properties, and their Fourier transform may be related to experimental spectra. The transport properties are defined in terms of the responds of a system to a perturbation, for example the diffusion coefficient relates to a concentration gradient, shear viscosity is a measurement of the shear stress induced by an applied velocity gradient, and thermal conductivity relates to the temperature gradient. In computer simulations, transport coefficients may be calculated from equilibrium time correlation function.

The diffusion coefficient D is given in Einstein relation (in three directions) by

$$D = \frac{1}{6N}\tau\sum_{i=1}^{N}\left\langle \left| r_i(t_0+\tau) - r_i(t_0) \right|^2 \right\rangle \qquad (2\text{-}22)$$

To improve statistics, t_0 can be any starting time on the trajectory, and then averages over time. The diffusion coefficient is valid from correlation behavior of long-time τ, especially in liquid. In solid the diffusion is through vacancy and interstitials mechanism, which takes longer time than a typical MD simulation run can cover.

2.5 MPiSIM: Massively parallel simulation tool for metallic system

2.5.1 Introduction of parallel MD

It's our interests to study the grain boundary, dislocation, cracks, void, vacancy, and other defects in solid to model the plastic behavior and mechanical properties of solid; to study the dynamics properties of condensed matter under high speed impact, and understand the shock wave propagation and phase transition during shock and spallation; to study the deformation of bulk metallic glass, which is well known initiated by shear band, but the formation of shear band and the structural properties are unknown yet. All these problems require to model ever-increasing system sizes, at least millions of atoms, which is beyond the capacity of current computer facilities. While massively parallel (MP) computing hardware got improved in last 10 years, it also requires the development of new parallel algorithms for simulation methods. G. S. Heffelfinger gave a good review on these efforts [2-20].

Because MD is inherently parallel [2-21], parallel MD algorithm were among one of the first parallel algorithms developed on various machines. There are three parallel methods based on decomposition strategy: "replicated data" or "atom decomposition" (each processor is assigned a fixed subset of atoms), "systolic loop" or "force decomposition" (each processor is assigned a fixed subset of forces matrix), and "spatial or geometric decomposition" (each processor is assigned a fixed spatial region). These methods on various systems were reviewed by Heffelfinger and detailed descriptions especially for short-range interactions were presented by Plimpton [2-22].

Many efforts of parallel algorithm were designed or optimized for the architecture of the supercomputer. However, in our new MPiSIM development, we targeted a general, expandable, flexible and portable simulation tool for short-range interactions system, such as metallic system. MPiSIM used standard C language and MPI (Massage Passing Interface) library to achieve good portability. We also tried to design our algorithm as general and easy to expand as possible, which means it's very convenient to add different potentials and dynamics methods.

Currently we have implemented different force field, such as Morse potential[2-23], a Sutton-Chen type of many body potential [2-6], and an EAM potential for tantalum [2-24]. MPiSIM can simulate periodic boundary condition (PBC) in any direction or no PBC for free surfaces studies. The integration of equation of motions is done either by leap-frog, by velocity Verlet or by 5^{th} order of Gear predictor-corrector [2-1] [2-25]. In terms of simulation methods, it can simulate constant NVE and NVT dynamics, uni-axial strain/compression tests, and sliding boundary for shock wave simulations.

2.5.2 Implementation method

2.5.2.A Data structure

Since most of the potentials we consider in this program are short-range interactions, we employ a cutoff, Rc, in our simulation. We construct a neighbor list for each atom with a larger cutoff R, Rs=Rc+δ, where δ is called the "skin" of the cutoff sphere. This neighbor list will be updated at intervals. To save time of constructing this neighbor list, we combine link-cell method with neighbor list. In

link-cell method, atoms are binned into 3D cells of length of d, where d is equal or slightly larger than Rs, so the neighbor of a given atom only fall into the 27 bins — the bin where the atom is and the 26 first nearest neighbor cells. This reduces the neighbor searching time to O(N). The atoms are only redistributed into cells once every few time-steps, which is the time interval of a new neighbor list is reconstructed. After the neighbor list is constructed, it will be used for a few time-steps.

Based on the neighbor list and link-cell methods, the atomic information is designed as a data structure, with atomic number, mass, coordinates, velocity, force, atom type, electrical density (used in EAM potential), pointer to the cell it belongs, and the neighbor atoms list. The link-cell array has a 3D integer coordinate for easy neighbor cell finding, and each cell has a link list of pointers, pointing to the atoms inside it.

2.5.2.B Spatial decomposition method:

The whole simulation box is decomposed into sub-domains and each of them is attributed to one processor. To take advantage of link-cell method, the unit of the communication is taken as the link-cell. Before a structure is read in, the number of cells in each direction is determined first, according to the dimension of the simulation box and the cutoff. Then the link-cells will be distributed into Np processors. After this, the atomic structure will be either read in from one processor then distributed into each processor according to their physical position, or be generated in all processors, but only atoms physically allocated on the processor will be kept. During the atom data structure construction, the atoms are distributed into

cells at the same time. After this data distribution, the whole simulation cell now is divided into processor, and each processor contains a collection of link-cells and atoms within it.

Due to the arbitrary shape of the simulation cell, the processor used on x,y,z directions can be specified by the user, so that the total number of processor Np=Px*Px*Py, where Px, Py and Pz are the number of processors used on each direction. The number of link-cells on each processor is equally divided on each direction, since right now the density of the simulation system is quite uniform. To solve the big problem of spatial decomposition, load balance, we will enable user to specify the number of cells on each processor based on the estimated density distribution for next stage development. But this method still can't automatically balance the load on each processor during the simulation. Load balance problem is hard to overcome, if the density of simulation system is heterogeneous.

2.5.2.C Communication method:

Since link-cell is used, each cell should have its nearest 26 neighbor cells to build the neighbor list. For the link-cells on the boundary of each processor, it needs to shear the information of neighbor link-cell and atoms within them from the nearby processors. We will call these cells as sheared information zone, and the duplicated atoms as image atoms.

Figure 2-1 shows communication mechanics in 2D. The number of link-cell on each process is defined as n_{cx}, n_{cy} and n_{cz}. First, the communication is made along +x direction (east), which means each processor sending atoms within the most east link-cells (n_{cy}*n_{cz} link-cells) into next processor, then the communication is made along –

x (west) direction. Secondly, the communication is done along y (north) direction, where the number of link-cell in communication is $(n_{cx}+2)*n_{cz}$, then the next communication is along y direction (south). Thirdly, the last communication is along z (up and down) direction and the number of link-cells in communication is $(n_{cx}+2)*(n_{cz}*2)$. After the communications along six directions, one cell is added in both directions of each of the three dimensions. As shown in Figure 2-1, atom A and B are physically located on processor P0, and atom C is located on processor P1; after the communication, atom C has an image on processor P0 and so is B's image on processor P1.

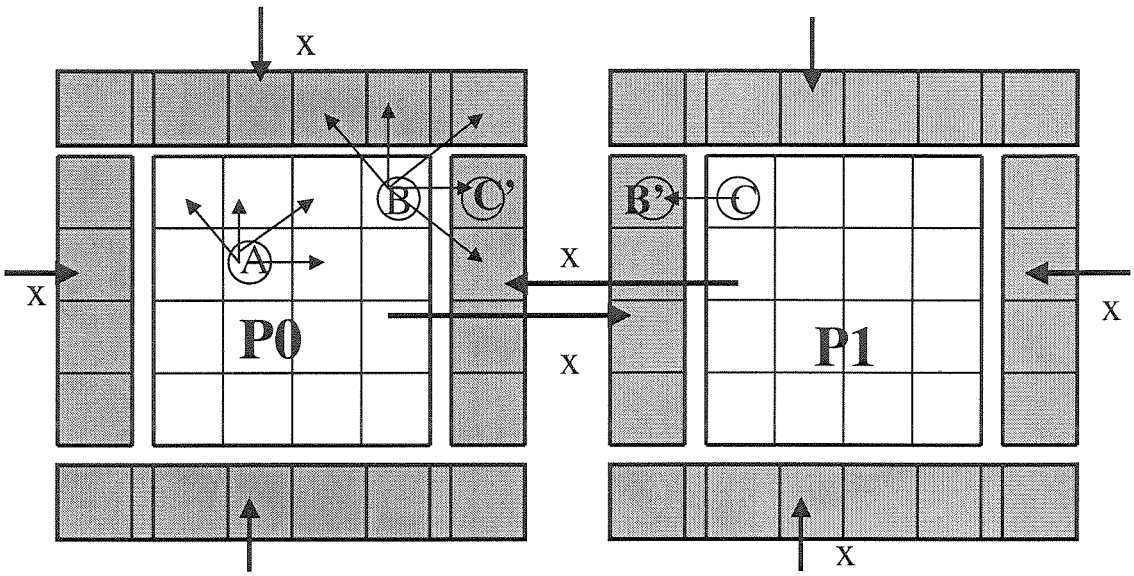

Figure 2-1 A schematic 2-D representation of the communication of atoms on the boundary of nearby processor and the link-cell neighbor search pattern used in domain decomposition program.

To achieve periodic boundary condition (PBC), the atoms are shifted along the periodic direction before communication. For example, to apply periodic along x direction, we send the most-east atoms in most-east processors to the most-west processor, after we added a displacement of "-Lx" (Lx is the length of simulation box along x) for these atoms. And then shift "+Lx" for atoms sending from most-west processors to the most-east processor. Periodic boundary condition is applied independently for each direction, to simulate clusters, wires, thin-films and bulk materials.

Each processor is responsible for computing the force and new positions for the atoms physically located on it. From Figure 2-1 we can see that in each processor there are two types of atoms, atom A, with its neighbors on the same processor, and atom B, with some of its neighbors located on the other processor, but having an image on the current processor. Not all of the information of the atoms needed to be communicated in every step. At each step the forces are calculated on each processor and the position of atoms got updated, then the new positions of atoms in the sheared zone got passed to nearby processors, which means the image atoms position also got updated on each processor, preparing for the calculation at next step.

For pair wise potential, like LJ and Morse, it's simple to only compute a force once for each pair of atoms, rather than once for each atom in the pair. EAM potential generally contain a two-body term and an electrical density term, which is also a function of summation of paired interactions between the given atom and its neighbors. Therefore, the electrical density term calculation can still be treated as a pair wise potential, which only needs calculating once for each pair of atom. So only

13 neighbor cells have to be considered to construct the neighbor list for calculation of the energy and force.

One thing special about EAM is that the electrical density term needs to be updated in the sheared zone before the total energy and the accurate force on each atom can be calculated. So there is only one position communication in two-body potential calculation, but two communications for electrical density and positions in many-body potentials, at each time step.

D. Brown et al. [2-26] has proposed a domain decomposition strategy by sending positions of atoms to nearby processors along three directions: east, south and above, then sending the force back along west, north and below, after the processor finishes the force calculation. This method is suggested to minimize communication and avoid redundant force calculation. But the communication data of position and force along three directions almost has the same amount data as the communication with position along six directions. Even though the force only calculated on one processor, it needs extra space to accumulate forces for image atoms, and after the forces being sent back, the combination of the force contributed from the same processor and nearby processors also takes time. Also a lock is added before all the forces being sent back. We don't know how much time this method will save, but it is hard to handle many-body force field calculation, where the force is not simply summation of atoms interaction.

In our design the communication is not based atom to atom, but cell to cell. A collection of atom information will be sent together, while only a temporary array is

needed for each communication. Only one global lock is added for summation of the total energy.

2.5.2.D Atoms redistribution

To keep the neighbor list and link-cell methods working, we need to update the atoms within the link-cell and redistribute the atoms to processor when some atoms diffuse away. We do this update every few timesteps, and assume that some atoms travel more than the skin distance, but less than the link-cell size. To avoid an all atoms communication between all the processors, we noticed that only the image atoms in the nearby processor's link-cells can move into the current processor , and only the atoms in the boundary link-cells can move out of the current processor. Since we kept the image atoms information from last link-cell update, we only need to copy the moving in atoms from image atoms, and delete the moving out atoms. This method will save the communications time between nearby processors.

2.5.3 Performance test

2.5.3.A Efficiency of MPiSIM

The computation time for each time step contains three parts: the time of calculation of force and energy took place on each processor, which is linear scaled as Np, number of atoms; the time cost on communication, which is proportional number of atoms in communication; and the time cost on the double calculation of energy of atoms on the boundary atoms, due to the duplication. If we assume the number of cells on each direction in every processor is equal, Nc, and the number of atoms in

each cell is basically uniform, represented by D, we can write the time needed on each processor as

$$T(Np) = T_1 / Np + 13(3Nc^2 - 3Nc + 8)D\tau_e + (3Nc^2 + 3Nc + 8)D\tau_c \qquad (2\text{-}23)$$

where Np is the number of processors, T_1 is the time needed on only 1 processor, τc is the communication time per atom and τe is energy calculation time per atom. T1 scale linearly with the size of the simulation system, N, such that the dynamics time scales as N/Np. The second and third term in eq. 2-23 are proportional to Nc^2D, where Nc is proportional to $(N/Np)^{1/3}$, and D is independent on N and Np, so the communication time and duplication time scale as $(N/Np)^{2/3}$. We can't avoid time cost of communication and redundant force calculation, but the more cells on each processor, the more efficient the algorithm.

2.5.3.B Performance on ACL Nirvana machine

On ACL Nirvana Machine, we have tested our algorithm up to 512 processors. The first test is a series of 1000 steps EVN dynamics on system sizes range from 4000 to 1024000 Ni atoms, described by Sutton-Chen type of potential.

In Figure 2-2, we showed the computational time of various sizes on four processors. Since we used the combination of link-cell and neighbor list methods, the computational time scales O(N). The scaling performance of simulation size agrees well with the ideal linear scaling, represented by the solid line.

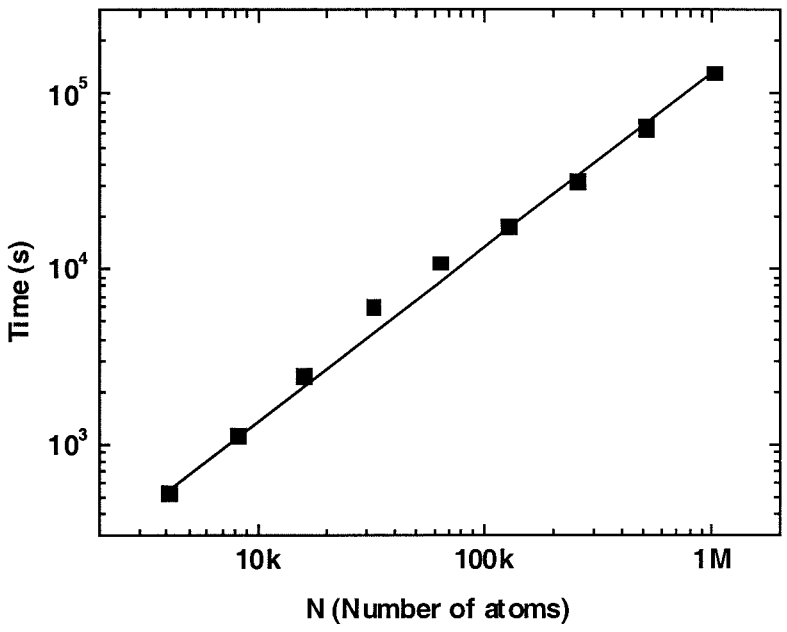

Figure 2-2 Scaling performance over size of the simulation system on ACL Nirvana Machine. The CPC time is for 1000 steps of NVE dynamics on four processors of Ni systems with Sutton-Chen many-body potential.

In Figure 2-3, we showed the simulation time scaling performance on different sizes of systems, and the dash line is the ideal linear scale of Np for system with 1024000 Ni atoms. The linear scale works well until 128 processors, then the computational time increased as processor number larger than 256 processors. Other groups who used the same machine have found the similar scaling behavior, which indicates this is a hardware related problem. The ACL Nirvana Machine consists of 16 SGI Origin 2000s each with 128 processors. The system interconnect is based on the HiPPI-800 standard and is currently being upgraded to HiPPI 6400/GSN

technology which will result in a bisection bandwidth of 25.6Gbytes per second bi-directional. Since the communication time within the box is much faster than the communication between boxes, the performance beyond 128 processors is slowed down by the communication between processors in different boxes. The more detailed discussion of communication time is not the focus of this paper. The scaling performance is not related to the potential employed in simulation. A scaling test on Ta, which used an EAM potential, showed the similar behavior.

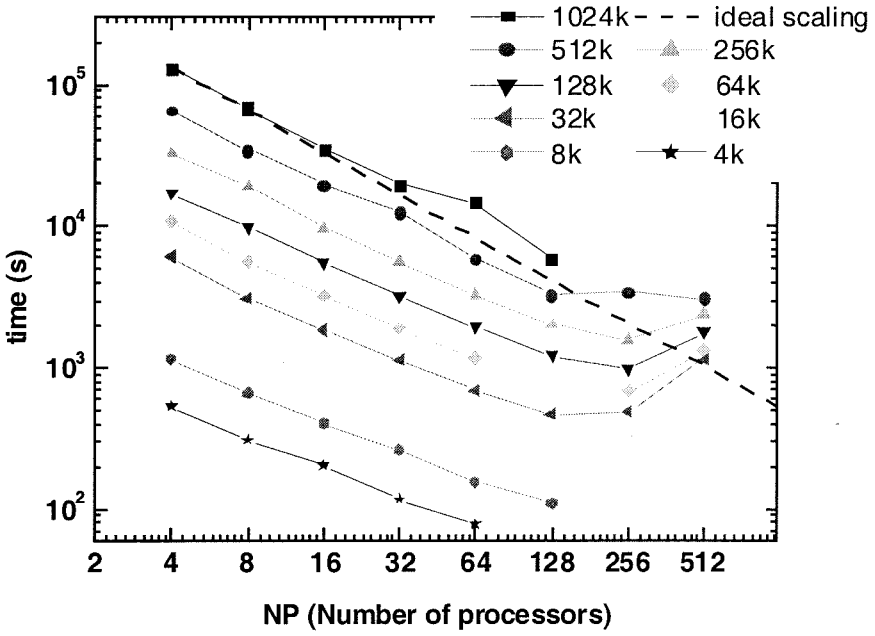

Figure 2-3 Scaling performance over Np, the number of processors used, on ACL Nirvana Machine. The CPC time is for 1000 steps of NVE dynamics of Ni systems with Sutton-Chen many-body potential.

2.5.3.C Performance on other platforms

Since we used the standard MPI library for information passing, the efficiency of MPiSIM is dependent on the MPI implementation on different platforms. We have tested MPiSIM on Origin 2000 (operating system is irix6.2 with MPI3.2 from SGI) in MSC, Caltech and NCSA, UIUC up to 16 processors, a Dell PC Beowulf cluster (operating system is Red Hat Linux 6.2 with LamMPI 6.3.2 from U. of Notre Dame) up to 12 processors, and HP Examplar X-class supercomputer (operating system is SPP-UX 5.3 with MPI from HP) in CACR, Caltech up to 16 processors. Due to the available resource we only test on these platforms up to maximum 16 processors. From our comparison in Figure 2-4, the Origin 2000 gave the best linear scaling of Np.

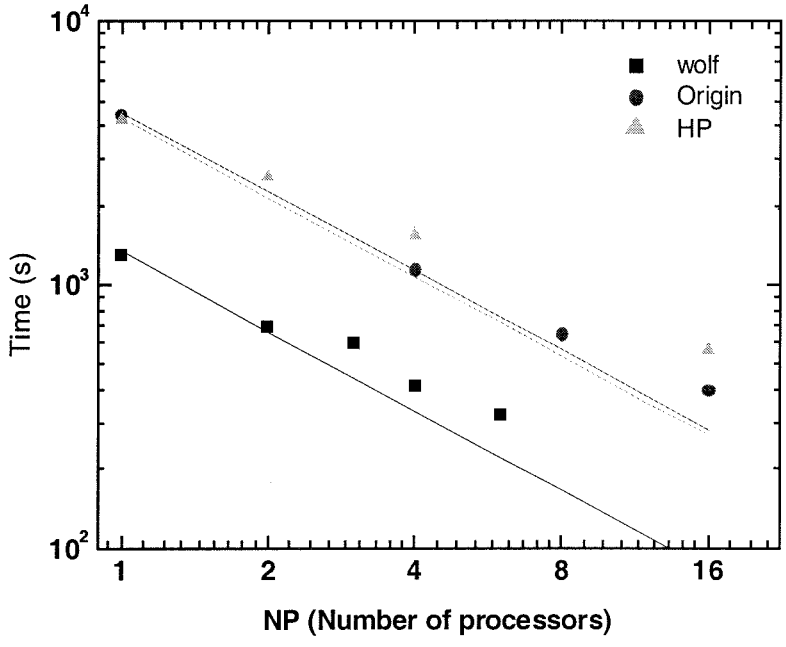

Figure 2-4 MpiSIM scaling over Np performance on various platforms, including Origin2000, HP Examplar X-classer, and Dell PC Beowulf cluster (wolf).

2.5.4 Applications

The MPiSIM has been applied to various materials properties studies. At nano-scale simulations, we studied melting and crystallization for Ni clusters ranging from hundreds to 8000 atoms, while two regimes have been captured [2-8]. We also studied the dissociation, core energy, core structure, and annihilation processes of screw dislocations in Ni [2-10]. Other studies such as shock wave propagation in Ta and shear band formation in CuAg are carried on as well.

2.5.5 Summary

MPiSIM, the massively paralleled simulation tool for metallic systems with various potentials, have been developed and used on different applications. The portability on other machines can be easily done without modifying the code, due to the usage of MPI for parallelization. But the best scaling results are on SGI origin 2000 based machines. In the near future the NPT dynamics and non-equilibrium MD (NEMD) will be implemented and more visualization tools and other utilities will be developed for analyzing the simulation results.

References:

[2-1] M. P. Allen and D. J. Tildesley, Computer Simulation of Liquids (Oxford, 1987)

[2-2] M. S. Saw and M. I. Baskes, Phys. Rev. B **29**, 6443 (1984); also M. S. Daw and M. I. Baskes, Phy. Rev. Lett. **50**, 1285 (1983)

[2-3] M. W. Finnis and J. E. Sinclair, Phil. Mag. A **50,** 45 (1984)

[2-4] A. P. Sutton and J. Chen, Phil. Mag. Lett. **61** (1990)

[2-5] H. Rafii-Tabar and A. P. Sutton, Phil. Mag. Lett. **63**, 217 (1991)

[2-6] Y. Kimura, T. Cagin, Y. Qi and W. A. Goddard III, Phys. Rev. B, submitted

[2-7] Y. Qi, T. Cagin, Y. Kimura and W. A. Goddard III. Phys. Rev. B **59**, 3527 (1999)

[2-8] Y. Qi, T. Cagin, W. L. Johnson and W. A. Goddard, J. Chem. Phys. accepted

[2-9] H. Ikeda, Y. Qi, T. Cagin, K. Samwer, W.L. Johnson and W. A. Goddard III, Phys. Rev. Lett. **82**, 2900 (1999), and Y. Qi, H. Ikeda, T. Cagin, K. Samwer, W.L. Johnson, W. A. Goddard III, Bulk Metallic Glasses, MRS Symp. Processing Vol. **554**, 367 (1999)

[2-10] Y. Qi, A. Strachan, T. Cagin and W. A. Goddard III, Mat. Sci. and Eng. A, **309**, 156 (2001)

[2-11] Y. Qi, T. Cagin, Y. Kimura and W. A. Goddard III, Phys. Rev. E, submitted.

[2-12] T. Cagin, Y. Qi H. Li, Y. Kimura, H. Ikeda, W. L. Johnson, and W. A. Goddard III, Bulk Metallic Glasses, MRS Symp. Processing Vol. **554**, 43 (1999)

[2-13] M. P. Allen and D. J. Tildesley, "Computer Simulation of Liquids", Oxford science publication, (1997)

[2-14] Shiuchi Nosé, J. Chem. Phys. **81**, 511 (1984)

[2-15] W.G. Hoover, Phys. Rev. A **31**, 1695 (1985)

[2-16] H. C. Andersen, J. Chem. Phys. **72**, 2384 (1980)

[2-17] M. Parrinello and A. Rahman, Phys. Rev. Lett. **45**, 1196 (1980)

[2-18] J.R.Ray and A. Rahman, J. Chem. Phys. **82,** 4243 (1985)

[2-19] R. Ray, Comput. Phys. Rep. **8**, 109 (1988)

[2-20] G. S. Heffelfinger, Comput. Phys. Commun. **128**, 219 (2000)

[2-21] B. M. Boghosian, Comput. Phys. Jan/Feb (1990)

[2-22] S. Plimpton, J. Comput. Phys. **117**, 1 (1995)

[2-23] F. Milstein and B. Farber, Phys. Rev. Lett. **44**, 277 (1980)

[2-24] A. Strachan, T. Cagin, O Gulseren, S. Mukherjee, R.E.Cohen and W. A. Goddard III, Phys. Rev. B, submitted (2001)

[2-25] C. W. Gear, "Numerical initial value problems in ordinary differential equations" Prentice-Hall, Englewood Cliffs, NJ (1971)

[2-26] D. Brown, et al. Comput. Phys. Commun. **74**, 67 (1993)

Chapter 3 Glass formation and crystallization of liquids in bulk alloys

3.1 Introduction

The crystallization will always occur in equilibrium solidification. However, if the homogenous nucleation of crystals in the undercooled liquid melt is prevented on laboratory time scale, a metastable glassy phase can form. It's well known that this glass phase can be obtained either from a liquid or a gas phase by fast quenching, which reduces the atomic mobility so as to prevent nucleation and growth of crystal phase [3-1].

Metal glasses were first prepared [3-3] by Duwez's group at Caltech in the 1960's by cooling a AuSi eutectic at 10^6K/s. The understanding of the factors predisposing an alloy to glass formation have been developed sufficiently that Johnson et al. [3-3] have made TiZr based metal glasses at cooling rates of only 1 K/s. Factors that play important roles are mismatching in atomic sizes (e.g., Zr versus Ti with a radius ratio of 1.10 or Ag versus Cu with a radius ratio of both 1.13 favor formation of a glass) [3-4] and mismatching in bond character (thus adding Be or B plus Fe or Ni to the TiZr favors glass formation). Such amorphous metal glasses have numerous desirable properties. For instance, they are extremely ductile and resistant to corrosion [3-5]. Despite the progress in making TiZr based amorphous metals (which are now in commercial use), it has not yet been possible to develop bulk metallic glasses based on Fe, or Al, or Cu, each of which might lead to numerous practical applications. To develop a better understanding of the factors controlling glass formation in metal

alloys, we have started a program in carrying out atomistic simulations to elucidate the factors controlling the balance between crystallization and glass formation.

MD simulations have previously been used to study glass formation from liquid in Lonnard-Jones system [3-6][3-7] and many realistic systems with different force fields. Among these are studies on pure metals, such as sodium [3-8], potassium [3-9], rubidium [3-10], nickel [3-11], and iron [3-12], and binary metal-alloys including good glass formers, like Ni-Zr [3-13][3-14], Ti-Al [3-15], and $Ni_{33}Y_{67}$ [3-16].

In this chapter, we use molecular dynamics (MD) in conjunction with the quantum Sutton-Chen (QMSC) force fields (FF)[3-17], to examine melting and quenching of CuNi and CuAg alloys. These two model systems were particularly chosen, since Cu and Ag have very different sizes, making them good candidates for forming a metal glass, while Cu and Ni have similar sizes thus making them good candidates for forming a crystal even at high quenching rates. In section 3.2 we will discuss the glass formability, in section 3.3, we summarize the MD simulation approaches for heating and quenching processes, and in section 3.4, 3.5, and 3.6 we will discuss the results showing that CuAg forms a glass at all quenching rates used while CuNi forms a crystal at these same quenching rates.

3.2 Glass forming tendency and the choice of alloys

The fact that cooling rate used to form metallic glass ranges from 10^6 to 1K/s in experiments indicates the dramatic difference of glass forming tendency (GFT) in various alloys. A simple parameter that has been found especially useful is the reduced glass transition temperature, Tgr=Tg/Tm, the ratio of the glass transition

temperature to the melting temperature. Turnbull [3-18] predicted that as Trg increased from values near 0.5 to values near 0.66, the homogenous nucleation in the undercooled melt should become very sluggish on laboratory time scale. Increasing Trg is a key parameter to consider in GFT. Chemical disordering, such as mismatch in atomic size and difference in the valence electron configuration, also can enhance the GFT. Egami et al. [3-19] have demonstrated that for two atoms of different size, there exists a critical maximum solubility in both the terminal solid solution, outside which the solid solutions becomes unstable with respect to transformation to the glass form. The disordered phase is better to accommodate the atomic level strain caused by mismatch of atomic sizes, due to the configurational entropy. All glass forming binary alloys have two common features: dramatic difference between atomic species, either in size or chemical bond character and relatively low melting temperature.

We choose random FCC alloys of Ag_6Cu_4 and Cu_1Ni_1 alloys for different GFT. In Ag-Cu alloy, a eutectic exists at 60.1 at.% Ag, 39.9 at.% Cu, and the metallic glass was made in the lab in 1960 by quenching the molten alloys at the rate of 10^6K/s [3-20]. This propensity to form a glass is due to the difference in atomic size, $(R_{Ag}-R_{Cu})/R_{Cu}$ =0.13, and the low melting temperature of CuAg at eutectic composition, (1053K compared with 1235K for Ag and 1358K for Cu). So we choose Cu_4Ag_6 as the model glass former.

On the other hand, Cu and Ni have very similar atomic size, $(R_{Cu}-R_{Ni})/R_{Cu}$ =0.025, and they form infinite solid solution at low temperature. So that CuNi is expected to form a random fcc structure at low temperature. Indeed (experimental)

rapid quenching of liquid CuNi or Cu from the melt has not yet led to formation of a glass.

3.3 Simulation of heating and quenching processes

The simulation is based on constant temperature, constant thermodynamic tension molecular simulation (TtN MD)[3-21], which combines thermodynamics of Nosè [3-22] canonical ensemble with the Parrinello-Rahman variable shape and size ensemble [3-23]. TtN MD captures very detailed microscopic information about the system, allowing us to study the phase transformation while permitting the shape and size of the cell to change. With an accurate FF it should give values of volume, structure, energy, and other thermal properties comparable with experimental data.

We carried out a series of TtN MD simulations as a function of temperature to simulate the heating and cooling processes. The heating and cooling rates were controlled by limiting the simulation time at each temperature. The TtN MD simulations started from a cubic box with 500 atoms (random FCC for alloys) subject to periodic boundary conditions (PBC). To obtain the stress free reference size and shape of the unit cell, we performed 50ps of simulation with constant enthalpy, constant thermodynamic tension (HtN) at zero pressure. The TtN MD simulations were carried out at a series of increasing temperatures from 300 to 1500K in 100K increment. The final temperature of 1500K is a few hundred degrees above the melting temperature. At every temperature, the MD integration time step was taken as 1 fs, and the simulation time was 25ps, which leads to a heating rate of $4*10^{12}$K/s. To define the melting temperature clearly, a small increment of temperature as 20K

was carried out in the region of 1000K~1200K, with a shorter simulation time of 5ps to achieve the same heating rate.

After equilibrating the structure in the liquid phase at 1500K, we cooled the system using different quenching rates from 1500K down to 300K in 100K decrements in the TtN ensemble. To achieve the fast, intermediate, and slow cooling rates, we kept model system at the same temperature for times of 50ps, 25ps, and 0.25ps. This leads to cooling rates of $2*10^{12}$, $4*10^{12}$, and $4*10^{14}$K/s, respectively. To ensure convergence of the results for the fastest cooling rate (0.25ps per 100K), we performed additional 25ps long TtN simulations, restarting from the conditions at the end of each 0.25ps interval (for each 100 K drop), for thermodynamic averaging.

The energy, volume, radial distribution function and structure factor were averaged over the full trajectory for each temperature. The time evolution of energy and structural factor was obtained later from the trajectory file of the MD process.

3.4 Melting in bulk CuAg, Cu and CuNi alloys

Figure 3-1 shows the variation of the volume as Ag_6Cu_4 and CuNi are heated. The large jumps in volume in the temperature range of 1000K to 1200K for Ag_6Cu_4 and 1500K to 1600K for CuNi during the heating process are due to the melting. In order to obtain a more refined estimate of Tm, we used a smaller increment in temperature, namely 20K, for this melting region. This leads to a theoretical melting temperature of Tm=1090K for Ag_6Cu_4, in reasonable agreement with experimental melting temperature of 1053K. And for CuNi we got Tm=1530 at the heat rate of $4*10^{12}$K/s,

while in experiments, the melting of CuNi (atm. 50%) occurs from 1523K to 1563K, with a liquid and solid coexist state.

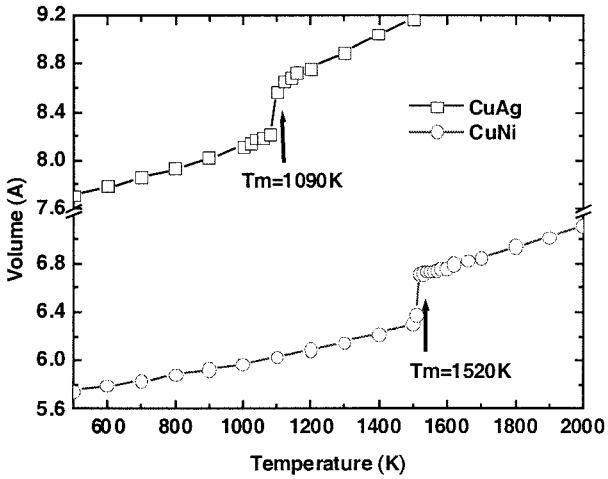

Figure 3-1 Volume vs. Temperature during heating for CuAg and CuNi. CuAg melts at 1090K and CuNi melts at 1520K.

We also slowed down the heating process, particularly for CuNi around 1500K, and showed the changing of structure factor S(K) for K vector of (10 0 0) and (5 5 5) as a function of time in Figure 3-2. For a perfect FCC crystal, the structure factor can accumulate to N, the number of atoms (500 in this case), for some K directions, but should be zero for a disordered structure. We can see this change in melting process. From MD runs at 1500K, 1510K and 1520K, we found S(K) drops to zero at the same point where the volume and energy increase during melting, and the transition of S(K) during melting occurred in an extremely rapid time scale, less than 0.05ps.

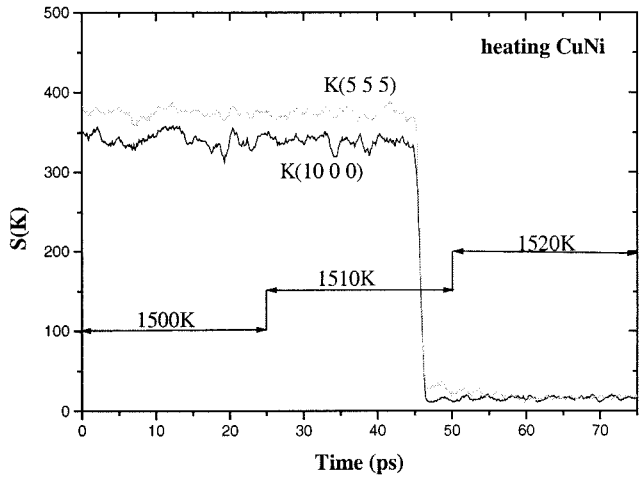

Figure 3-2 Structure factor S(K) as a function of time for the heating simulation of NiCu for 1500K,1510K and 1520K. Melting occurs after 21ps at 1510K, with a sharp drop to zero.

In our simulation, melting is a homogenous transition, and normally gives higher melting temperature than the experiments. One reason for the melting temperature being a bit high is that our system is homogeneous without a free surface. In addition, we started with a perfect crystal; given the rapid rate of heating, the system might not have had time to generate an equilibrium distribution of defects, thus leading to a slightly higher Tm. In the absence of defects such as grain boundary, free surface, void or dislocations, the mechanism of melting is mechanical melting instead of the thermodynamic melting, which normally occurs in experiments. Mechanical melting is driven by an intrinsic elastic instability in the system, or the vanishing of shear modulus; for cubic system this means either $(C_{11}-C_{12})/2=0$ or $C_4=0$. This was pointed

out by Born [3-24] 50 years ago, as the absolute limit to superheating for any crystal structure.

3.5 Crystallization in pure Cu and NiCu

We quenched the liquid CuNi alloy and pure Cu using a cooling rate of $4*10^{12}$K/s as the reverse processes of cooling. Cooling CuNi alloy from the melt (Figure 3-3a) shows a sharp drop in volume at 500K. To provide a continuous view of the crystallization in CuNi, Figure 3-3b shows the RDFs calculated at 1800K, 600K, and 400K during cooling process [and compared with the structure we started (in heating cycle) with at 500K. The RDF at 1800k shows broad peaks, which is the pair distribution for liquid structure with no ordering. At 600K RDF for suppercooled liquid shows a little split in the second peak, indicating a structure with some local order. The transformation from liquid to crystal is very clear in the RDF at 400K, in which the peaks formed in cooling well overlapping those from the original crystal in heating cycle.

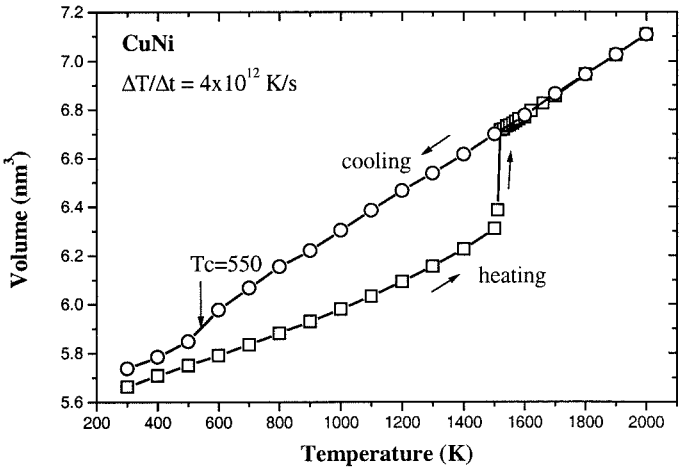

(a)

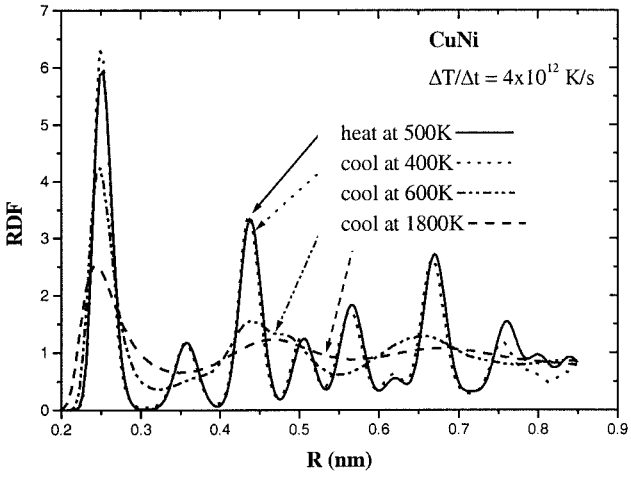

(b)

Figure 3-3 Melting and cooling (at the quenching rate of $4*10^{12}$K/s) of NiCu leads to crystallization at ~500K. (a) Volume versus temperature in heating and cooling cycles. (b) RDF of NiCu at 500K in heating cycle and at 1800K, 600K and 400K in the cooling cycle.

Similarly, the results for Cu (Figure 3-4a) show a sharp change in the volume as the temperature is lowered below 600K. The RDF (Figure 3-4b) for this system clearly shows that at 500K the cooled Cu has crystallized, with the peaks on RDF at 500K from cooling cycle overlapping well with those in heating cycle. Pure monatomic metallic liquids have not in practice been quenched into a glass because they exhibit a relatively low reduced glass temperature, Trg=0.25. This means the glass transition temperature in pure Cu is close to 337K, which is lower than the crystallization temperature 650K; thus no glass transition can occur.

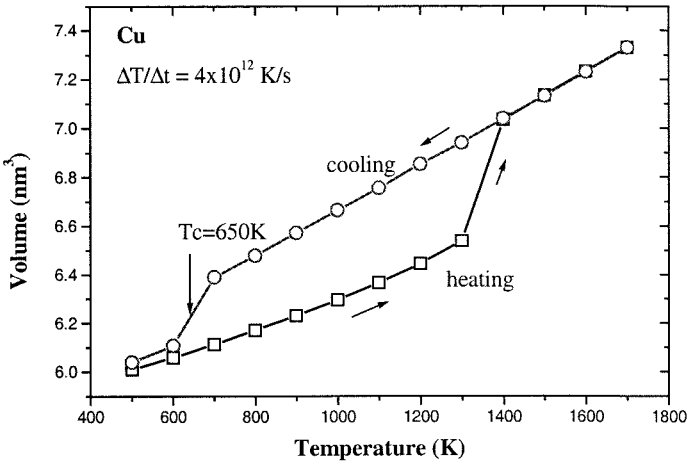

(a)

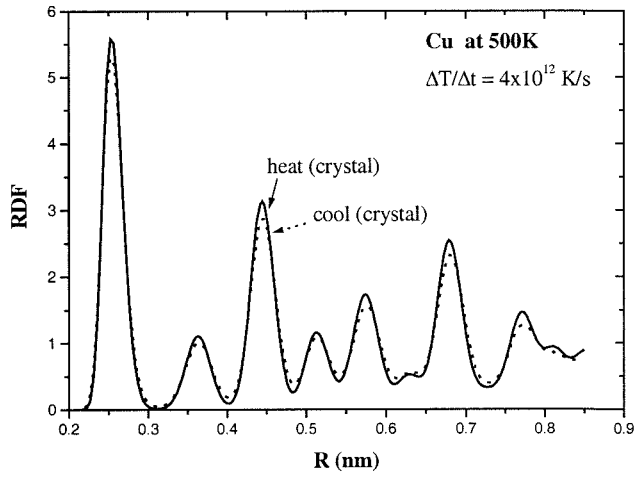

(b)

Figure 3-4 Melting and cooling: quenching rate of pure Cu at 4*1012K/s leads to crystallization at 600K. (a)Volume versus temperature during heating and cooling cycle. (b) RDF at 500K for structure obtained during heating and cooling cycles.

To understand the progression of melting, we calculated the S(K) from trajectory as a function of time in Figure 3-2 and showed melting is a homogenous transition

without free surface. Crystallization is the opposite process of melting. The structure factor S(K) will increase as the atoms order in appropriate planes. In our calculation, the K vectors here are defined with respect to the axes of the box. Since the new crystal need not form in the same orientation of the original box, the K vectors, on which the S(K) grow, are different with the original ones. We found K-vectors such as (2 –2 8), (11 3 0) and (4 6 –4) will accumulate to the number of particles in system after crystallization. Figure 3-5 displays the values for some S(K) are traced for 700K, 600K, 500K, and 400K. The atoms became ordered on specific planes, leading to increase in structure factor for the K-vectors representing these planes. As the nuclei form and grow, these S(K) increase. Figure 3-5 shows that crystallization process starts at 25ps and completes at 75ps. Different with melting process, it takes about 50ps for S(K) to reache 450 from 0, indicating crystallization is a heterogeneous process.

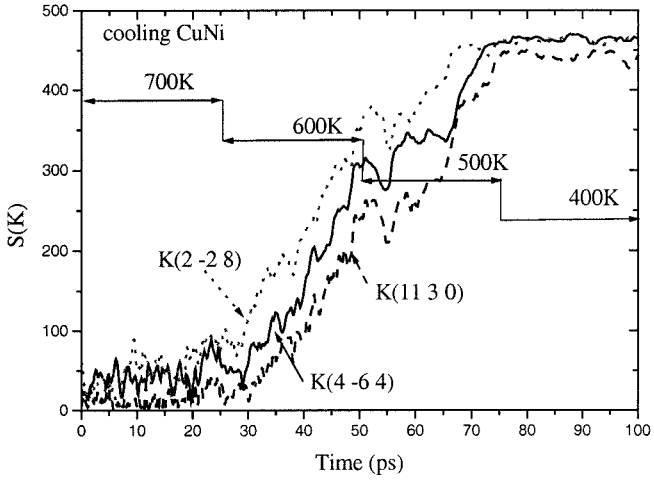

Figure 3-5 Structure factor S(K) as a function of time for the cooling simulation of NiCu from 700K to 400K. Crystallization starts at 25ps and is completed at 75ps.

Since we kept the simulation under a constant cooling rate, crystallization is not always under equilibrium states, but becomes cooling rate dependent. For this reason, we also studied the dependence of crystallization temperature on the cooling rate. Figure 3-6a shows the volume versus temperature curve for various cooling rates. Here the crystallization temperature Tc is the temperature at which the density increases suddenly. Tc is decreasing as the cooling rate increases.

To examine crystallization in detail, we again calculated the structure factor for a set of K vectors. Using a time increment of 25ps for each temperature step, the crystallization occurred after 8ps at 600K (based on the drastic increase on S(K) for specific K vectors) (Figure 3-7b). In fact, we see that the nucleus for crystallization had already formed at the end of the 700K run. To show this, we followed the 25ps at 700K with another 25ps simulation at 700 K. We find (Figure 3-6c) that the structure factor grows to 450 after 10 additional ps (total of 35ps), essentially the same as for the 650K case. The K vectors, or the orientation of the newly formed crystal, in these two runs are identical, indicating that the nucleus had already formed by the end of the first 25ps at 700K. According to the value of S(K), the size of the nucleation is about 100~200 atoms. We also carried out a third calculation shown in Figure 2-6d. Here we started with the final structure at 800K after 25ps and continued an additional 50ps at 800K. In Figure 3-6d we denote the start of this last 50ps as 0 in order to compare with Figures 8a and 8b. We see that this took 48ps to crystallize (longer than the 33 or 35ps for 650K or 700K), but the final crystal has different K vectors. This indicates that a different nucleus formed.

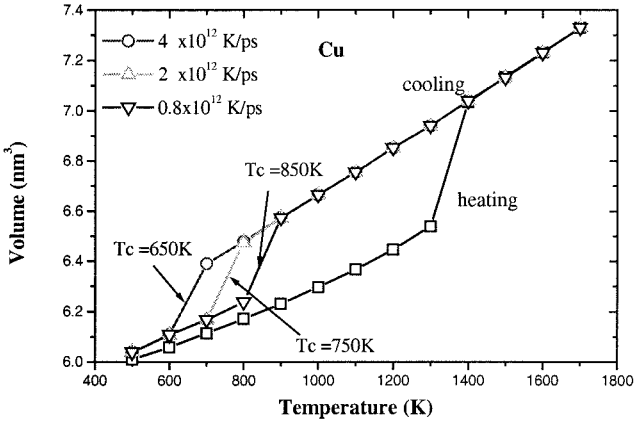
4 x10^12 K/ps
2 x10^12 K/ps
0.8x10^12 K/ps
Cu
cooling
heating
Tc =850K
Tc =650K
Tc =750K
Volume (nm^3)
Temperature (K)

(a)

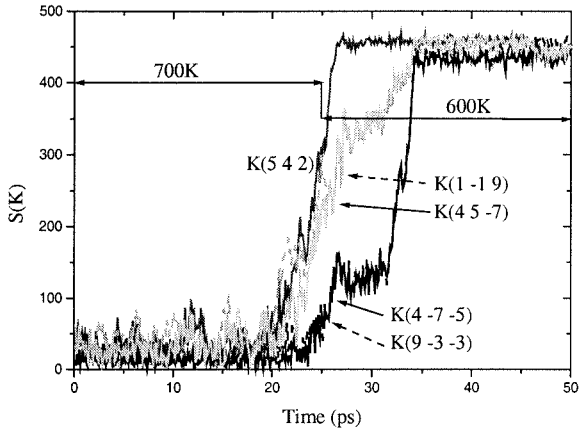
700K
600K
K(5 4 2)
K(1 -1 9)
K(4 5 -7)
K(4 -7 -5)
K(9 -3 -3)
S(K)
Time (ps)

(b)

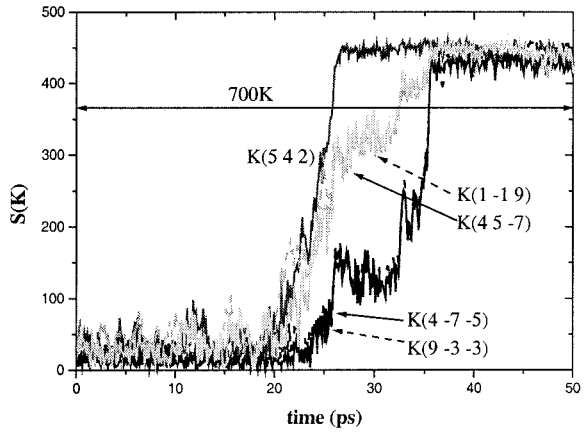
700K
K(5 4 2)
K(1 -1 9)
K(4 5 -7)
K(4 -7 -5)
K(9 -3 -3)
S(K)
time (ps)

(c)

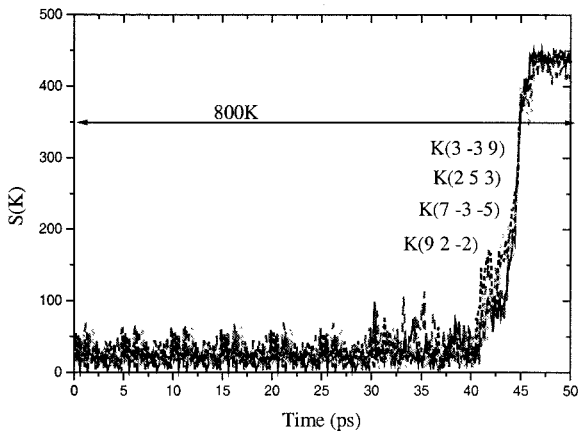

(d)

Figure 3-6 Effect of cooling rate on crystallization temperature for pure Cu. (a) Volume changing of Cu at different cooling rate. (b) Change in structure factor for different simulation of crystallization. Normal cooling rate with 25ps at 700K followed by 25ps at 600K. Crystallization is completed at 33ps. (c) The same 25ps run at 700K followed by second 25ps again at 700K. The same K values appear as for case (b) indicating the same nucleus. (d) After the first 25ps at 800K, an additional 50ps were carried out at 800K rather than cooling to 700K and 600K. The crystallization was complete at T~45ps. The values are different for (b) and (c) indicating a different nucleus.

3.6 Glass formation in CuAg

In contrast with crystallization observed in pure Cu and CuNi alloy, we also quenched liquid Cu_4Ag_6 alloy using the same cooling rates as for NiCu and pure Cu. Notice here the atomic size ratios are Ag/Cu=1.129, Cu/Ni=1.025 and Cu/Cu=1.0.

Figure 3-7 shows the variation of the volume as Cu_4Ag_6 is heated and cooled. In contrast to the volume jumping in heating process, we see that cooling leads to a continuous change in volume. However, for Cu_4Ag_6, the slope of the volume versus temperature curve decreases below 500K. This is a sign of glass formation. The glass transition temperature is a general phenomenon observed when a liquid is cooled beyond its freezing temperature and does not crystallize. Because the glass is actually frozen liquid, where the change in configurational entropy vanishes, the derivative of entropy with respect to pressure is just the derivative of volume with respect to temperature. Thus the slope of volume vs. temperature decreases after the glass transition.

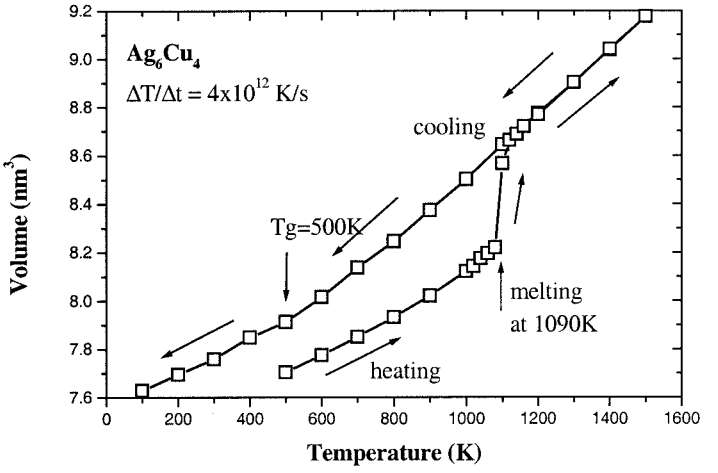

(a)

Figure 3-7 Average volume during heating and cooling of Cu_4Ag_6 at a rate of $4*10^{12}$K/s. Upon cooling, the liquid is supercooled until 500K where it transforms to a glass.

Figure 3-8 shows the RDF of the model structure during the heating and cooling processes. The RDF shows an FCC crystal structure as the sample is heated from 300K to 900K. However, at 1200K (just above melting) we see the emergence of broad peaks, signifying the melting of structure. The sample was heated up to 1500K and cooled back to 1200K, leading to the same structure as for heating, indicating still a disordered liquid structure. Cooling down to 900K, we still see the structure of a liquid, in fact a supercooled liquid. However, after cooling to 300K, we see that the second peak of RDF is split. This splitting of the second peak, due to exists of local ordering, is a well-known characteristic feature in the RDF of a metallic glass. Thus, quenching the Ag_6Cu_4 alloy from the liquid to 300K at the rate of $4*10^{12}$K/s leads to a metallic glass.

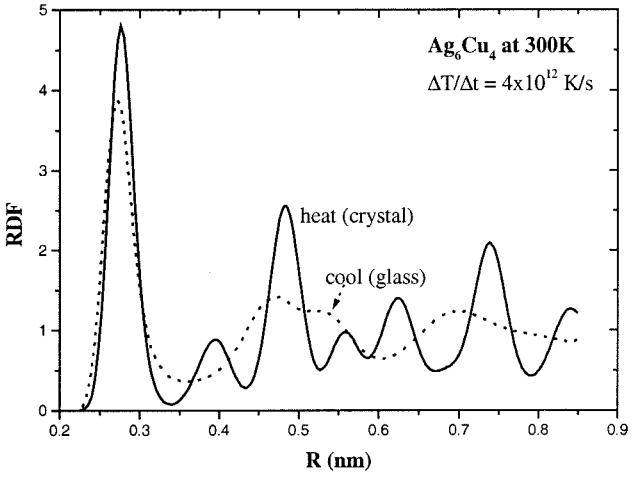

(a)

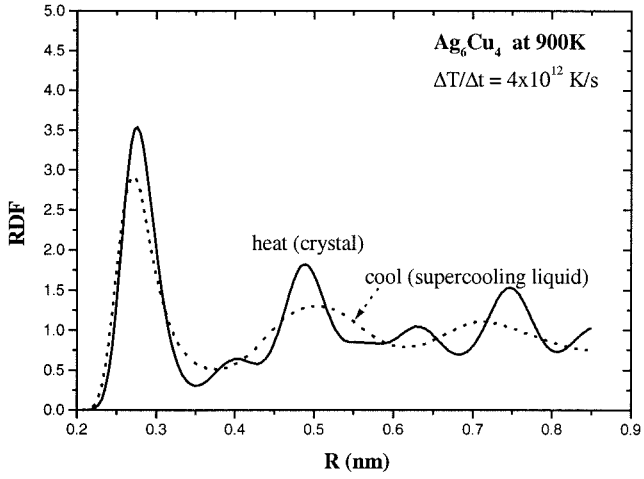

(b)

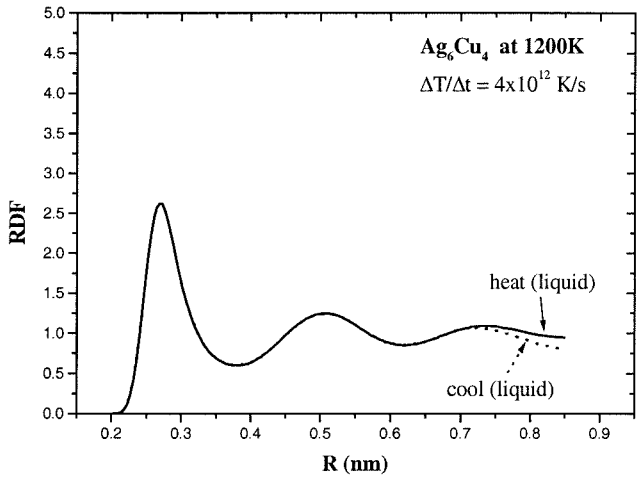

(d)

Figure 3-8 RDF during heating and Cooling of Cu_4Ag_6 at a rate of $4*10^{12}$K/s, *heat* denotes a random FCC crystal in the heating cycle and *cool* denotes the metallic glass at the end of cooling cycle. (a) RDF at 300K, both are FCC crystal, (b) RDF at 900K, structure in heating cycle is still FCC and structure in cooling cycle is supercooled liquid, (c) RDF at 1200K, both structures are in liquid states.

We have considered several cooling rates to investigate its effect on the glass transition temperature Tg. Figure 3-9a shows the volume versus temperature curve. Each rate leads to a slightly different value for the temperature at which the slope changes. A parameter often used to define the glass transition temperature is the Wendt-Abraham parameter [3-25] defined by $R=g_{min}/g_{max}$. Here $g_{min}(g_{max})$ is the value of g(r) at the first minimum (maximum) in the RDF. Since the nature of local ordering is also characterized by the shape of the first peak in RDF, the Wendt-Abraham parameter stresses the local character of g(r), permitting a direct comparison between structures and leading to a better estimate of glass transition temperatures. The Wendt-Abraham transition temperature, Tg^{WA}, is displayed in Figure 3-9b for each cooling rate. Thus, we see that $Tg^{WA} \cong 500K$ at $\Delta T/\Delta t = 2*10^{12}K/s$, $Tg^{WA} \cong 550K$ at $\Delta T/\Delta t = 4*10^{12}K/s$, and $Tg^{WA} \cong 700K$ at $\Delta T/\Delta t = 4*10^{14}K/s$. Thus, the glass transition temperature increases with increased cooling rate. The fastest cooling rates result in shorter times for the atoms to relax, thus leading to formation of the glass at a higher temperature than at lower cooling rate.

3.7. Conclusion

We have applied the modified SC potential for Cu, Ni, and Ag to study the phase transformation in Ag6Cu4 and CuNi alloy and pure Cu. At the same cooling rate, Ag6Cu4 form metallic glass while Cu and CuNi form FCC crystal. The glass transition temperature and crystallization temperature are highly affected by the quenching rate.

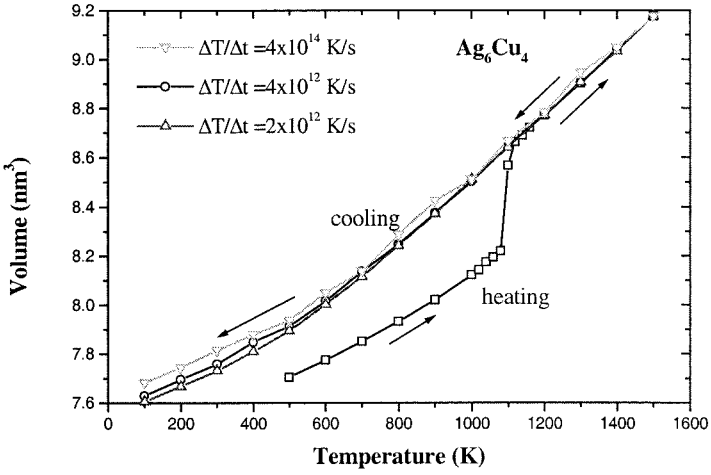

(a)

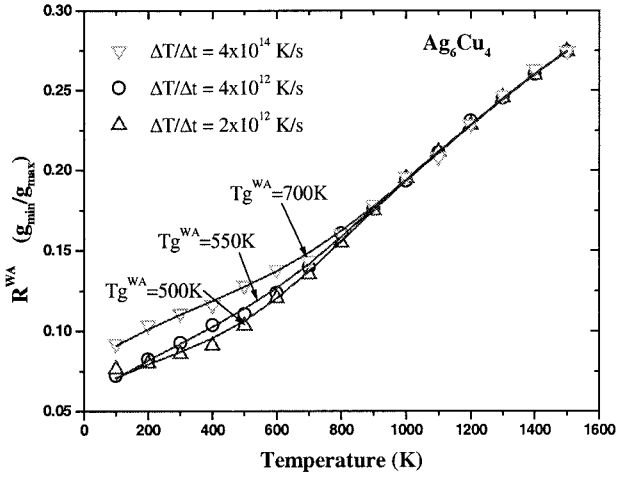

(b)

Figure 3-9 Dependence of glass transition temperature on cooling rate. (a) Volume versus temperature for Ag_6Cu_4 obtained from three different quenching rates. (b) Wendt-Abraham parameter R versus temperature. The calculated Tg^{WA} for three different cooling rates are 500K, 550K and 700K.

References:

[3-1] "Metallic Glasses" American Society for metals, Metals Park, Ohio, (1978)

[3-2] W. Clement, R. H. Willens, and P. Duwez, Nature **187**, 869 (1960).

[3-3] A. Peker and W. L. Johnson, Appl. Phys. Lett. **63**, 2342 (1993); also X. H. Liu and W. L. Johnson, J. Appl. Phys. **78**, 6514 (1995)

[3-4] C. Kittel, Introduction to solid state Physics, 7th ed (Wiley, New York, 1996), W. B. Pearson, Crystal Chemistry and Physics of Metals and Alloys (Wiley, New York, 1972)

[3-5] H. Choiyim and W. L. Johnson, Appl. Phys. Lett. **71**, 3808 (1997); also X. Sun, S. Schreider, U. Geyer, W. L. Johnson and M. A. Nicolet, J. Mat. Res. **11**, 2738 (1996)

[3-6] K. Vollmayr, W. Kob, and K. Binder, J. Chem. Phys. **105**, 4714 (1996)

[3-7] W. C. Swope and H. C. Andersen, Phys. Rev. B **41**, 7042 (1990)

[3-8] M.S. Watanabe and K.Tsumuraya, J. Chem. Phys. **87**, 4891 (1987)

[3-9] H. C. Chen and S. K. Lai, Mater. Sci. Eng. A **179**, 261 (1994)

[3-10] A. C. Brown and R. D. Mountain, J. Chem. Phys. **80**, 1263 (1984)

[3-11] J. Lu and J.A. Szpunar, Phil. Mag. A **75**, 1057 (1997)

[3-12] L. J. Lewis, Phys. Rev. B **39**, 12954 (1989)

[3-13] T. Aihara, K. Aoki and T. Masumoto, Mater. Sci. Eng. A **179**, 256 (1994); T. Aihara, K. Aoki and T. Masumoto, Mater. T. JIM **36**, 399 (1995); T. Aihara, Y. Kawazoe, T. Masumoto, J. Non. Cryst. Solid. **207**, 875 (1996)

[3-14] H. Teichler, Phys. Rev. Lett. **76**, 62 (1995); H. Teichler, Phys. Rev. E **53** 4287 (1996)

[3-15] M. Shimono and H. Onodera, Mater. Trans. JIM **39**, 147 (1998).

[3-16] R. G. Dellavalle, D. Gazzillo and G. Pastore, Mater. Sci. Eng. A **165**, 183 (1993)

[3-17] A. P. Sutton and J. Chen, Phi l. Mag. Lett. **61**, 139 (1990); H. Rafii-Tabar and A. P. Sutton, Phil. Mag. Lett. **63**, 217 (1991); Y. Kimura, T. Cagin, Y. Qi and W. A. Goddard III, Phys. Rev. B, submitted

[3-18] D. Turnbull and J. C. Fisher, J. Chem. Phys. **17**, 71 (1949); also D. Turnbull, J. Chem. Pys. **18**, 198 (1950)

[3-19] T. Egami and Y Waseda, J. Non Cryst. Sol. **64**, 113(19), T. Egami, Mat. Sci. Eng. A **226**, 261 (1997)

[3-20] P. Duwez, R. H. Willens and W. Klement Jr., J. Appl. Phys. **31**, 1137 (1960)

[3-21] J. R. Ray and A. Rahman, J. Chem. Phys. **82**, 4243 (1985)

[3-22] S. Nosè, Mol. Phys. **52**, 255 (1984); S. Nosè, J. Chem. Phys. **81**, 511 (1984)

[3-23] M. Parrinello and A. Rahman, Phys. Rev. Lett. **45**, 1196 (1980); M. Parrinello and A. Rahman, J. Appl. Phys. **52**, 7182 (1981)

[3-24] M. Born and K. Huang, "Dynamical Theory of Crystal Lattices", Clarendon Press, Oxford (1954)

[3-25] H. R. Wendt and F.F.Abraham, Phys. Rev. Lett. **41**, 1244 (1978)

Chapter 4 Size Dependence of Melting and Crystallization of Ni nanoclusters

4.1 Introduction

Particles with diameters of 1 nanometer ~ 10 nanometer exhibit properties that are often intermediate between molecular and crystalline. The properties of such mesoscale nanoparticles are expected to evolve gradually from molecular to solid like as the particle number increases, but it has been difficult to study the mesoscale region experimentally. It is well established that in the nanometer range the melting temperature decreases dramatically with the decreasing radius of the cluster [4-1], but there is little quantitative data on the structures and energetics of the bulk and surface regions important to the properties of such system. Since transition metal clusters have a number of exciting potential applications in nanoscale electronic devices and catalysis [4-2]~[4-5], it is important to develop quantitative understanding of the thermodynamic and structural properties of such metal clusters. Thus, in this paper we carry out molecular dynamics (MD) simulations using an accurate many-body force field to study melting and crystallization processes for Ni nanoclusters containing up to 8007 atoms (5.74 nm diameter). We find that at the upper of this range, the properties can be described accurately in terms of macroscopic concepts with well-defined bulk plus surface thermodynamic properties.

When the crystal-vapor surface energy (γ_{xv}) exceeds the sum of the liquid-vapor (γ_{Lv}) and crystal-liquid (γ_{xL}) surface energies, ($\Delta\gamma=\gamma_{xv} - (\gamma_{Lv}+\gamma_{xL})>0$, then the formation of liquid skin on a planar or curved solid surface is energetically favorable. Using experimental bulk surface energies [4-6], and assuming that the driving force

for melting on a surface is the reduction in the total interfacial energy, these considerations suggest that Au($\Delta\gamma$=33mJ/m^2), Sn($\Delta\gamma$=18mJ/m^2), Pb($\Delta\gamma$=22mJ/m^2), and Pt($\Delta\gamma$=29mJ/m^2) would favor surface melting. Indeed, experiments on Au[4-1], Sn[4-7][4-8], Pb[4-9], Pt[4-10] and Na[4-11] small particles, show melting at considerably lower temperature than bulk systems, suggesting that the melting process starts on the surface. By the surface energy criterion bulk Na($\Delta\gamma$=-8mJ/m^2) and Ni($\Delta\gamma$=-2mJ/m^2) are *not* expected to exhibit surface melting on planar surface. However, small particles of Na[4-11] also show melting at much lower temperature than bulk systems, and the results have not yet been established for Ni. Experimental studies have not yet been reported on Ni, and previous melting simulations have been reported for small Ni clusters with 7~23 atoms [4-12] and 55 atoms [4-13], but no systematic study of the size dependence of melting and crystallization behaviors has been reported for Ni. Hence we decided to study Ni using MD simulations to determine if surface melting is a general phenomenon in small particles.

In this chapter we apply molecular dynamics (MD) methods using the quantum Sutton-Chen (QMSC) many-body force field to simulate melting and crystallization processes for Ni nanoclusters containing up to 8007 atoms (5.74 nm diameter). In particular, we examine how the melting temperature and heat of fusion depend on cluster size, including pre-melting prior to the transition. Then we examine the local structures formed upon solidification and the melting temperature during reheating of the newly formed crystals. This chapter is arranged as follows: section 4.2 summarizes various details of the calculations, while section 4.3 describes the results for melting and crystallization of Ni clusters, with comparisons to results of bulk Ni.

The implications are discussed in section 4.4 and the conclusion in section 4.5.

4.2 Computational methods

4.2.1 Dynamics

We use the quantum corrected Sutton-Chen (QMSC) many-body force field [4-14] with parameters empirically fitted to data on density, cohesive energy, compressibility, and phonon dispersion. QMSC leads to accurate values for surface energies, vacancy energy, has previously been applied to studies of melting, glass transformation, and crystallization for bulk NiCu and CuAg alloys [4-15] and for studying plasticity and strain rate induced amorphization in one-dimensional nanorods [4-16].

The MD calculations [4-17] were performed using the MPiSim software developed at Caltech [4-18]. The calculations were carried out using two flavors of dynamics.

(a) All nanoclusters were generated with geometries constructed from a large FCC block of Ni, using various spherical cutoff radii centered at a tetrahedral interstitial site. This leads to smooth but faceted surface structures. The cluster is then put into a much larger cubic unit cell to simulate isolated particles in vacuum. These nanoclusters were simulated using an MD Hamiltonian with constant temperature (T for Hoover [4-17]), constant shape (h), and constant particle number (ThN MD) *without* periodic boundary conditions. Here the simulation cell is kept constant, but the cluster can adjust its volume to keep a zero pressure, within the constant unit cell.

(b) For the simulations of the bulk system, we used a cubic periodic super cell,

containing 500 atoms with FCC structure. The bulk systems were studied with periodic boundary conditions using an MD Hamiltonian with constant temperature (T for Hoover [4-17]), constant stress (t for Rahman-Parrinello[4-17]) and constant particle number (TtN MD).

The MD equations of motion were integrated using a fifth-order predictor-corrector algorithm with a time step of 1.0 fs. This led to quite stable dynamics trajectories.

We considered clusters ranging from 336 atoms (2.144 nm diameter) to 8007 atoms (5.74 nm diameter). After equilibrated at 300K for 25ps, the clusters were subjected to a heating-cooling cycle consisting of a series of ThN (TtN MD for bulk system) simulations with temperature increments of ΔT = 100K and equilibration simulation times of dt = 25ps. However, for the temperature region near the melting point, we used smaller temperature increment, ΔT, but for shorter times Δt so that the heating rate remains constant at $\Delta T/\Delta t$ = 4K/ps (e.g., 20K for 5ps).

4.2.2 Analysis of thermodynamic quantities

To calculate the heat capacity, we fitted smooth cubic splines to the average potential energy during the heating process as a function of temperature and then obtained the derivative from this fitted curve:

$$C_p(T) = \frac{d(PE)}{dT} + \frac{3R}{2} \qquad (4\text{-}1)$$

We defined the melting point as the temperature with the maximum apparent heat capacity.

To obtain ΔH_{melt} (the heat of fusion at T_{melt}), we fitted the potential energy to two linear functions of T in both solid and liquid phases (above and below the transition temperature) and determined the difference at T_{melt}. To calculate the entropy change at the transition, we used $\Delta S_{melt} = \Delta H_{melt} / T_{melt}$ together with the computed values for the energy of fusion.

We defined the radius of the cluster as

$$R_c = R_g \sqrt{5/3} + R_{Ni}, \qquad (4\text{-}2a)$$

where R_g is the radius of gyration, defined as

$$R_g^2 = \Sigma_i (R_i - R_{cm})^2 / N \qquad (4\text{-}2b)$$

And the atomic radius R_{Ni} is half the atomic distance in bulk system, $R_{Ni} = 1.25$Å. Comparing the surface area calculated from (4-2a) with the solvent accessible surface (using R_{Ni} as solvent radius), we find a difference of less than 5%. Thus, we have used R_c to calculate the internal volume and surface area as a function of temperature.

4.2.3 Analysis of dynamic characteristics

To analyze how the atomic motions change near the melting point, we partitioned the cluster into 6 radial shells of equal ΔR. Within each shell we calculated the average root-mean-square thermal displacement (RMSD) as in (4-3)

$$\mathrm{RMSD}_{\mathrm{shell}}(dt) = \frac{\sum_{i \in shell} RMSD_i(dt)}{N_{shell}} \qquad (4\text{-}3a)$$

where

$$\mathrm{RMSD}_i(dt) = \sqrt{\left\langle \sum_{t=0}^{tend-dt} (r_i(t+dt) - r_i(t))^2 \right\rangle} \qquad (4\text{-}3b)$$

To obtain RMSD we averaged over a 25ps trajectory and used *dt* as 10ps, which is sufficiently long for diffusion in the liquid phase. This provides a rough measure of the diffusion constant, which increases monotonically with the distance from the center. The RSMD changes dramatically upon melting, indicating a first order phase transformation.

4.2.4 Analysis of structural characteristics

To investigate the local geometric structure, we developed an FCC searching algorithm to group atoms within one FCC grain and identify the stacking fault and grain boundary [4-16]. In this method we first define an atom having 12 nearest neighbors with an ABC packing sequence as a part of a perfect FCC crystal; from it we check the atoms in far nearest neighbors, and stop at the atoms, which lost the FCC nearest neighbors configuration. Using this method we can define the FCC grains in the system, and find twinning or grain boundaries.

We also used the Honeycutt-Andersen [4-19] index to distinguish between the local icosahedral and FCC structures. The HA index has four numbers to characterize the environment for each pair of atoms. The first number shows the distance of two atoms; 1 means they are the first nearest neighbor (bonded pair) and 2 means they are the second nearest neighbor (not bonded pair). The second number indicates how many bonded atoms the two atoms share. The third index is the bond number among the shared atoms. And the fourth number is the added information to distinguish bonds configuration when the first three numbers are the same. This has proved useful tool for other studies of local structures [4-19].

4.3 Results

4.3.1 Size dependence of cluster melting

The analysis is illustrated in Figure 4-1, which compares the potential energy for heating and cooling of the 1004 atom cluster with the corresponding results for bulk Ni. The melting transition is clearly identified by a rapid increasing in energy, which is well defined but much broader than for the bulk system. We define the melting temperature, T_{melt}, as the maximum in the heat capacity Cp (T), leading to T_{melt} = 1160K. Figure 4-1 shows that the potential energy begins to deviate from linearity at 800 to 900K, but the Cp indicates that melting starts (becomes nonlinear) at ~ 1000K and extends to over 1200K. This indicates a heterogeneous melting process.

Figure 4-1 also shows the calculated heating curve for bulk Ni. These periodic boundary condition calculations provide no free surface for bulk Ni leading to an abrupt (~40K width) homogeneous melting transition at a temperature of T_{melt} = 1760K, which is 32K (1.8%) higher than the experimental melting temperature of T_{melt} = 1728K for pure Ni. Such a higher melting temperature might be consistent with surface melting depressing the experimental value.

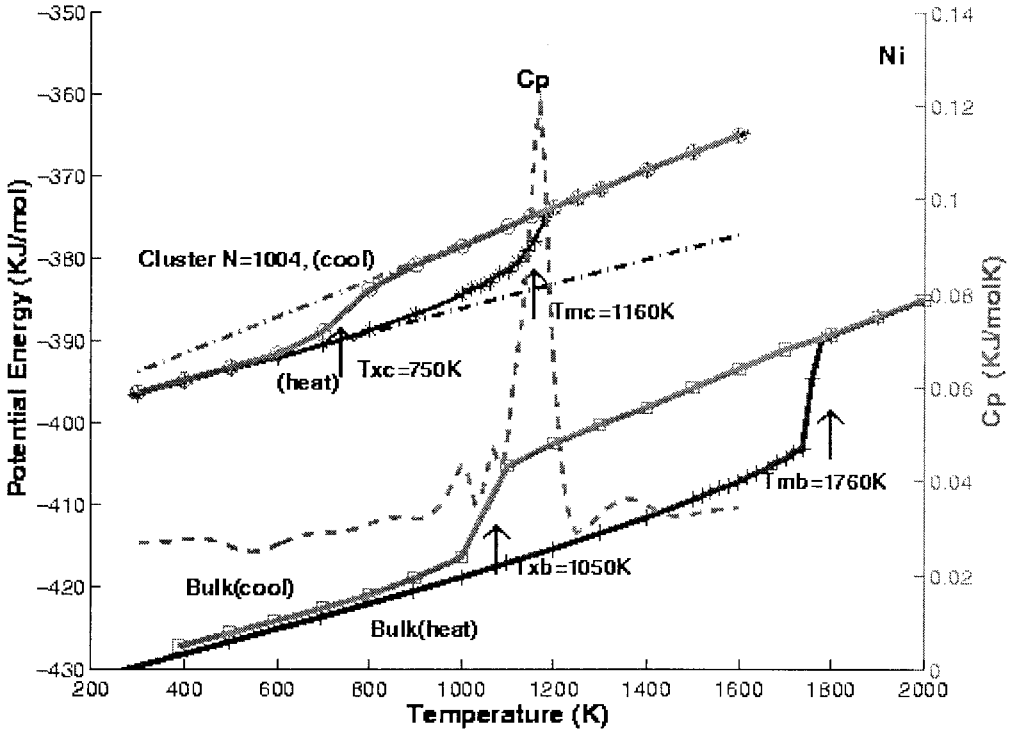

Figure 4-1 Potential energy U(T) and heat capacity Cp(T) for heating and cooling cycles of a cluster with N=1004 Ni atoms and the bulk fcc phase of Ni.

The total potential energy per atom of the cluster is higher than that of the bulk system due to the surface energy. For the 1004 atom system, the difference at 300K is 33.6 kJ/mol. Using the calculated radius of 14.97Å (2816 $Å^2$ surface area), we obtain a surface energy of 1990mJ/m^2, which compares well with the experimental surface energy for bulk Ni of 2104mJ/m^2 and the calculated value for bulk Ni (same FF) of 2202mJ/m^2 [4-14]. The surface energy predicted for the various clusters at 300K and 1500K are shown in Table 4-1. At 1500K, we compared the liquid clusters with super-cooled liquid bulk Ni to obtain the surface energy of liquid Ni. This leads to γ_{LV} =1537mJ/m^2 for cluster with 1004 atoms, which can be compared to the

calculated surface energy at 1500K for bulk Ni of 2057mJ/m^2 and the experiment value for bulk liquid Ni of 1750 mJ/m^2.

Table 4-1 also shows how the various properties change with cluster size. The melting temperature drops dramatically with cluster size in the nano scale region, leading to a T_{melt} for 1004 atoms, that is ~ 34% lower than for bulk Ni.

Figure 4-2a shows that the melting temperature of Ni clusters scales linearly with $N^{-1/3}$. Extrapolating the results in Figure 4-2a for finite clusters to N = ∞ ($N^{(-1/3)} = 0$) predicts a bulk melting point of 1590K, significantly below the calculated value of 1760K for bulk Ni. This is partly because the finite cluster calculations have a free surface, whereas the bulk calculations do not. In order to predict the dependence of T_m^c on size, we write the free energies of solid and liquid clusters as the sum of central bulk region and surface. The superscript of b, c, and s represents bulk, cluster and surface respectively [4-20].

$$G_{solid,}^{cluster} = G_X^b + G_X^S = N\mu_x^c + \gamma_{xv} A$$

$$G_{liquid,}^{cluster.} = G_L^b + G_L^S = N\mu_L^c + \gamma_{Lv} A \qquad (4\text{-}4a)$$

where μ is the free energy per atom of bulk Ni and A is the crystal surface area. Thus, at T_m^c, the melting temperature of the cluster, we have

$$(\gamma_{xv} - \gamma_{Lv})A = N(\mu_{Lb} - \mu_{xb}) = N(T_m^b - T_m^c)(S_L^b - S_x^b) \qquad (4\text{-}4b)$$

where we used

$$\Delta H_{f,}^{bulk} = (H_L^b - H_x^b) = T_m^b (S_L^b - S_x^b) = T_m^b \Delta S_f^{bulk} \qquad (4\text{-}4c)$$

and S_b is per atom. Hence,

$$T_m^c = T_m^b - \frac{(\gamma_{xv} - \gamma_{Lv})}{(S_L^b - S_x^b)} \frac{A}{N} \qquad (4\text{-}5a)$$

Assuming a spherical cluster leads to a specific surface area of

$$\frac{A}{N}=\frac{3V_{AT}}{R}=\frac{(36\pi V_{AT}^2)^{1/3}}{N^{1/3}} \tag{4-5b}$$

where V_{AT} is the volume per atom. Thus,

$$T_m^{\ b} - T_m^{\ c}(N) = \alpha N^{(-1/3)} \tag{4-6a}$$

where a is a constant,

$$\alpha=\frac{(\gamma_{Xv} - \gamma\gamma_{Lv})}{\Delta S_{Lx}^{\ b}}(36\pi\ V_{AT}^2)^{1/3} \tag{4-6b}$$

Figure 2a shows that (6a) leads to a good fit to the calculations for the range of 336 to 8007 atoms, with a = 4220.2 K. This value of a, with $S_f^{bulk} = \Delta H_f^{bulk}/T_m^{\ b}$=9.83 J/mol-K from our calculations and the average density calculated at the melting temperature from our calculation ($\rho = 1.09*10^5 mol/m^3$) lead to $(\gamma_{xv} - \gamma_{Lv}) = 233 mJ/m^2$.

Alternatively, we can estimate $(\gamma_{xv} - \gamma_{Lv})$ from Eq. 4-7 for each size (derived from Eq. 4-5a) leading to a surface energy difference of

$$(\gamma_{Xv} - \gamma_{Lv}) = \frac{\Delta S_f^{\ bulk}(T_m^{\ b} - T_m^{\ c})N}{4\pi R^2} = 189\ mJ/m^2 \text{ for } N = 1004 \tag{4-7}$$

(using the fitted value of $T_m^{\ b}$ = 1590K). Table 4-1 shows the $(\gamma_{xv} - \gamma_{Lv})$ calculated for various clusters, which increases with cluster size.

Figure 4-2b shows the differences of heat of fusion, entropy of fusion and melting temperature for clusters compared with bulk as a function of cluster size. Considering that the cluster is composed of surface and bulk regions, and considering that the core part has the same heat of fusion and surface energy as the bulk phase, the enthalpy can be written as

$$H_{solid,}^{\ cluster} = H_x^{\ c} + \gamma_{xv} A$$

$$H_{liquid,}^{\ cluster.} = H_L^{\ c} + \gamma_{Lv} A \qquad (4\text{-}8)$$

This leads to a heat of fusion for Ni clusters that scales linearly with $N^{-1/3}$,

$$\Delta H_f^{\ b} - \Delta H_f^{\ c}(N) = bN^{(-1/3)} \qquad (4\text{-}9)$$

From Figure 4-2b, we see that this linear relation is obeyed above 736 particles, but that the smaller clusters are more stable than what is suggested by Eq. 4-9. This will be discussed in section 4.4.1.

From Eq. 4-5 and Eq. 4-9, the entropy of fusion should have the form

$$\Delta S_f^{\ b} - \Delta S_f^{\ c} = \frac{bN^{(-1/3)} + a\Delta S_f^{\ c} N^{(-1/3)}}{T_m^b - aN^{(-1/3)}} \qquad (4\text{-}10)$$

Figure 4-2b shows that this relation (the dotted line) is obeyed above 736 particles and the smaller clusters have lower entropy.

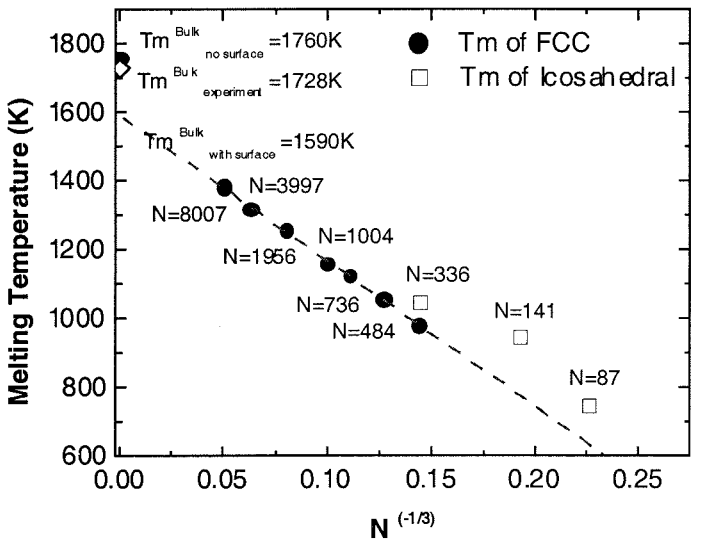

(a)

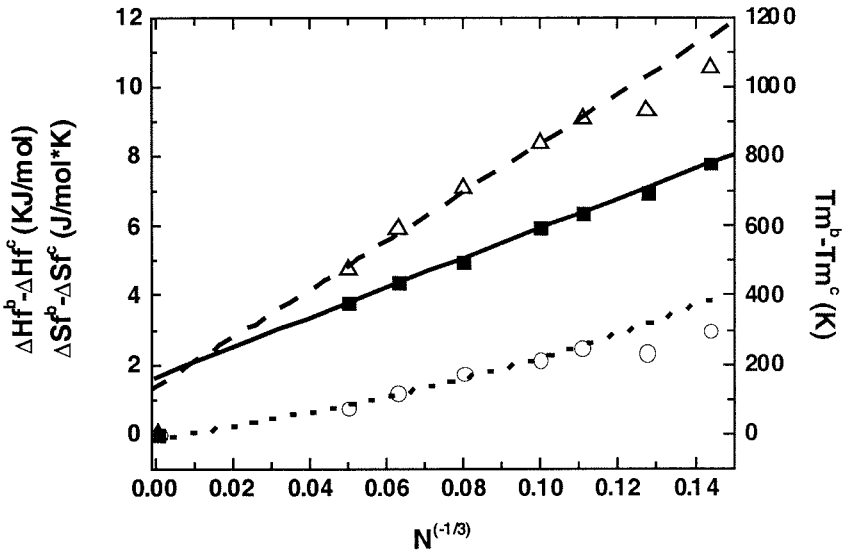

(b)

Figure 4-2a Dependence of melting temperature on cluster size. The dashed line shows the best fit to a linear function of $N^{(-1/3)}$. This leads to a predicted value for large N of 1590K, well below the value 1760K calculated for the bulk system (no surface). The melting temperature for N=336(ico), N=141 and N=87 are all higher than the Tm predicted from linear fitting.

Figure 4-2b Tm^b-Tm^c, ΔH_f^b-ΔH_f^c, and ΔS_f^b-ΔS_f^c plotted as a function of $N^{(-1/3)}$. The solid and long dashed lines show the fit of T and ΔH to a linear function of $N^{(-1/3)}$. Here we see an excellent fit for N above 736 atoms. The dotted line is the fit to Eq. 4-10, which should be valid above 736 atoms.

Table 4-1 Thermodynamic properties evaluated from the MD for various clusters as a function of size and the number of atoms within the cluster

Size	Cluster Radius[a] (Å)			Properties at Melt			Surface Energy (mJ/m^2)		
N	300K	Melting Point	1500K	T_m (K)	ΔH_f KJ/mol	ΔS_f J/mol.K	γ_{XV}-γ_{LV}[d]	γ_{XV}[b] (300K)	γ_{LV}[c] (1500K)
336	10.72	10.99	11.29	980	6.73	6.867	154	1812	1447
484	12.00	12.30	12.61	1060	7.98	7.528	169	1877	1475
736	13.60	14.03	14.32	1120	8.22	7.339	170	1926	1508
1004	14.97	15.22	15.71	1160	8.90	7.672	189	1990	1537
1956	18.41	19.01	19.28	1260	10.23	8.116	192	2034	1589
3997	23.04	23.90	24.16	1320	11.40	8.634	216	2088	1617
8007	28.70	30.07	30.17	1380	12.55	9.094	223	2146	1641
Extrap.[e]B.				1590	15.94	10.44			
Sim.B.				1760	17.30	9.830			
Exp.[f] B.				1728	17.64	10.2	354	2104	1750

[a] Derived as $R = \sqrt{(5/3)}\, R_g + R_{Ni}$

[b]Calculated as the total PE of the cluster minus the bulk PE for the same number of atoms divided by the area using the cluster radius (second column)

[c]Calculated as in b but using the PE of the supercooled liquid as the reference energy.

[d]Using Eq. 4-7.

[e]See Figure 4-2a.

[f] See Reference [4-6].

4.3.2 Surface melting and the Lindemann criterion

The concept of surface melting is that below the bulk T_m a quasi-liquid skin forms on the surface, which thickens as the temperature increases, leading finally to melting of the whole bulk solid. The bulk melting temperature is then the temperature at which the thickness of the "skin" diverges to infinity.

A useful way to relate the origins of melting to atomic phenomena is the Lindemann criterion [4-21], which states that melting occurs when the root-mean-square thermal displacement (RMSD) of the atoms in the lattice reaches a critical fraction (typically 10%~15%, depending on the crystal structure [4-22]) of the equilibrium interatomic distance. The atoms on the surface have weaker restraining forces than the bulk atoms (since they have fewer near neighbors), allowing them to fulfill this criterion at a lower temperature, suggesting a much lower T_{melt}.

To analyze the calculations in terms of such a model, we defined RMSD as in Eq. 4-3, and examined its dependence on the distance from the center of the cluster. Since the interatomic distance in pure Ni is about 2.49Å, we partitioned the atoms in the cluster with 1004 atoms (R=14.97Å) into 6 spherical bins, with dR = 2.5Å. The atoms were assigned to bins based on their average initial positions. The average RMSD was calculated for each spherical shell bin. Figure 4-3a shows the average RMSD as a function of distance from the center at various temperatures (for the N=1004 cluster). In all cases, the RMSD for the surface bin is larger than the central bins. Following the changes in RMSD through the melting process, we find a discontinuity of the RMSD for the central atoms, indicating a first order phase transformation (with latent heat). Figures 4-3b ~ 4-3d show snap shots of the cluster at 1000K, 1140K, and

1180K, providing a clear picture of the increased thickness of liquid skin formed on the surface at 1000K and 1140K and the melted bulk cluster at 1180K.

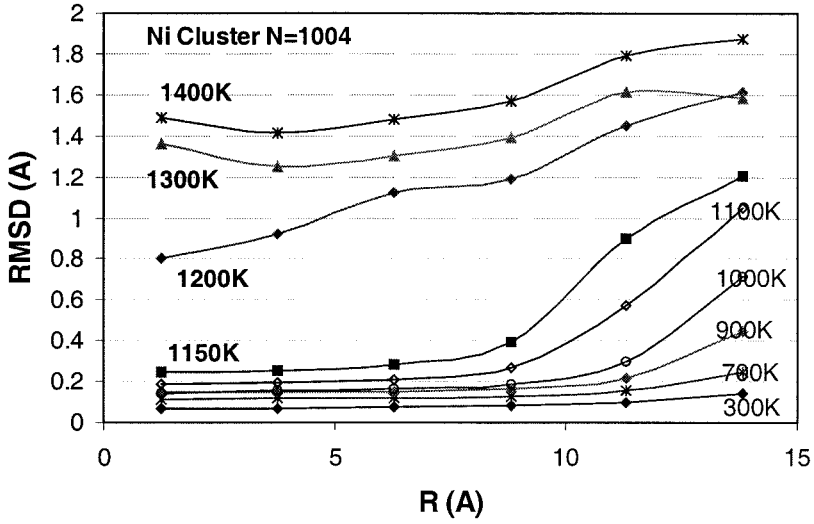

(a)

(b)T=1000K (c)T=1140k (d)T=1180K

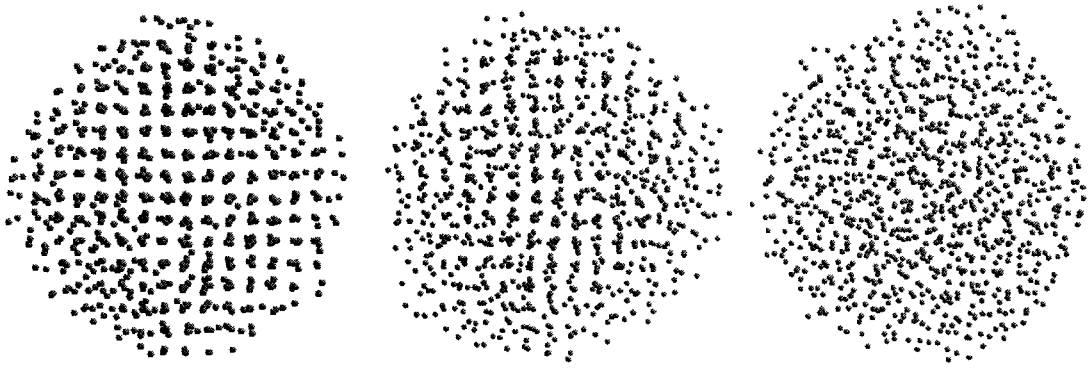

Figure 4-3a Average displacements for the atoms in various spherical shells, as a function of the distance from the center of the cluster. This shows surface melting starting at 1000K (using RMSD=0.6A as the criterion for melting), and the cluster has already melted by 1200K.

Figure 4-3b Snapshot of the 1004 Ni atom cluster at 1000K, showing formation of

the liquid "skin" at the outer layer.

Figure 4-3c Snapshot of 1004 Ni atoms cluster at 1140K, showing that the inner regions are still ordered.

Figure 4-3d Snapshot of 1004 Ni atoms cluster at 1180K, showing that the entire cluster is melted.

Defining the critical RMSD to be molten as 0.6Å (24% of the bulk interatomic distance of Ni), we find that at 1000K only the surface bin is molten. As the temperature rises to 1100K and 1150K the average RMSD for the atoms in the fifth and fourth bins, respectively, reach the critical RMSD, while the atoms in the central three bins remain crystalline. Finally, at 1200K (which clearly is above the melting temperature of the cluster) the RMSD for the whole cluster has exceeded RMSD of 0.6Å. Thus, using 0.6Å as the melting criterion, the radius of the remaining solid crystal region, $R_{crystal}$, can be calculated from RMSD, and the results are shown in Figure 4-4.

We can also estimate $R_{crystal}$ from the heat of fusion. The potential energy deviates from a linear function of temperature because of melting at the surface. We write this deviation as $\Delta PE = L^*N_L$, where L is the latent heat at T_m, and N_L is the number of atoms in the liquid phase. This leads to a radius for the remaining solid crystal of the form

$$R_{crystal} / R_{total} = (1 - \Delta PE / L)^{1/3} \qquad (4\text{-}11)$$

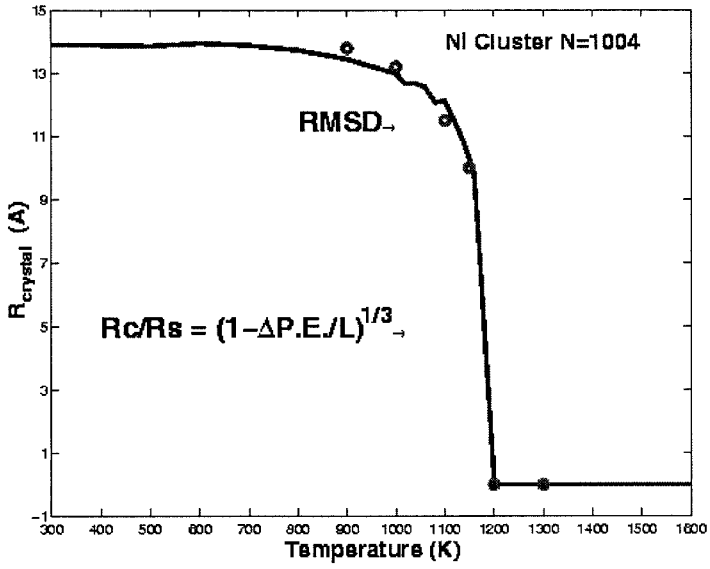

Figure 4-4 Radius of the remaining crystal in N=1004 cluster as a function of temperature, melting process, calculated from two methods: The circles indicate the values obtained from assuming a Lindemann criterion of RMSD > 0.6Å as an indication of melting. The line is based on Eq. 4-11 based on analyzing the dependence of Potential Energy temperature.

Indeed, Figure 4-4 shows that the radius of the remaining solid crystal from (4-11) leads to results very similar to the RMSD criteria when we use a melting criterion of 0.6Å (24% of the interatomic distance in Ni). This is much larger than the typical Lindemann criterion of 10-15%. This could be because these small clusters have a large fraction of the atoms on the surface (leading to a larger diffusion region for the surface atoms), or it could be that 24% is more accurate.

4.3.3 Size effects on cluster crystallization

Starting with the liquid phase and cooling at a fixed rate, all clusters initially display supercooling below T_{melt} and finally a large drop in the energy upon solidification. From the peak in the derivative of the energy (the specific heat), we can define the crystallization temperature, T_x.

Figure 4-5 shows the potential energies for the heating, cooling and reheating cycles of the 336 and 736 atom clusters. In both cases, after cooling to 300K, the potential energy approaches a value close to that in the heating process (which started with a cluster having the FCC structure). But after re-heating the 336 atoms cluster, the melting temperature increased to 1050K (The original FCC structure led to a melting temperature of 980K), which indicated quenching from melt has led to a phase more stable than FCC. This contrasts with the cluster with 736 atoms, which leads to the same melting temperature, 1120K, during re-heating.

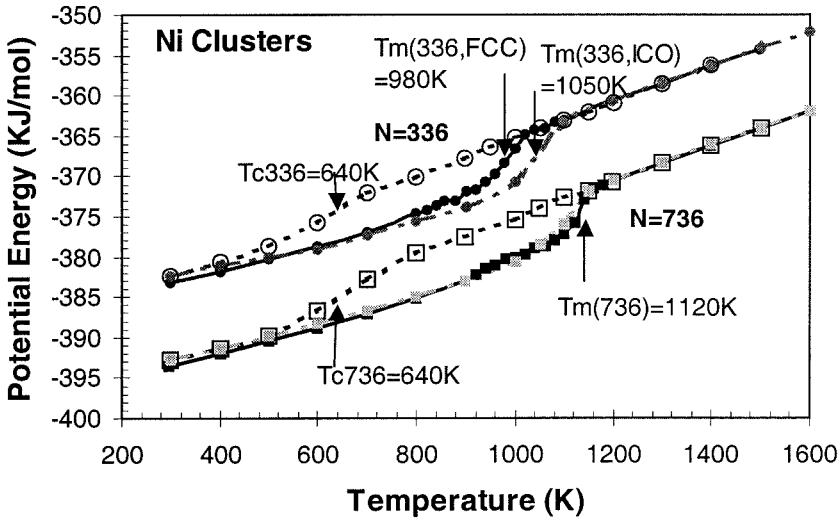

(a)

(b)N=736 (c)N=336

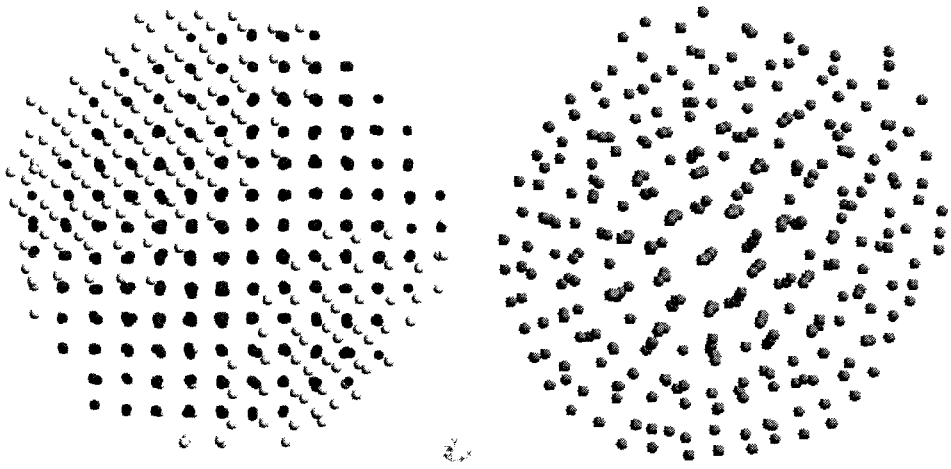

Figure 4-5a Potential energy U(T) as a function of heating from 300K (starting from an FCC strucure) to 1600K, cooling back to 300K, and then reheated to 1600K. For 336 atoms, the cluster after crystallization has an icosahedral structure, and the reheating shows that the icosahedral structure has a T_{melt} ~ 1050K, compared to 980K for the original FCC cluster. For the clusters with 736 atoms, the cluster after crystallization has a large region of FCC and the reheating leads to T_{melt} ~ 1120K, just as for the original heating.

Figure 4-5b [001] Projection of the new FCC crystal formed in the 736 Ni atoms cluster from heating and then cooling. Here the 494 dark balls form the new FCC crystal (orientation not related to the original crystal). The white balls are disordered atoms on surface.

Figure 4-5c Snapshot of solid cluster with 336 atoms at 300K. This is dominated by icosaheral character with five-fold symmetry.

Using the algorithm we developed for searching FCC grains, we found a perfect FCC crystal (Figure 4-5b) of about 500 atoms within the quenched 736-atom cluster. This FCC crystal had an orientation unrelated to the initial FCC structure, showing that memory or the original structure was lost. However, this new FCC structure still melts at 1120K. On the other hand, for the cluster with N=336 atoms we could not find in the quenched cluster any FCC cluster having more than 13 atoms. Indeed, the 336-atom cluster has a slightly deformed icosahedral structure, as shown in Figure 4-5c. This icosahedral structure is more stable than FCC by ~1 kJ/mol and melting temperature 70K (7%) higher than FCC. The N=336 cluster is very close to magic number of 309 atoms for a Mackay cluster with four shells, which could be the reason an icosahedral structure is more stable. For the similar reason, it could be that the N=736 atom cluster forms an FCC crystal easily because it is far from the nearby two magic numbers 561 and 923. Alternatively, icosahedral could be generally more favorable than FCC for sizes below 400 to 700.

4.3.4 Structural change in liquid quenching

To analyze the local ordering of the various clusters, we used the Honeycutt-Andersen (HA) algorithm [4-19] to characterize the environment for each pair of atoms. Table 4-2 shows the HA pair parameters for various structures (including FCC, HCP, and various icosahedral clusters) of Ni at 300K. We used the minimum between the first and second nearest neighbor distance in FCC crystal as the cutoff for bonded atoms, 2.99A for Ni, and 3.55 for AgCu. We see that 1551 and 2331 HA pair types are characteristic of icosahedral ordering. Here 1551 corresponds to two

neighbor atoms with five common neighbors forming a bonded pentagon, while 2331 corresponds to a pair of not bonded atoms that share three neighbor atoms forming a bonded triangle. Two other HA pair types, 1421 and 1422, characterize the FCC and HCP crystal structures. Normalizing by the total number of the first nearest neighbor pairs, the perfect FCC structure contains 100% of 1421 pairs but no pairs of 1551 or 2331 type.

Table 4-2 The analysis of various structures in terms of Honeycutt-Andersen (HA) pairs (based on the final structure at 300K)

Cluster	1201	1211	1301	1311	1321	1421	1422	1431	1541	1551	2101	2211	2321	2331	2441
FCC		0	0	0	0	1	0	0	0	0	1	2	0	0	0.5
HCP	0	0	0	0	0	0.5	0.5	0	0	0	1.5	1.5	0	0.17	0.5
ICO_13	0	0	0	0	0.71	0	0	0	0	0.29	0.14	0	0	0.71	0
ICO_55	0	0	0	0.26	0.26	0	0.38	0	0	0.1	0.97	0.64	0	0.38	0.26
ICO_147.	0	0	0	0.26	0.13	0.17	0.39	0	0	0.05	1.12	0.99	0	0.26	0.34
ICO_309.	0	0	0	0.23	0.08	0.31	0.35	0	0	0.03	1.15	1.2	0	0.19	0.39
C_336	0.03	0.01	0.02	0.22	0.06	0.33	0.27	0.02	0.02	0.02	1.15	1.23	0.04	0.18	0.35
H_336	0.03	0.08	0	0.17	0	0.72	0	0	0	0	0.8	1.63	0.06	0	0.37
ICO_561.	0	0	0	0.21	0.05	0.41	0.31	0	0	0.02	1.15	1.34	0	0.15	0.41
C_736	0.03	0.06	0	0.13	0.01	0.7	0.07	0	0	0	0.95	1.62	0.05	0.03	0.4
H_736	0.03	0.05	0	0.15	0	0.77	0	0	0	0	0.88	1.71	0.04	0	0.41

First we analyze the clusters with N=336 and N=736 atoms at 300K formed before and after the heating-cooling cycle. Comparing the solid-like cluster of N=336 atoms after quenching with the icosahedral cluster of 309 atoms, we see that they

have almost the same ratio of every pair parameter. This confirms that the cluster with 336 atoms has a high content of five-fold symmetry, which is compatible with an icosahedral structure (it definitely does not have FCC-like local order).

Figure 4-6 shows the HA analysis for types 2331, 1551 and 1421 for the clusters with 336 and 736 atoms during the heating-cooling cycle. Figure 4-6 also includes the analysis for the metallic glass formed in the AgCu system (studied in detail in reference [4-15]). In the initial FCC structure, there were no 2331 or 1551 pairs but 70% of 1421 pairs (less than 100% because of the atoms on surface.). As the temperature increases, the population of 1421 pairs decreases, dropping very quickly after surface melting begins and going close to zero after the cluster melts totally. Upon cooling AgCu, the 1421 pairs stay below 10% for the whole cooling process during which AgCu forms a metallic glass with T_g = 550K. Below 550K, the 2331 and 1551 pairs continue increasing with decreasing temperature, reaching values even larger than for the 55 atom icosahedral cluster (38% for 2331 pair and 10% for 1551 pair), but less than the 13 atom icosahedral cluster (71% for 2331 pair and 29% for 1551 pair). This indicates that the metallic glass has a great deal of icosahedral local structure.

For the 736-atom cluster the cooling process recovers 70% of the 1421 pairs after the new FCC crystal is formed. However, the 336 atoms cluster reaches only 33% of the number 1421 pairs characteristic of FCC (close to the ratio of 1421 pairs in the 309 icosahedral cluster). The 2331 and 1551 pairs show quite interesting properties during the phase transition. During the heating process the fraction of both kinds of pairs increases at first and then drops upon melting of the whole structure. In the

cooling process, the undercooled liquid shows an increasing fraction of 2331 and 1551 pairs (observed also in a Lennard-Jones system [4-19]) until crystallization. For the N=736 atom cluster, we find that below the crystallization temperature of 600K the amount of 2331 drops to 3% and the 1551 pairs drop to zero. However, for the 336 atom cluster, 2331 only drops to 18% while 1551 drops only to 2% (both close to the values of 19% 2331 pairs and 2% 1551 pairs in the icosahedral cluster with N=309 atoms).

(a) 1421 HA pairs showing FCC character

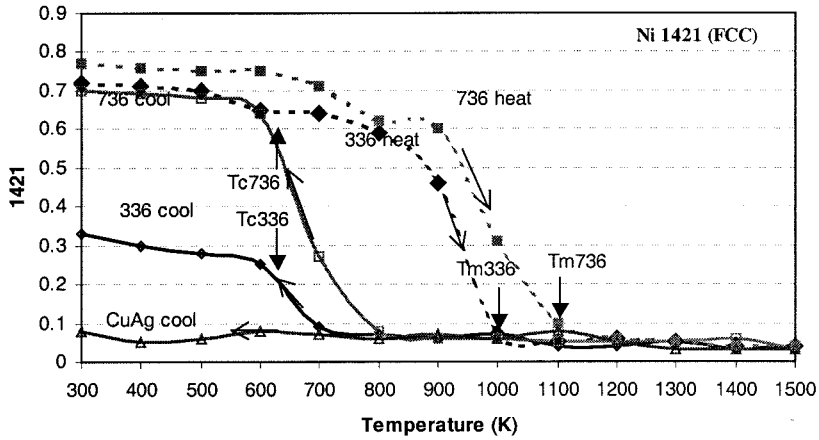

(b) 2331 HA pairs showing icosadedral character

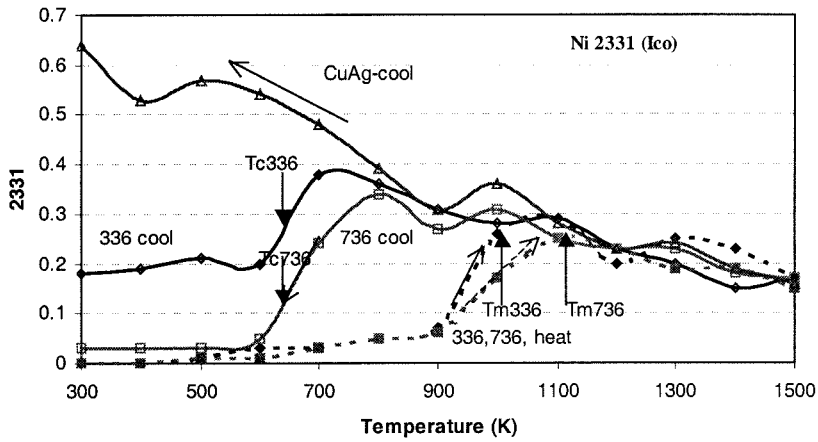

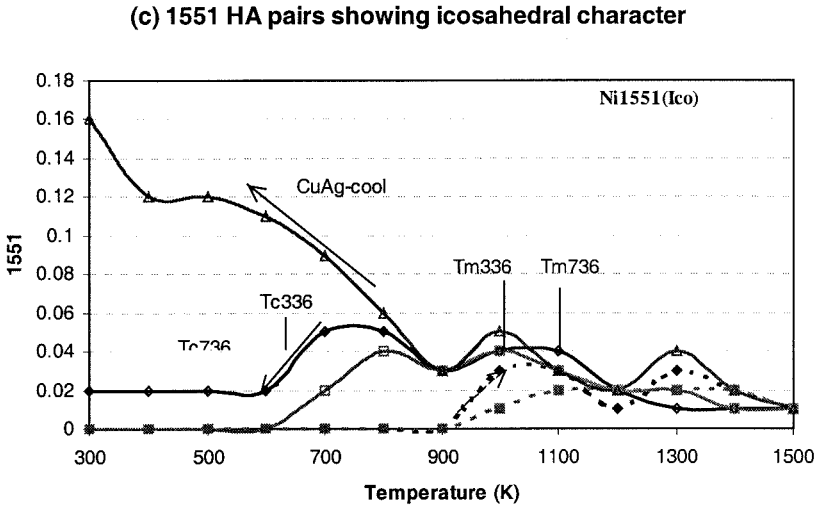

Figure 4-5 Honeycutt-Andersen pair populations as a function of T. Shown are the 336 and 736 atom clusters, and the bulk CuAg system (which forms a glass upon cooling to 550K).

4.4 From molecular regime to mesoscale regime

We find that for Ni the thermodynamic properties relevant to melting and surfaces behave in a very regular way for clusters above 736 atoms, with the difference between the enthalpy and melting temperature for the clusters deviating from the bulk value by an amount proportional to $N^{-1/3}$ as expected from the ratio of surface atoms to bulk atoms. We refer to this as the *mesoscale regime*. However, below ~500 atoms there are significant deviations from the trends observed in the mesoscale regime. We find that these deviations in the small cluster (molecular) regime are caused by a transition of the cluster to a structure different than for the bulk and

mesoscale system. For Ni, the small clusters prefer a structure with significant icosahedral structure. For very small clusters (147 and 70 atoms), the icosahedral structure is obtained by annealing at moderate temperatures. For larger structures, it was necessary to melt the initial FCC structures in order to transform to the more stable icosahedral form. In either case the structure stabilized for small clusters leads to significant deviations from the thermodynamic properties extrapolated from the mesoscale regime. We will discuss below first the mesoscale regime and then the small cluster regime.

4.4.1 Mesoscale regime

Due to the large ratio of surface to bulk atoms, the melting of mesoscale clusters differs from the bulk system in three main respects [4-1],[4-7]~[4-13],[4-22]~[4-30].

4.4.1.A Decrease of melting point with decreasing particle size

The decrease of the melting point with particle size has been observed in experiments on supported clusters of Au [4-1], Sn [4-7], Pb [4-9], and Pt [4-10], for isolated Sn particles (with 500 atoms [4-8]), and for gas phase Na particles (with only 139 atoms [4-11]). It has also been verified in many simulations [4-24]~[4-30]. We find that the change in (T_m^b - T_m^c) with size is quite proportional to $N^{-1/3}$ for clusters with N above 736 atoms, which prefer the FCC structure.

4.4.1.B Latent heat of fusion

The decrease of the latent heat of fusion with size has been observed by calorimetric measurements on small Sn particles [4-7][4-8] and by numerical simulations [4-28]. As shown in Figure 4-2b, we find that the decrease scales as $N^{-1/3}$

for clusters larger than 500 atoms

We observed that for clusters with ~100 atoms, the FCC cluster transforms during heating to a lower energy icosahedral structure. This icosahedral cluster then melts at higher temperature and with a larger heat of fusion than the FCC cluster. A similar increased latent heat is exhibited for isolated tin clusters with about 500 atoms. It is not clear in our simulations that such a transition occurs for clusters with 484 and 363 atoms, but they might favor icosahedral structure leading to a higher heat of fusion, and a smaller ΔH_f^b-ΔH_f^c, as found in Figure 4-2b.

4.4.1.C Critical size for zero latent heat of fusion

When the latent heat drops to zero, the cluster fluctuates between solid and liquid, leading to a phase transition that spreads over a finite temperature range. This results because of (i) formation of a size dependent liquid skin, and (ii) thermodynamic fluctuations, which become significant in small systems. We find that this skin grows with temperature. Based on the linear fit to the mesoscale FCC regime, we estimate that heat of fusion would go to zero for clusters of ~ 86 atoms, leading to a melting temperature of 633K. According to Turnbull's glass forming ability criteria, a good glass former will have a ratio of glass transition temperature (Tg) to the melting point (Tm) increased from values near 1/2 to 2/3, such that the homogeneous nucleation of crystals in the undercooled melt should become very sluggish. It's believed that Tg for pure metal is about ¼ of Tm; in Ni system it should be around 400K [4-38]. For bulk Ni, small Tg to Tm ratio makes it very difficult to form a bulk amorphous phase of Ni. However, if the melting temperature can be decreased to ~ 600K, we expect

that it would be easy to form glassy Ni.

For Ni clusters we did not find a clear formation of the amorphous phase, because FCC is not the stable structure for Ni clusters smaller than 500. Since the small FCC clusters (up to 147 atoms) transform into the icosahedral phase during heating, we obtain a larger melting temperature and latent heat for melting of the icosahedral phase. Thus the size for which the heat of fusion becomes zero for the icosahecral phase is likely much smaller than 86 atoms.

4.4.1.D Surface melting

The role of surface melting in nanoclusters has also been studied for Pb particles on a Si substrate [4-9]. These studies show that a ~0.5nm liquid skin grows just below the melting temperature of a 50nm Pb crystal, indicating size dependent melting. These results are consistent with our simulations.

The driving force for melting on a flat surface is the reduction in the total interfacial energy [4-6][4-29],

$$\Delta\gamma = \gamma_{XV} - (\gamma_{LV} + \gamma_{XL}) > 0 \qquad (4\text{-}12)$$

where γ is the surface energy between the solid (X), liquid (L), and vapor (V) phases. For Ni, the experimental driving force $\Delta\gamma$ is close to zero [4-6] so that a surface melting on a flat surface is not expected. However, in our simulation the surface energy are decreasing with the radius of the particles, and since geometrical and capillary effects, might increase the thickness of quasi-liquid skin in small particles [4-32], and decrease the interface energy of solid and quasi-liquid. As a result the small radius of these small clusters could favor surface melting, as we seen in this

study.

4.4.2 Small cluster (molecular) regime

Surfaces are expected to play an especially important role in crystallization processes, where optimizing the internal packing and minimizing surface energy are competitive driving forces. Thus, to understand the crystallization of a free nanocluster, we must understand homogeneous nucleation. Below some critical radius (~10-20Å) the optimum structure might change from the bulk-like structure (say, FCC) optimal for long range order to a new arrangement optimum for a cluster environment [4-33][4-34].

4.4.2.A Comparison with previous simulations

As shown in Figure 4-5a, for 336 atoms the icosahedral structure of Ni melts at a temperature 70K (7%) *higher* than the FCC structure. As a result, the $N^{-1/3}$ rule does not apply at these small sizes. We also found that for very small clusters, such as N=140, N=87, the FCC structure transforms to icosahedral *before* melting, which also leads to a higher melting temperature than the Tm predicted from of the extrapolation of the $N^{-1/3}$ rule. Since these icosahedral structures are formed during natural quenching or even heating processes, they are more stable than FCC. It is reasonable to propose that below a critical size, ~ 500 atoms in our study, the icosahedral phase actually is the stable phase favored by the small clusters. Thus these clusters will have a melting temperature higher than predicted by the $N^{-1/3}$ extrapolation from FCC particles. This leads to melting temperature below the critical size that may depend on size differently than $N^{-1/3}$.

Similarly, particles of Ag [4-35] are observed experimentally to prefer an icosahedral arrangement below a critical size cluster. Indeed, for Lennard-Jones gases numerous simulations have confirmed the stability of icosahedral arrangements (Mackay [4-36]), with particular stability for the magic number clusters [4-37] (containing 13, 55, 147, 309, 561, 923, 1415, and 2057 atoms).

Cleveland and Landman reported in detailed studies of the size dependence of energetic and structure of small nickel clusters [4-31], where they found icosahedral clusters to be favored for clusters smaller than 2300 atoms (EAM force field) and 1600 atoms (LJ force field). Since only the minimized energy was considered, the critical sizes are for 0K. We quenched from a liquid drop and also observed the formation of icosahedral clusters. However, we find that for our FF at 300K and a cooling rate of 4K/ps, the critical size for forming icosahedral is ~ 500.

4.4.2.B Compared with Bachels model

Bachels *et al.* have combined their measurement of melting temperature on isolated tin nanoparticles [4-8] with experiments on supported tin particles by Lai [4-7] to propose a model, in which below a critical radius (35Å), the melting temperature of the particle lies below the surface melting temperature, such that the surface pre-melting effect will be suppressed, leading to a constant melting temperature [4-8]. But there is still a large difference between their predictions and the experimental data on melting temperature for a cluster with 500 atoms, and they suggested that the difference is due to insufficient accuracy of the parameters used for evaluating their model.

However, we noticed that the actual melting temperature of tin particle with ~500 atoms is *larger* than that predicted from size dependence rule ($N^{-1/3}$) based on nano particles ranging from 5~50nm. This agrees with our finding that the critical size should be related to the icosahedral phase (or other stable structure) for small particles. It is very likely that the initial solid state cluster structure in the experiments with ~500 atoms were already in the icosahedral structure, hence it is expected that the melting temperature will be higher than the value predicted by the extrapolation from the larger nanoparticles of size 5~50nm (FCC).

4.4.2.C Simulations on Au particles

From simulations Cleveland *et al.* [4-30] showed that clusters smaller than 500 atoms lead to properties very different than larger particles. They studied gold clusters with 75, 146 and 459 atoms and found a solid (truncated-decahedra for Au75 and Au146, and FCC with truncated-octahedral for Au459)-to-icosahedral transformation. They didn't find that a quasi-liquid wetting layer formed on the surface, which thickens until the whole cluster melts in clusters Au75 and Au146, but there is solid-liquid coexistence in Au459. They calculated the melting temperature decreases with size (T_{melt} ~550K for N=75, T_{melt} ~625K for N=146, and T_{melt} ~760K for N=459), all below that for bulk system (T_{melt}=1090K). However, they did not report results for larger clusters, where the size dependence of melting temperature might be described by the $N^{-1/3}$ rule. Based on our results, we expect that the melting temperatures for these cases are higher than the melting temperature of FCC structures having the same sizes.

4.5. Conclusion

Using MD simulations with the QMSC FF on unsupported Ni nanoclusters, we find that for the mesoscale regime above ~750 atoms, the melting temperature and heat of melting scales inversely as $N^{1/3}$ for FCC structures. We find that melting proceeds from the surface inwards and that the melting process for the central core is discontinuous (first order). Thus the mesoscale regime is characterized by surface melting.

Upon quenching from the melt, we find that larger clusters and bulk Ni crystallize easily to form FCC crystals. However, for smaller clusters, with less than ~ 500 atoms, we find that the stable structure is icosahedral, which has a higher melting temperature and larger heat of fusion than FCC structures to the same size.

We also found that the supercooled liquid and glassy phase are highly icosahedral as is the pre-melted phase.

References:

[4-1] P. Buffat and J-P Borel, Phys. Rev A **13**, 2287 (1976)

[4-2] S. Sugano, Y. Nishina and S. Ohnishi, Microclusters: Proceedings of the First NEC Symposium, Springer Verlag, New York, (1987)

[4-3] H. Haberland, Clusters of Atoms and Molecules I: Theory, Experiment, and Clusters of Atoms, Springer Verlag: New York, 1995

[4-4] T. P. Martin, Clusters of Atoms and Molecules and Molecules, Kluwer Academic, Boston, (1995)

[4-5] P. Jena, S. N. Khanna and B. K. Rao, Proceedings of the Science and Technology of Atomically Engineered Materials, World Scientific, New Jersey, (1995)

[4-6] R. Canselow and R. F. Howe, Chemistry and Physics of Solid Surfaces VII, Springer, Heidelberg, (1988)

[4-7] S. L. Lai, J. Y. Guo, V. Petrova, G. Ramanath and L. H. Allen, Phys. Rev. Lett. **77**, 99 (1996)

[4-8] T. Bachels and H.J. Guntherodt, Phys. Rev. Lett. **85**,1250 (2000)

[4-9] K. F. Peters, J. B. Cohen, and Y-W. Chung, Phys. Rev. B **57**, 13430 (1998)

[4-10] Z. L. Wang, J. M. Petroski, T. C. Green and M. A. El-Sayed, J. Phys. Chem. B **102**, 6145 (1998)

[4-11] M. Schmidt, R. Kusche, E. Kronmuller, B. V. Issendorff and H. Haberland, Phys. Rev. Lett. **79**, 99 (1997)

[4-12] S. K. Nayak, S. N. Khanna, B. K. Rao and P. Jena, J. Phys.: condens. Matter **10**, 10853 (1998)

[4-13] Z. B. Guvenc and J. Jellinek, Z. Phys. D **26**, 304 (1993)

[4-14] T. Cagin, Y. Qi, H. Li, Y. Kimura, H. Ikeda, W. L. Johnson and W. A. Goddard III, MRS Symp. Ser. **554**, 43 (1999). Also A. P. Sutton and J. Chen, Phil. Mag. Lett. **61**, 139 (1990)

[4-15] Y. Qi, T. Cagin, Y. Kimura and W. A. Goddard III, Phys. Rev. B **59**, 3527 (1999)

[4-16] H. Ikeda, Y. Qi, T. Cagin, K. Samwer, W.L. Johnson and W. A. Goddard III, Phys. Rev. Lett. **82**, 2900 (1999). Also Y. Qi, H. Ikeda, T. Cagin, K. Samwer, W.

L. Johnson and W. A. Goddard III, Materials Research Society Symposium Proceedings Vol. 554,. 367(1998).

[4-17] J. R. Ray and A. Rahman, J. Chem. Phys. **82**, 4243 (1985); W. G. Hoover, Phys. Rev. A **31**, 1695 (1985); M. Parrinello and A. Rahman, Phys. Rev. Lett. **45**, 1196 (1980)

[4-18] Y. Qi, T. Cagin, and W. A. Goddard III, Computer Aided Materials Design, submitted

[4-19] J. D. Honeycutt and H. C. Andersen, J. Phys. Chem. **91**, 4950 (1987); also H. Jonsson and H. C. Andersen, Phys. Rev. Lett. **60**, 2295 (1988)

[4-20] S. Valkealaht and M. Manninen, Comp. Matter. Sci. **1**, 123 (1993)

[4-21] F. A. Lindemann, Z. Phys. **14**, 609 (1910)

[4-22] S.-A. Cho, J. of. Phys. F Metal Physics **12**, 1069 (1982)

[4-23] P. Melinon, C. Paillard, V. Dupuis, A. Perez, P. Jensen, A. Hoareau, J.P. Perez, J. Tuaillon, M. Broyer, J. L. Vialle, M. Pellarin, B. Baguenard, and J. Lerme, Int. J. Mod. Phys. B **9**, 339 (1995)

[4-24] P. Labastie and R. L. Whetten, Phys. Rev. Lett. **65**, 1567 (1990)

[4-25] X. Yu and P. M. Duxbury, Phys. Rev. B **52**, 2102 (1995)

[4-26] J. B. Mallet, A. Boutin and A. H. Fuchs, Phys. Rev. Lett. **76**, 4336 (1996)

[4-27] L. J. Lewis, P. Jensen and J-L. Barrat, Phys. Rev. B **56**, 2248 (1997)

[4-28] F. Ercolessi, W. Andreoni and E. Tosatti, Phys. Rev. Lett. **66**, 911 (1991)

[4-29] J. G. Dash, Contemp. Phys. **30**, 89 (1989)

[4-30] C. L. Cleveland, W. D. Luedtke and U. Landman, Phy. Rev. B **60**, 5065 (1999)

[4-31] C. L. Cleveland and U. Landman, J. Chem. Phys. **94**, 7376 (1991)

[4-32] M. B. Baker and J. G. Dash, J. Cryst. Growth **97**, 770 (1989)

[4-33] S. Ino, J. Phys. Soc. Jpn. **27**, 941 (1969)

[4-34] For instance, B. Raoult, J. Farges, M. F. De Feraudy and G. Torchet, Philos. Mag. B **60**, 881 (1989) and references therein

[4-35] B. D. Hall, M. Flueli, R. Monot and J.-P. Borel, Phys. Rev. B **43**, 3906 (1991)

[4-36] A. L. Mackay, Acta Cryst. **15**, 916 (1962)

[4-37] R. F. K. Herzog, W. P. Poschenrieder and F. F. Satkiewicz, Radiat. Effects **18**, 199 (1973)

[4-38] D. Turnbull and J. C. Fisher, J. Chem. Phys. **17**, 71 (1949); also D. Turnbull, J. Chem. Phys. **18**, 198 (1950)

Chapter 5 Deformation Behavior of FCC Metallic Nanowires Under High Strain Rates

5.1 Introduction

From mechanical tests and structure analyses, such deformation mechanisms as dislocations [5-1][5-2], twinning [5-3][5-4], and grain boundary sliding [5-5] have been proposed and verified in various systems. The two major and competitive deformation models in single crystal are slip and twinning. Deformation twins are more prominent in lower symmetry crystal structures such as BCC and HCP than in FCC, because the potential active slip systems are reduced. Increasing in strain rate or decreasing in temperature tends to favor twining over slip, since both parameters suppress the thermally-activated dislocation processes, such that stresses can be high enough to nucleate and grow deformation twins. Indeed twins have been observed in FCC metals exposed to large strain rates (such as in shock load/impact conditions [5-6]), and/or low temperature [5-7]. Unfortunately, experiments under these conditions tend to have many factors all playing roles simultaneously. For instance, experiments at very high strain rates lead to shear localization arising from adiabatic heat dissipation and localized thermal softening. On the other hand, molecular dynamics (MD) simulations can isolate the direct effect of strain at various strain rates from those due to heat dissipation and the concomitant temperature increase by controlling the temperature and the stain rate. Keeping the temperature constant can then be used to analyze the detailed mechanisms of the deformations.

To model solid state deformation, Parrinello and Rahman have proposed constant stress dynamics [5-8], with the shape matrix, $\boldsymbol{h}$, which characterize the shape and size of the simulation cell, can adjust to the applied external stress. They have used this method to study the FCC to HCP phase transformation under uniaxial compression and elastic limit under tension of bulk Ni, which interaction is represented by two-body Morse potential [5-9]. In PR's method, a parameter called "piston mass," W, is introduced with the variable $\boldsymbol{h}$ matrix. Even though the equilibrium average properties are independent of W, it determines the relaxation time for the recovery from and imbalance caused by external pressure and the internal stress, such that one needs to choose W carefully when studying the states beyond elastic limits. PR's method is used to systems with periodic boundary condition, but when there is a free surface, the definition of volume can't be described by $\boldsymbol{h}$ matrix any more.

To overcome these two difficulties, we used a quasi-static equilibrium MD approach to simulate constant strain rate uniaxial tensile process in nanowires [5-10], where we found strain rate induced amorphization beyond a critical strain rate ($5\%ps^{-1}$ in Ni) and below this critical high strain rate, the crystal is very ductile, with deformation twin formation and coherent shearing events. Generally the strategy for forming amorphous metals involves alloying with elements that are dissimilar in size and bonding (chemical disorder) or by introducing various defects [5-11] followed by sufficiently rapid decreases in the temperature that there is no time for crystal nuclei to form. In contrast we found that a homogenous perfect crystal at constant temperature can be transformed continuously to an amorphous metal by application of sufficiently large strain rates. Thus there are now three orthogonal processes for

forming amorphous metals: rapid quenching from a liquid, introduction of chemical or physical disorder, and application of rapid strain rates.

Branicio and Rino studied the same process in Ni nanowire with different cross sections [5-12] and found Young modulus dependence of cross section, but the deformation processes are the same in systems with different cross sections. The yielding stress is slightly different since they used embedded-atom method for Ni [5-13] and we used Sutton-Chen type of potential modified by some quantum effects [5-14].

In this chapter we will focus on the deformation behavior of NiCu under high strain rates, compared with the Ni and NiAu alloy. And this chapter is organized as follows. Some details of the quasi-static equilibrium MD approach of strain rate simulation are discussed in section 5.2. From section 5.3 to 5.8 we discuss the deformation behavior, including the evidence of deformation twinning associated with the sharp stress drop, the new mechanism of deformation under high strain rate, the strain rate induced amorphization and the relation between glass formability and the critical strain rate required to form glass.

5.2 Simulation methods

5.2.1 MD procedures of constant strain rate simulation

The periodic unit cell for the MD simulations consisted of 5*5*10 fcc cubic cells (For example: 1.78nm*1.78nm*3.56nm for NiCu) with 1000 atoms. We started with an FCC single crystal and equilibrated at 300K for 100ps to reach an equilibrium state. For the alloys NiCu (50%) and NiAu (50%) we assumed a random FCC

structure. We used 1-D periodic boundary condition along the <001> (z) crystallographic direction to simulate an infinite long nanowire with finite width (initially about 2nm thick) and free surfaces in the x and y directions.

A tensile strain, ε_{33}, was applied in the z direction to these nanowires. To maintain the specified strain rate, the tensile strain along the <001> direction was increased by 0.5% at a time interval determined by the strain rate (For example 1ps for 0.5%/ps). At each strain state, (which is increasing) we used constant volume and constant temperature (ThN) [4-17] dynamics to relax the system. And the simulation time at each strain state is determined by strain rate. To avoid the generation of stress wave, the strain was applied uniformly to all layers of atoms, which were then allowed to relax in the MD. The temperature is controlled by Hoover constant temperature method [5-16], which isolates effects of adiabatic heat dissipation and thermal softening. The stepwise strain increasing method provides a relaxation time for all the atoms at each strain state, the longer the simulation time at each strain state, the more equilibrium the tensile process is close to. This is different with PR's constant stress method, where the shape matrix, ***h,*** will respond to the applied stress at every step, so the detailed relaxation of atoms can't occur and the failure of system is prevented by uniform elongation tendency.

At each strain state, we evaluate the average energy, stress, pair distribution function for the whole simulation, and the elastic constants from the final snapshot structure (only Born term contribution, [5-17] since the temperature is kept constant, the thermal fluctuation term is ignored). Even though for some fast strain rate, the

simulation time of 100 steps is not enough to reach equilibrium, the overall trend of these properties are reliable for the study of rate dependence.

5.2.2 Correction of the results from ThN MD

The constant volume in ThN dynamics means that the shape and size of the simulation cell is unchanged. However, due to the free x-y surface, the "Poisson's ratio" causes the contraction on x-y direction when the sample is under tension, such that the volume of the unit-cell (the volume used in MD calculation) is not the actual volume of the sample any more. To get the correct stress and elastic constants, we have to use the true sample volume and correct the calculated intensive variables. In the true volume calculation, each atom is replaced by a sphere with atomic radii; the simulation cell space is then divided into 100*100*200 small grids, which length is about 0.2Å. If a grid is occupied by the sphere or it's an interstitial among spheres, the volume of this grid will be counted. At the end the total occupied grid volume is the approximation of the true volume of the sample. This method allows us to estimate the actual volume of an arbitrary shape without a big hole inside. The correction to the stress is therefore

$$\sigma_{ij} = \sigma'_{ij} V_{cell} / V_{true} \tag{5-1}$$

and the correction to elastic constant is

$$C_{ijkl} = C'_{ijkl} V_{cell} / V_{true} \tag{5-2}$$

where Vtrue is the actual volume of the system, and Vcell is the volume of the simulation cell (which is kept constant at each strain state, and increasing along z direction during tensile test), σ_{ij} and C_{ijkl} are the correct stress and elastic constant

tensors, and σ'_{ij} and C'_{ijkl} are the stress and elastic constant calculated using the volume of simulation cell in dynamics.

We noticed that at zero strain state, σ_{33} is not zero, after the sample is relaxated at 300K. Using the coordinates in the unstressed wire leads to initial stress components of σ_{33} = 1.9 GPa, σ_{11} = -0.1 GPa, and σ_{22} = -0.1 GPa. This arises from the capillary forces associated with the free surfaces.

$$F_z = \frac{\partial E_s}{\partial L} = \frac{\partial}{\partial L}\left(4\gamma L\sqrt{\frac{V_0}{L}}\right) \tag{5-3}$$

The stress component along z direction due to the capillary force is therefore

$$\sigma_{33}^{cap} = \frac{F_z}{V_o / L} = \left(\frac{2\gamma}{\sqrt{V_0}}\right)L^{1/2} = \left(\frac{2\gamma}{\sqrt{V_0}}\right)\sqrt{L_0(1+\varepsilon)} \tag{5-4}$$

where, γ is surface energy, V_0 is the true volume, which we assume is unchanged, and L and L_0 are the length along z direction during tension and length at initial state. According to equation 5-4, the stress at zero strain state, leads to a surface energy γ =1 J/m^2, which is comparable to experimental values for Ni, Cu [5-18]. This simple strain dependence of capillary force is only valid when the sample is uniformly deformed or before necking occurs.

Equation 5-4 also shows that the stress due to the capillary force is a function of the strain, such that we should correct the stress by the new capillary force as well.

$$\sigma''_{33}(\varepsilon) = \sigma_{33}(\varepsilon) - \sigma_{33}(0)\sqrt{(1+\varepsilon)} \approx \sigma_{33}(\varepsilon) - \sigma_{33}(0) \tag{5-5}$$

where, σ_{33} is the tension stress along z direction after volume correction, and σ''_{33} is the stress after the capillary force correction. The strain rate dependence part of

capillary force correction is small when strain is relatively low; such that the reported stress in the following discussion is first corrected by the true volume of the deformed sample then taken as the net difference between the strained state and the zero strain state.

5.3 Deformation behavior

We summarize the strain rate dependent deformation behaviors of NiCu crystal at 300K in Figure 5-1 and Figure 5-2. Figure 5-1 displays the stress (σ_{33}) vs. strain (ε_{33}) curve for NiCu at T=300K for each strain rate. The stress-strain relation is linear at small strain, and the yield stresses (strain) increase from 4.3Gpa(7%) at strain rates of 0.05%/ps to 5 9.6Gpa(15%) at strain rate of 5%/ps. The increase of yield stress and strain increases with the strain rate is called strain-rate hardening. This occurs because when the relaxation of the system cannot keep up with the fast strain rate, causing the yielding process (twinning or amorphization) to get delayed. Due to the lack of defects and fast strain rate, the elastic yield stresses and strain in these cases far exceed that of bulk NiCu.

At low strain rates, 0.05%/ps and 0.5%/ps and 1%/ps, the stress drops in a repeating loading/plastic flow cycle after passing the elastic limit. From analyzing the structures, we have been able to identify these events as coherent shearing, and the twinning formed during the shearing events. The stress drop is caused by twin deformation, which is also observed in experiments [5-19]. During the next increase of the stress, the Young's Modulus remains almost the same. Multiple coherent shearing continue to take place as tensile stress increases, but eventually necking

begins around 80% strain for strain rates of 0.5%/ps and 1%/ps, and sample becomes disordered around the necking part, due to the local high stress. Eventually the stress concentration at the neck causes failure, with the stress dropping to zero. After fracture additional increments in strain cannot cause any increase in stress; however the melted neck relaxes back to FCC crystalline packing in the absence of the stress field.

But when the strain rate is increased to 5%/ps we see quite different behavior. At 5%/ps strain rate, no coherent shear bands and twins are formed within the specimen. Instead, the specimen transforms continuously from an FCC crystal to a glass with accompanying homogeneous plastic flow. Stress-strain curve showed a gradual rounding without "twinning related" stress dropping/increasing events, and after further plastic deformation, the stress decreased but converged to a value around 3.6Gpa and a calculated viscosity ($\eta = \sigma_{33} / \dot{\varepsilon}$) of 0.072 Poise for this steady flow. We reported this strain rate induced amorphization by analyzing the radial distribution function and elastic constants in an early work [5-10]. It should be pointed out that the volume correction for stress is important, without the volume correction, the breaking stress does not drop to zero and the steady flow does not converge but keep dropping.

Figure 5-2 shows snapshots at 100% strain for different strain rates. We can see that both the samples in (a) and (b) (at strain rates of 0.5%/ps and 1%/ps respectively)showed a multi-crystalline structure, with a disordered necking region. In structure (d), the whole systems transformed into a disordered structure under strain rate of 5%/ps, and even at such high strain rate, the sample is homogeneous

with a normal Poisson contraction in the ε_{11} and ε_{22} strains and no necking has been observed at this stage. Sample (c) has combined characters of structure (b) and (c), coexisting of some orientated structure and large disordered region; it shows a less obvious necking than (a) and (b), but not uniformly stretched structure as (d) either.

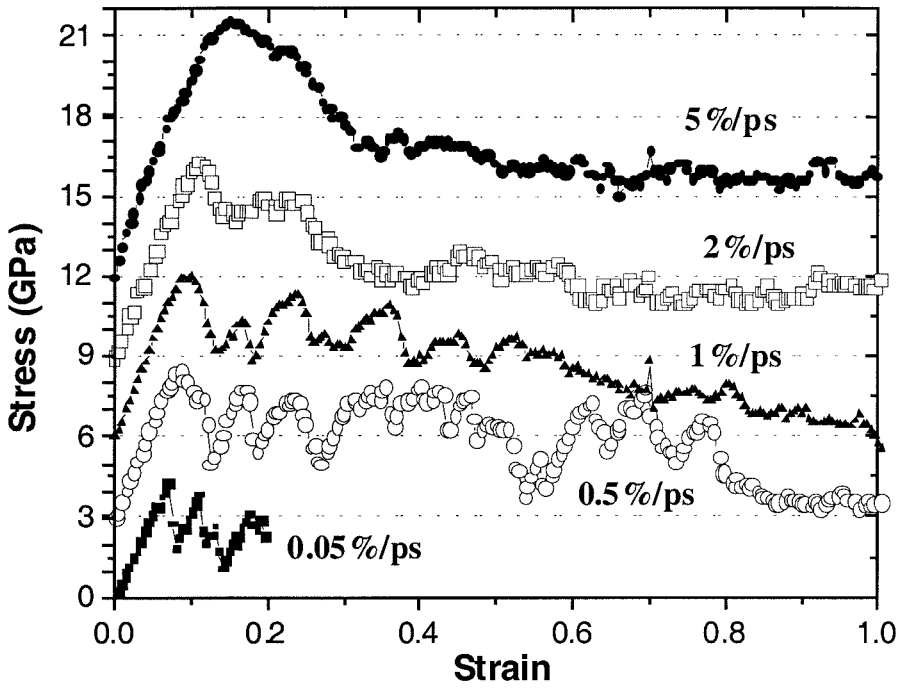

Figure 5-1 Stress-Strain curves for strain rates of 0.05%/ps to 5%/ps starting with CuNi alloy with random FCC crystal structure at 300K. All these strain rates show elastic behavior up to ~7% strain. For 0.05%/ps, 0.5%/ps and 1%/ps, the stress is relaxed by twin formation, which subsequently hardens the material, leading to a zigzag stress-strain curve. For 2%/ps and 5%/ps strain rates, there is a continuous transformation to amorphous phase of NiCu.

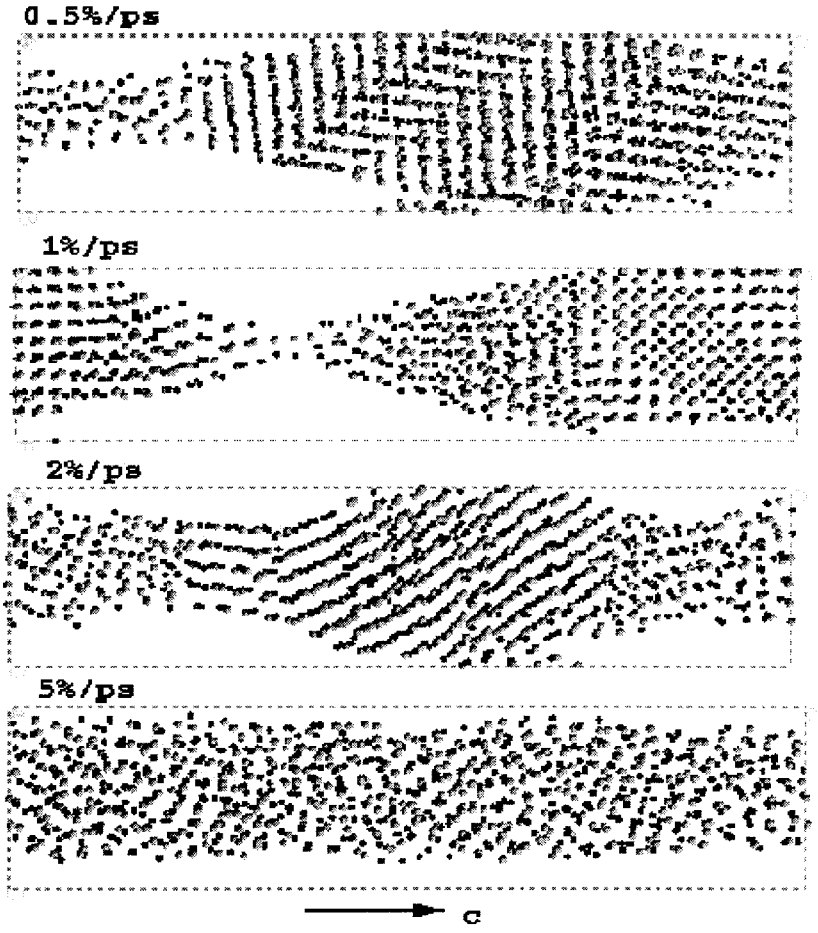

Figure 5-2 Snapshots of an FCC NiCu alloy nanowire at 100% strain, deformed at uniform strain rates starting with the random FCC single crystal at 300K.

a. 0.5%/ps shows twining, necking and local melting

b. 1%/ps shows finer FCC grains and necking

c. 2%/ps shows extensive disordering

d. 5%/ps shows FCC crystalline fully amorphized

5.4 Twin formation

To study the structural details, we show the $(01\bar{1})$ projection of the structure before and after yielding at strain rate of 0.05%/ps and 0.5%/ps in Figure 5-3(II), and corresponding stress-strain curve in Figure5-3 (I). We highlight a group of neighbor atoms on (111) and $(\bar{1}11)$ planes, and keep track of them during the deformation. Structure (a) is at elastic yielding point 7% strain, under 0.05%/ps strain rate, where no plastic deformation has taken place. After the first load drop under strain rate of 0.05%/ps, the mismatch on (111) planes are obvious in structure (b), which is at 8% strain. There are two twins formed; one with two $(\bar{1}11)$ layers of atoms, and one only has one (111) layer of atoms. These twins are formed through cooperative shearing. To return back to the original crystal orientation due to the applied periodicity along z direction, two twins must be formed on different (111) planes. The relative displacements for the atoms across the twin boundary are along $<\bar{2}11>$ on (111) planes, consistent with the well known (111)[112] twin system in FCC metals. The same mirror image of twin pattern can be seen from Figure 5-3(III), which is the schematic of twinning in FCC metals, and the projection from (220) plane is included to keep the same view as the snapshots shown in Figure 5-3 (II). At a strain state of 14%, (under strain rate of 0.05%/ps) after the second stress drop finishes, there are still two twins in the sample, while both twins increased by one more layer. Structure (d) is after the first load drop under the strain rate of 0.5%/ps, where two twins formed on (111) plane, and one twin with 2 layers of atoms on $(\bar{1}11)$ plane. These structures indicate that the stress drop events are correlated with the creation and growth of twins in the system. The stress load drops during deformation have been

observed in FCC structure, such as Au-Ag system [5-20] and BCC structure, such as Nb-0.33wt%Zr system [5-21], at very low temperature. But in these experiments, the stress load drops are hard to separate twinning formation effects from adiabatic heating and softening effects, while in our simulation, the stress drop is solely due to twinning.

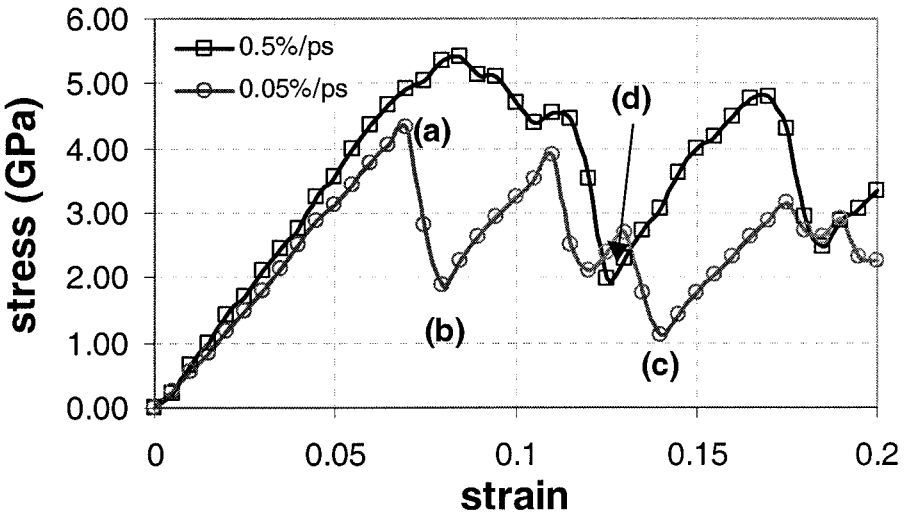

(I)

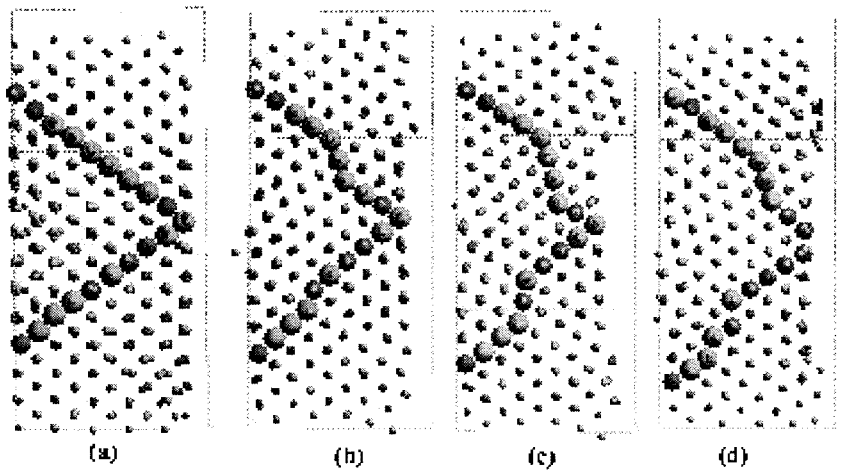

(II)

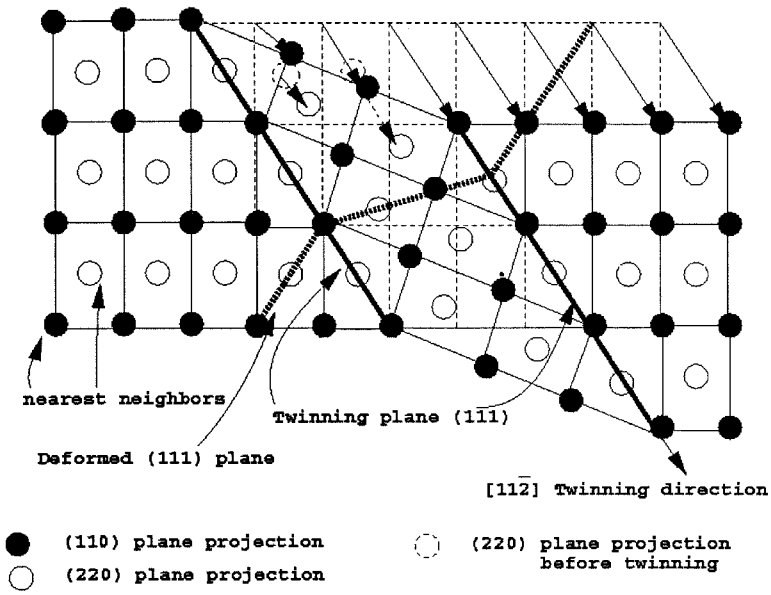

(III)

Figure 5-3 I, stress-strain curve up to 20% strain of strain rates 0.05%/ps and 0.5%/ps showed the detail of first several load dropping and reloading events.

II, snapshot of structures for NiCu during tensile tests, while the (a)~(d) correspond to the strain states shown in I.

III, schematic of twinning in FCC metals.

The twin formed on a stacking fault and growed layer by layer, which consist with Cottrel and Venables' model, where Cottrell and Bilby [5-22] predicted that the FCC structure would produce only a monolayer stacking fault, and Venables [5-23] suggested a modified mechanism to allow a continuous growth of twin from a single stacking fault.

The formation of twin requires large stress in the system. Figure 5-1 has shown that the system can accumulate more elastic strain energy as the strain rate increases, so that the sample can nucleate more stacking fault for twin growth. Since the system uses the stored elastic energy to form twins, after twin formation the total stress in the system will get released. The more twins form, the more stress can release. We compare the structure of NiCu after the first stress drop (at 12.5% strain state) under strain rate of 0.5%/ps in Figure 5-3(II)d, which contains two three independent monolayer stacking faults on the (111) planes, and the structure after the first stress drop under strain rate of 0.05%/ps in Figure 3(II)b, which contains two independent twins. The first stress drop under strain rate of 0.5%/ps is about 3.5 Gpa, which is much larger than the first stress drop of 2.5Gpa under strain rate of 0.0.5%/ps, due to the more stacking fault formed. Therefore, the released stress generally increases with increasing number of stacking faults. However, the twin formation also takes time; when the strain rate continues to increase, the system will not have enough time to form a complete relaxed twin structure. This leads to an even smaller stress drop, which can be observed in strain rate of 1%/ps and 2%/ps.

5.5 From twinning to disordered phase

Figure 5-2 shows that after the single crystal turned to a multi-oriented crystal by continuous twinning and multiple shearing, the grain sizes, at the same strain state but different strain rates, are quite different. We can show qualitatively that the grain size is decreasing as the strain rates increases.

We developed an algorithm to find the FCC structures in any structure. We start from an atom having 12 nearest neighbors with an ABC packing sequence as a part of a perfect FCC crystal; from it we check the atoms in far nearest neighbors, and stop at the atoms, which lost the FCC nearest neighbor's configuration. This method can group atoms within one FCC grain and identify the stacking fault on a twin boundary, or any kind of grain boundary between FCC crystals. Using this method we count the atoms inside the boundary as the grain size.

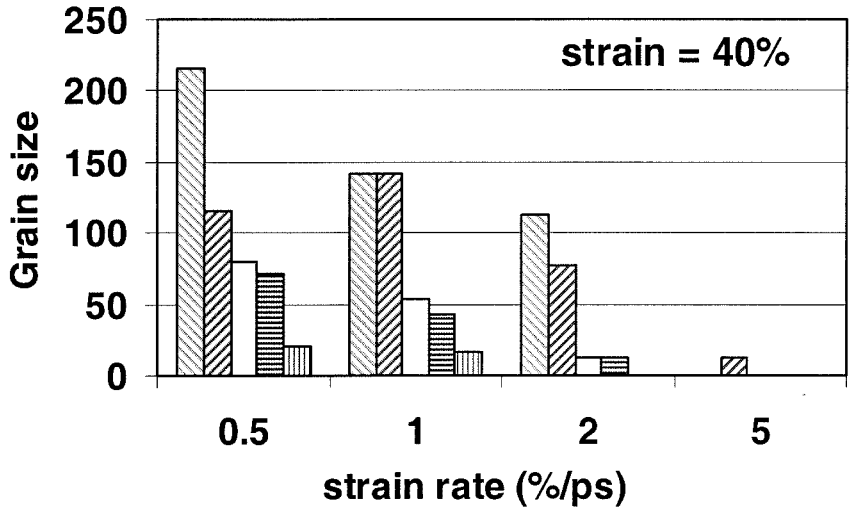

Figure 5-4 Grain size of multi-grain crystalline at 40% strain state, after twinning deformation (0.5%/ps, 1%/ps, 2%/ps) and amorphization (5%/ps).

The grain sizes at ε_{33}=40% during different strain rates tensile process are calculated by this method, and the results are given in Figure 5-4. At strain rate of 0.5%/ps, we got one grain with 215 atoms and one with 115 atoms, at strain rate of

2%/ps, we still have one grain with 112 atoms, while at strain rate 5%/ps, we only found one little cluster with 13 atoms with an FCC structure. The size of grains decreases as the strain rates increase by two reasons: one is more nucleus can form when more stress is accumulated under high strain rate, and the other is more twins can release more stress energy during less relaxation time. As a result, the deformed nanowire tends to form more twins and smaller grains as the strain rates increase.

Therefore, we propose a deformation mechanism at high strain rates here. The twin is considered as a unit. Its size decreases as the strain rate gets higher. As the strain rates get so high that either the system doesn't have enough time to form twin or these units lose their coherent relation, and get smaller than 12, the number of nearest neighbors for FCC structures, a disordered system emerged. This is the strain rate induced amorphization behavior we observed at 5%/ps strain rate, when system flows like liquid after the transition and the detail of the structural change can be found in the paper by Ikeda *et al.* [5-10]

5.6 The recovery of shear modulus after twinning and shear instability in amorphization

Figure 5-5 shows that the tetragonal shear modulus in the xy plane, $(C_{11}- C_{12})/2$, decreases linearly with increasing strain for all strain rates (pure Ni at T = 300K) up to ~ 7% strain. However, for $\dot{\varepsilon} \leq 0.5\%$/psec, the shear modulus suddenly increases at 7% strain state back to its original value. This is due to the relaxation of stress by twinning or coherent shearing (Figure 5-3). The linear extrapolation of $(C_{11}- C_{12})/2$ to zero would predict a vanishing shear modulus at 11% strain.

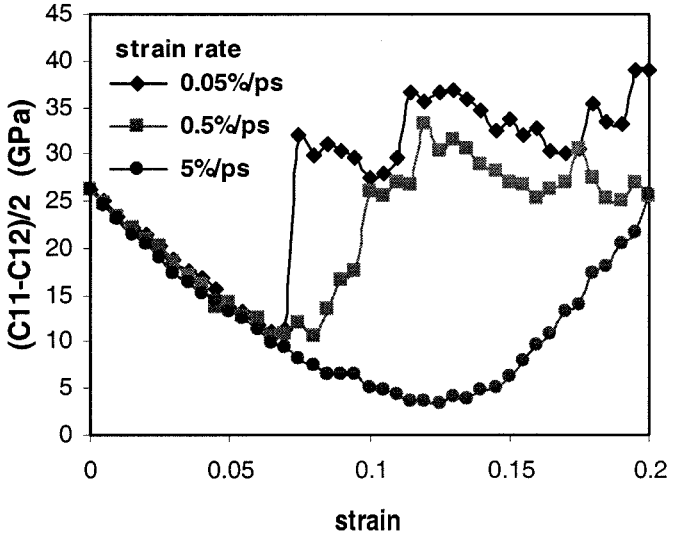

Figure 5-5 Tetragonal shear modulus (C11-C12)/2 for strain rate of 0.05%/ps, 0.5%/ps and 5%/ps. In all strain rates, the shear modulus decrease with increasing strain at first, but for strain rates of 0.05%/ps and 0.5%/ps, shear modulus recover to its original value due to twinning, and at strain rate of 0.05%/ps, the shear modulus approaches to a shear instability condition under glass transition.

Such a vanishing of the shear rigidity is associated with the solid to liquid transformation [5-24] (either the rhombohedral shear modulus (C_{44} for cubic) or the tetragonal shear modulus (C_{11}-C_{12})/2 for cubic[5-25]). Tallon [5-26] showed that the shear moduli decrease with increasing temperature in such a way as to extrapolate to zero at a critical temperature above the thermodynamic melting temperature, T_m. He also found that this instability is triggered by the vanishing of (C_{11}-C_{12})/2 rather than C_{44}. Recently, Wang *et al.* [5-27] derived modified stability conditions for the case of strained solids by including the hydrostatic pressure into the strain tensor, which

becomes important close to the instability. The vanishing of elastic constants near the crystal to glass transition has also been measured experimentally [5-28]~[5-32].

For $\dot{\varepsilon}$ = 5%/psec strain rate (the amorphization case), we find tetragonal shear modulus $(C_{11}-C_{12})/2$ indeed decreases with increasing strain, first linearly, then less rapidly as it approaches the critical condition. It continues to decrease until the shear modulus bends to form a minimum at 12% strain and then finally increases to a limiting value after 30% as the amorphization transition is complete. The deviation from a linear extrapolation from 10 to 12% strain is, we believe, related to the presence of critical shear fluctuations as the system approaches the $(C_{11}-C_{12})/2 = 0$ condition. However, for $\dot{\varepsilon} \leq 0.5\%$/psec, the recovery of shear modulus after twinning avoids the system to approach the shear instability state, which occurs in glass transition.

5.7 Strain rated induced amorphization

The ordering of structure can be represented in radial distribution function (RDF), or G(r). Figure 5-6a shows that for $\dot{\varepsilon}$ = 0.5%/psec the maxima in RDF (expected for a crystalline FCC-system) remain for distances up to 0.55nm, but broaden. In particular, the second nearest neighbor peak around 0.32 nm (associated with the apex to apex distance of the octahedral interstitial sites in the FCC structure) is clearly resolved.

Figure 5-6b shows the RDF for NiCu as a function of strain for $\dot{\varepsilon}$ = 5%/psec. At $\varepsilon = 0.1$ the RDF still shows the peak near 0.32nm representing the octahedral sites, but for $\varepsilon = 0.15$ this peak is gone. Thus, for strains above 0.15 the RDF suggests that

the crystalline phase has transformed to the amorphous phase. This RDF for amorphous state formed under high strain rate has the same patten with the RDF of glass phase formed in fast quenching.

However, starting with the amorphous state achieved at a strain of $\varepsilon = 0.2$ from straining at 5%/psec and then slowing the strain rate to 1%/psec, we found that the sample recrystallizes to form polycrystalline CuNi. Thus for pure CuNi at 300K the critical strain rate to transform and remain amorphous is close to 5%/psec. At strain state of 20%, even the RDF has already shown the amorphous structure, but it still keeps the memory of crystal, so the glass transition is not fully finished at 20% strain.

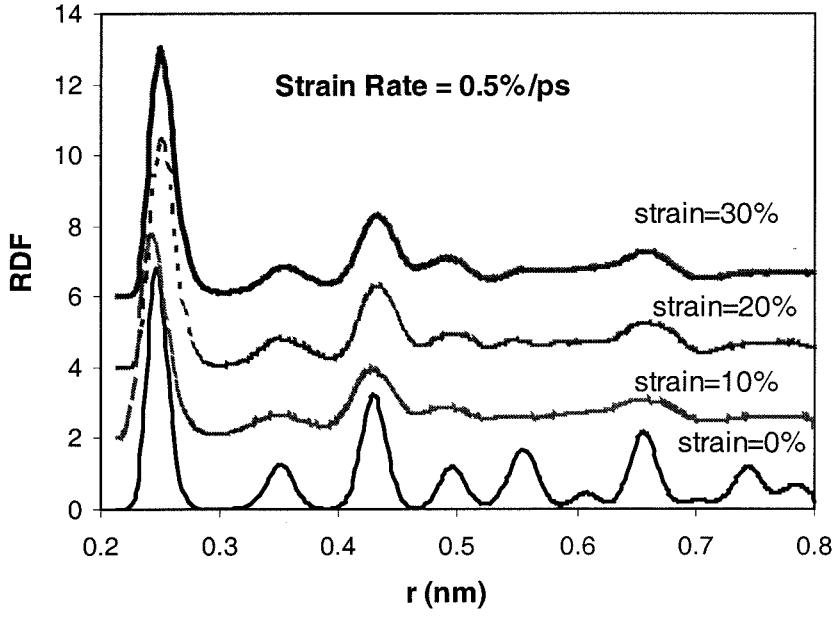

(a)

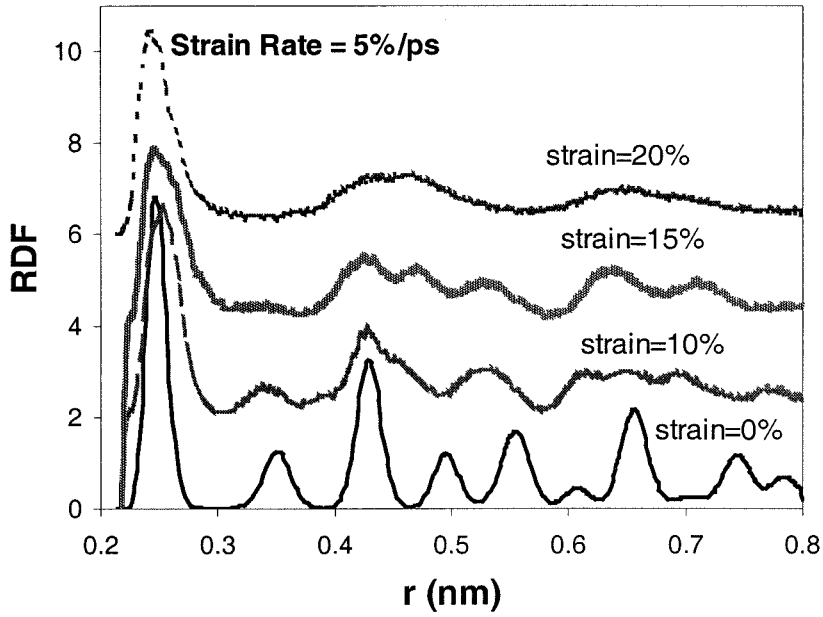

(b)

Figure 5-6 Radial distribution function of NiCu nanowire for various strains at strain rates of (a)0.5%/ps and (b)5%/ps.

The limiting viscosity of η = 0.07 Poise calculated from Figure 5-1, combined with the limiting shear stress of $G_s = (C_{11}-C_{12})/2$ = 50 GPa from Figure 5-7, combined with the Maxwell relation, $\eta = G_0 \tau$, suggests a relaxation time of τ = 1.4 psec. This corresponds to 7% strain in Figure 5-7, which is consistent with the observed relaxation time for the stresses in the amorphous phase.

Figure 5-7 shows the elastic constants for NiCu as a function of strain for $\dot{\varepsilon}$ = 5%/psec. The uniaxial tension in the z-direction breaks the cubic symmetry so that the three independent elastic constants split into six independent elastic constants for the tetragonal system: $C_{11} = C_{22}$, C_{33}, C_{12}, $C_{13} = C_{23}$, $C_{44} = C_{55}$, and C_{66}. By a strain of 0.4 to 0.7, we observe the four independent elastic constants: $C_{11} = C_{22}$, C_{33}, $C_{12} = C_{13}$ =

C_{23}, C_{44}= C_{55} = C_{66} expected for a homogenous amorphous glass under steady state uniaxial deformation. In particular $C_{66} = (C_{11}-C_{12})/2$, as for an isotropic solid. Thus Figure 5-7 indicates that the amorphization process starts at 10% strain but is not complete until 40 - 70% strain (where we find the expected symmetry related degeneracy in the C_{ij}'s). Thus this relaxation takes ~ 8 to 14ps, corresponding to the time for a shear wave to traverse the MD cell a few times. It's still not fully isotropic on the sense of $C_{33}\neq C_{11}(C_{22})$, due to the applied external strain. However, if the constant strain rate stops after 70% strain state, there are only two independent elastic constants in the relaxed amorphous phase, C_{11} and $C_{44}=(C_{11}-C_{22})/2$, indicating a fully isotropic structure. This structure is indeed amorphous; when it is heated up, a glass to liquid transition has been observed as well.

Figure 5-7 shows that the rhombohedral shear moduli $C_{44} = C_{55}$ extrapolate to vanish at a strain of 20%, much higher than for the tetragonal shear (11%), as suggested by Tallon [5-26]. Although the tetragonal shear modulus in x-y plane nearly vanishes at 11% strain, the tetragonal shear modulus in xz and yz planes, $(C_{33}-C_{23})/2$, increases. Thus, the FCC-nanowire first begins to amorphisize in the x-y plane. This behavior is related to the no-periodic boundary condition on this plane. As the nanowire under gets stretched, the surface increases. The atoms on the surface have more free energy to adjust to a disordered phase to release stored elastic energy.

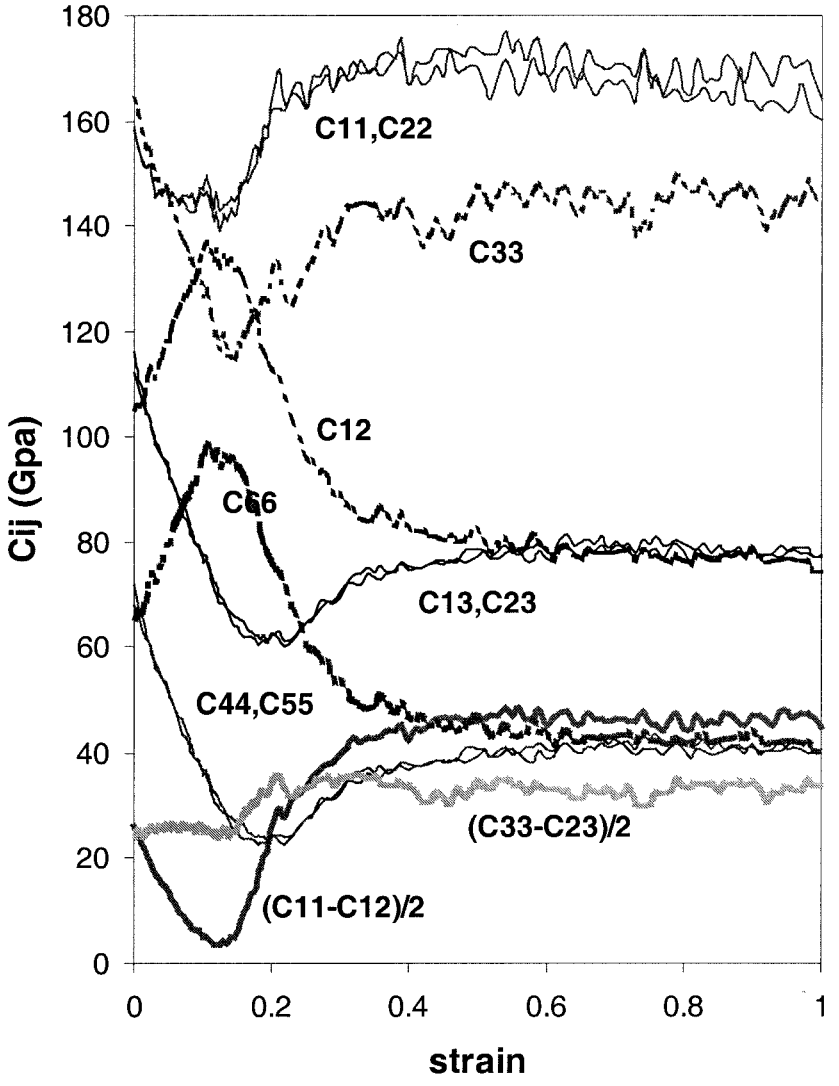

Figure 5-7 Elastic constants for NiCu nanowire under a tensile strain rate of 5%/ps. The strain (along z direction) leads to six independent C_{ij},(C_{11}=C_{22}, C_{33}, C_{12}, C_{13}=C_{23}, C_{44}=C_{55}, and C_{66}). The steady state amorphous phase in uniaxial tension (above 60% strain) has four independent elastic constants.

The strain-rate induced amorphization/melting in homogeneous elastically strained FCC single crystal nanowires is indicated by

- the change in the RDF expected for an amorphous material (loss of the octahedral 2nd nearest neighbor peak at 0.32nm)
- a limiting stress for uniform shear rate (leading to a viscosity of 0.06 Poise)
- the symmetry in the elastic constants [$C_{66}=(C_{11}- C_{12})/2$] expected for an isotropic material, and
- the vanishing tetragonal shear modulus [$(C_{11}- C_{12})/2 \rightarrow 0$] at the start of the transformation

Effectively the strain rate of $\dot{\varepsilon}$ = 5%/ps has transformed crystal to amorphous at 300K. For pure Ni and NiCu alloys we find that the critical strain rate for the crystal to glass transition is below 5%/psec. For strain rates of 0.5%/ps and less, we find cooperative shear events (twins) in the nanowire but no phase transitions.

5.8 Critical strain rate and GFT

The twinning formation requires time that the shear wave can propagate through the whole sample at least twice; since we applied a periodic boundary condition along z direction, the shear wave only needs to travel half of the sample length. Therefore, we can estimate the time required for twin formation. The speed of sound calculated from average of rhombohedral shear modulus C_{44} and tetragonal shear modulus $(C_{11}-C_{12})/2$ is about 2323m/s, the length of the NiCu nanowire is 3.56 nm, and the time for the shear wave to travel half of the sample is 0.76ps. The relaxation time should be on the order of ps for the strained state to finish the twin formation. This explained why

CuNi can't form twin, but uniformly changes into amorphous at the strain rate of 5%/ps, where the simulation time for the strain rate is 0.1ps, which is not enough for twinning relaxation.

The critical strain rate needed to form glass is not only related to the twinning formation time, but also related to the glass forming tendency (GFT) of an alloy. Since the glass formed by high strain rate is the same disordered amorphous phase formed from other process, such as fast quenching liquid to low temperature, the glass formability will follow the same rule as glasses formed by other processes. The size difference and bonding difference (chemical disorder) will improve the glass formability of an alloy. Due to the fact that the size difference of AuNi is 13%, and only 2.5% in CuNi [5-33], similar to slower cooling rate is required to form glass in AuNi than in CuNi, slower strain rate will be required to form glass in AuNi than in CuNi, and we have observed this phenomena in this study. We have studied the strain rate dependence of deformation behaviors in AuNi, CuNi and pure Ni. We found that strain rate of 0.5%/ps is sufficient to obtain amorphous NiAu, but the critical strain rate is about 5%/ps for NiCu and pure Ni. Though the velocities of shear wave in these systems are on the same order (Vs=1809m/s for AuNi and Vs=2486m/s for Ni based on our elastic constants calculation), the critical strain rate to form AuNi glass is at least 100 times slower than that in NiCu and Ni systems. The GFT is more important in determining the glass transition. AuNi has a large size mismatch, which destabilizes the crystalline state with respect to the amorphous state and makes it favor glass formation. Therefore, the critical strain rate required to deform like liquid is much lower than the other two.

From the study we found that increasing strain rate has the same trend of lowering the temperature. In deformation mechanics, only at low temperature one can observe the deformation twins in FCC metals, while increasing strain rate can also favor twin formation. In terms of phase transformation, it's well known that fast cooling can freeze liquid into glass, while the fast strain rate beyond the relaxation time of the system, a disordered phase, amorphous also can form. To combine the effects of high strain rate and fast cooling in glass formation, we believe that the critical strain rate is also a function of temperature.

5.9 Conclusions

We studied the deformation behavior of Ni, CuNi and NiAu at high strain rate, from 0.05%/ps to 5%/ps. A new deformation mechanism at high strain rate is found. In systems where dislocations cannot be sustained, coherent shear of the atoms can create twins and lower the elastic energy in the system. As the strain rate increases, the size of the twins decreases and the number of twins increases. Beyond the critical strain rate, amorphization occurs, and the specimen deforms uniformly.

References:

[5-1] J.P. Hirth and J. Lothe, *Theory of Dislocations*, Wiley, New York, 1982

[5-2] F.R.N. Nabarro, *Theory of Crystal Dislocations*, Oxford, Clarendon 1967

[5-3] R.W. Cahn, Adv. Phy. **3**,363 (1954)

[5-4] J.W. Christian and S. Mahajan, Prog. Mater. Sci. **39,** 1 (1995)

[5-5] G.A. Ghadwick and D.A. Smith, *Grain Boundary Structure and Properties*, Academic Press, London, (1976)

[5-6] G.T. Gray III, Acta. Met. **36**, 1745 (1988)

[5-7] T.H. Blewitt, R.R. Coltman and J.K. Redman, J. Appl. Phys. **28**, 651 (1957)

[5-8] M. Parrinello and A. Rahman, J. Appl. Phys. **52**, 7182 (1981)

[5-9] F. Milstein, J. Appl. Phys. **44**, 3825(1973), J. Apply. Phys. **44**, 3833 (1973) and F. Milstein and B. Farber, Rhys. Rev. Lett. **44**, 277 (1980)

[5-10] H. Ikeda, Y. Qi, T. Cagin, K. Samwer, W. L. Johnson and W. A. Goddard III, Phy. Rev. Lett. **82**, 2900 (1999)

[5-11] K. Samwer, H. Fecht, and W. L. Johnson in "Glassy Metals III" ed. by H. Beck and H.J. Guntherodt (Springer, Berlin 1994)

[5-12] P. S. Branicio and J-P Rino, Phy. Rev. B **62**, 16950 (2000)

[5-13] S. Chantasiriwan and F. Milstein, Phys. Rev. B. **58**, 5996 (1998)

[5-14] T. Cagin, Y. Qi, H. Li, Y. Kimura, H. Ikeda, W. L. Johnson and W. A. Goddard III, MRS Symp. Ser. **554**, 43 (1999). Also see A. P. Sutton and J. Chen, Phil. Mag. Lett. **61**, 139 (1990) and H. Rafii-Tabar and A. P. Sutton, Phil. Mag. Lett. **63**, 217 (1991)

[5-15] J. R. Ray and A. Rahman, J. Chem. Phys. **82**, 4243 (1985), also M. Parrinello and A. Rahman, Phys. Rev. Lett. **45**, 1196 (1980)

[5-16] W. G. Hoover, Phys. Rev. A **31**, 1695 (1985)

[5-17] J.R. Ray, Comput. Phys. Rep. **8**, 109 (1988)

[5-18] R. A. Swalin, Thermodynamics of Solids (Wiley, New York, 1962)

[5-19] R. W. Hertzberg, Deformation and Fracture Mechanics of Engineering Materials (John Wiley & Sons, New York, 1989)

[5-20] H. Suzuki and C. S. Barrett, Acta. Met. **6**, 156 (1958)

[5-21] W. J. Botta, J. W. Christian and G. Taylor, Phil. Mag. **57**, 703 (1988)

[5-22] A.H. Cottrell and B.A. Bilby, Phil. Mag. **42**, 573(1951)

[5-23] J.A. Venables, Phil. Mag. **6**, 379(1961)

[5-24] G.E. Dieter, *Mechanical Metallurgy*, McGraw-Hill, New York (1986)

[5-25] M. Born, J. Chem. Phys. **7,** 591 (1939), also M. Born, Proc. Cambridge Philos. Soc. **36**, 160 (1940)

[5-26] J.L. Tallon, Nature **342**, 658 (1989)

[5-27] J. Wang, J. Li, S. Yip, D. Wolf and S. Phillpot, Physica A **240**, 396, (1997)

[5-28] C. Ettl and K. Samwer, Mat. Sci. Eng. A **178,** 245 (1994)

[5-29] R. Hassdorf, M. Arend and W. Felsch, Phys. Rev. B **51**, 8715 (1995)

[5-30] P. R. Okamoto et al., J. Less-Common Metals **140**, 231 (1988)

[5-31] J. Chevrier and J. B. Suck, Phys. Rev. B **49**, 961 (1994)

[5-32] U. Herr, Habilitationsschrift Univ. Augsburg 1998, to appear in Mat. Science Rep

[5-33] C. Kittel, Introduction to Solid State Physics, 7^{th} ed. (Wiley, New York) (1996)

Chapter 6 Screw Dislocation Structure, Annihilation and cross-slip in Ni

6.1 Introduction

Dislocations are important factors in controlling the mechanical properties of ductile materials. Classic continuum dislocation theory [6-1] provides an understanding of the basic properties of dislocations and interactions of dislocations in elastic regime. But atomistic simulations can provide the description of interaction of dislocations in short range, which is beyond the scope of dislocation theory, and the detailed structures of dislocation, which are limited by the experimental observation scope. Large scale atomic simulations, as an important link on the multiscale simulation of mechanical properties of materials, generate important energetic information for modeling at continuum theory and dislocation dynamics levels.

In FCC metals, the perfect screw dislocation, with Burgers vector $b=\frac{1}{2}\langle 110\rangle$, dissociates into a pair of Schockley partials separated by an intrinsic stacking fault to lower the energy [6-1]; the properties of these partials are dominant factors in the study of motion and interaction of dislocations. Since these dislocations are no longer linear but planar objects due to the dissociation, the simple line shape model of screw dislocation is not accurate any more. And the annihilation process of two dislocations of opposite signs becomes more complicated than simply canceling with each other if their separation is less than a critical value, as assumed in meso-scale modeling [6-2]. Swaminarayan *et al.* [6-3] and Rasmussen *et al.* [6-4] studied the motion and annihilation of dislocations in copper from an atomistic point of view, but still treated

the screw dislocation as a line object. In our study, we believe that due to the dissociation of the perfect screw dislocation, different configurations of dislocation dipoles need to be considered; and the process of dipole annihilation in Ni is the main focus of this chapter.

Cross-slip (where screw dislocations move from one slip plane to another one) is a fundamental factor in determining the mechanical behavior of FCC metals. For example, it is related to the onset of stage III in the stress strain curve of single crystals, where the rapid, linear work-hardening stage ends, and the cross-slip rate increases sharply under the accumulated stress [6-5]. While perfect screw dislocation can cross-slip freely because there is no defined slip plane, the dissociated dislocations in FCC crystals require an external force to cross-slip due to defined dissociation plane and the edge components of their partials. The classical theory requires the partials to recombine into one perfect dislocation in order to cross-slip. Freidel-Escaling's model of this constrain process [6-5][6-6] states that on the primary slip plane the partials must be recombined over a short length, either by applied stress or by thermal fluctuation, then the part of screw dislocation can re-dissociate on the cross-slip plane. These classical models describe the dislocation line tension and calculated the activation enthalpy of cross-slip. Recently Duesbery studied two-dimensional rigid dislocations in copper with atomistic simulations [6-7]; he finds that cross-slip can occur without the constriction of the partials in the primary plane if the shear stress is large enough. And Rasmussen *et al.* [6-8] calculated the activation energy for cross-slip in copper in 3D from MD simulation; the activation energy is close to the enthalpies calculated by Duesbery *et al.* [6-9]. But they used a

predetermined path for cross-slip, instead of a fully relaxed process taken by the system. We will study the natural process of cross-slip in Ni using dislocation dipoles in a periodic simulation cell.

All these simulations were calculated by a parallel MD code, MPiSIM[6-8], which can simulate systems with hundreds of thousands of atoms easily. And the interaction of Ni is described by a quantum effected modified Sutton-Chen (QMSC) many-body potential, which gives accurate values of elastic constants and surface energy [6-11]. In this chapter we'll first discuss the dissociation, core energy and core structure calculations in section 6.2. Since the screw dislocations can dissociate on two equivalent (111) planes, there are three configurations of the dipole: a) the two dislocations dissociate on the same slip plane; b) they dissociate on two intersecting slip planes, and c) on two parallel slip planes. We'll study the dislocation motion, annihilation and cross-slip using a dislocation dipole in a periodic simulation in section 6.3~6.5. We will show the different annihilation processes due to dissociation plans' configurations.

6.2 Core structure and core energy

The challenging of atomic simulations of dislocation is the simulation size and the boundary condition, since interactions between dislocations and between dislocation and surface are very long range. There are several models available. 1) Two regions model, which contains a free relaxed core region and a linearly elastic region, has been used to study core structures [6-12][6-13]. This model can use a few thousands of atoms. But to study the motion of dislocations, one needs to keep updating the

boundary and region limits in this model. 2) A system large enough so the surface effects can be ignored [6-14]; in such simulations millions of atoms will be used. 3) A system with periodic boundary condition without free surface, which requires the net Burgers vector of the cell to be zero. Using this method, a periodic cell as small as hundreds of atoms can be constructed and calculated even at *ab initio* level [6-15]. In our simulation we used either a cylinder model with free surface or dislocation quadrupole structure with a 3-D periodic boundary condition.

The cylinder model contains only one screw dislocation at the center with b=1/2[110]. The model has periodic boundary condition along z direction, parallel to the dislocation line. The screw dislocation can be constructed in an FCC lattice, by using the displacements obtained from elastic theory,

$$u_b = \frac{b\theta}{2\pi} \tag{6-1}$$

where θ is the angle between a fixed direction and the vector from the dislocation line to the actual atom. Then all atomic positions are relaxed with energy minimization. The dissociation from a perfect screw dislocation into two partials is instantaneous. Parallel to [110] direction, there are two glide planes, $(1\bar{1}1)$ and $(\bar{1}11)$. the splitting can occur on either one of these two planes as follows:

$$(1\bar{1}1) \text{ plane: } \frac{1}{2}[110] \rightarrow \frac{1}{6}[121] + \frac{1}{6}[2\bar{1}\bar{1}],$$

$$(\bar{1}11) \text{ plane: } \frac{1}{2}[110] \rightarrow \frac{1}{6}[211] + \frac{1}{6}[12\bar{1}]. \tag{6-2}$$

The cylinder model contains 12684 atoms, the radius is 5nm and the length along z direction is 7 Burgers vector. The central three layers of $(1\bar{1}1)$ planes in the

relaxed structure are shown in Figure 6-1. We colored three layers of $(1\bar{1}1)$ planes in color. Perfect FCC packing, ABC packing, is seen to the left and to the right of the partials, and HCP packing, ABA packing is shown between two partials.

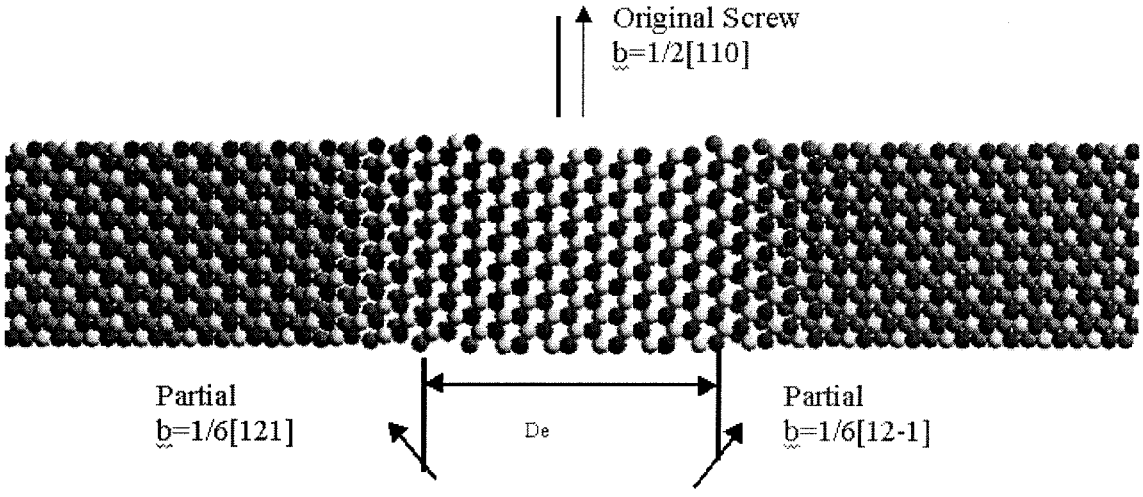

Figure 6-1 Three layers of $(1\bar{1}1)$ planes after screw dislocation dissociated into two partials. Perfect FCC stacking fault is seen outside the core region; the stacking changes gradually from FCC to bridge to HCP between the two partials.

Even though the cylinder radius is 5nm long, it's still under surface influence. In order to get more accurate relaxed core structure and energy, we build the dislocation quadrupole system in a simulation cell with 3-D periodic boundary condition, in which there are two dislocations with Burgers vector $\frac{1}{2}\langle 110\rangle$ and two with $\frac{1}{2}\langle \bar{1}10\rangle$. We construct the screw dislocations using the displacements obtained from elastic theory and then all atomic positions are relaxed with energy minimization. The core structure can be represented by differential displacement map (DD map) [6-16],

which displays the relative displacement of neighboring atoms, which is produced by the dislocation; thus it provides the information of local strain. In DD map, the atoms arrangement is shown for two layers of AB packed (110) planes in projection of dislocation line direction. The arrow between a pair of atoms shows the magnitude of the differential displacement along z direction (only the screw component) of the paired atoms. The magnitude of the arrows is normalized to lie between ±b/2, such that a relative displacement of b/2 just connects the two atoms. Figure 6-2 shows the DD map of a constructed screw quadrupole and the relaxed structure. The original screw dislocation as a line object becomes a planar object containing two partials and a stacking fault between them. If we calculate the atomic energy for each atom, the atoms with highest energy are spread on (111) plane, with a planar shape as well.

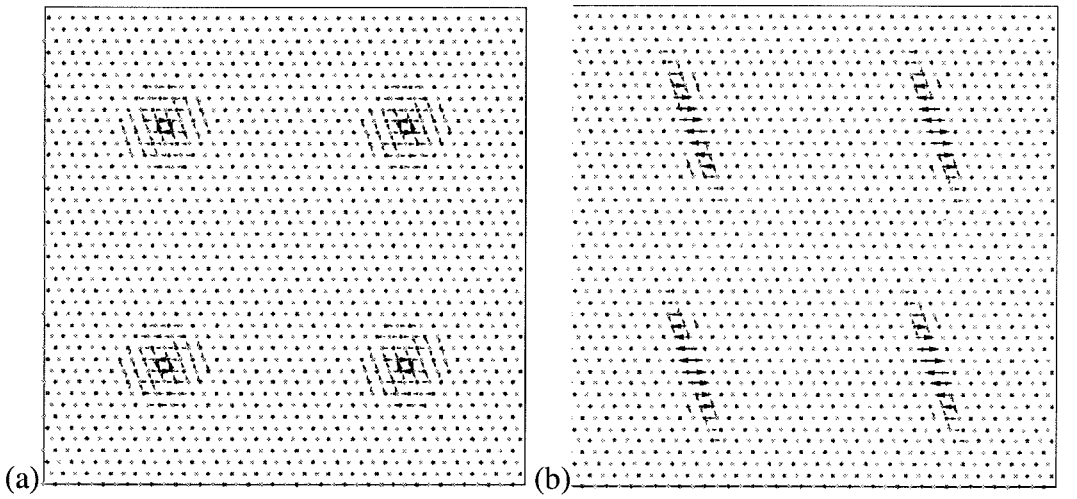

Figure 6-2 Differential displacement map (DD map) of the screw quadrupole periodic structure. (a) Constructed screw dislocations from elastic theory. (b) Relaxed structure, the screw dislocations have dissociated into partials, such that a planar shape is formed.

The total energy of a system containing dislocation quadrupole can be divided into one term associated with the core energy of the dislocations and another term due to elastic field, which can be calculated using linear elasticity theory. For our dislocation quadrupole system, if we consider the dislocations as one object, the total energy can be written as [6-14]:

$$E = E_c(r_c) + \frac{Kb^3}{4\pi}\left[\ln\frac{d_1}{r_c} + A(d_1/d_2)\right] \qquad (6\text{-}3)$$

where E_c is the core energy and the second term is the elastic energy which contains self energies as well as interactions, K is a constant related to the elastic modulus, and d_1, d_2 are the distance of two screw dislocation cores along x and y directions. The term $A(d_1/d_2)$ contains the sum of all dislocation interactions and depends on the geometry of the simulation cell; it can be evaluated numerically. Figure 6-2 shows E/b as a function of $\ln(d_1/r_c)+A(d_1/d_2)]$, for systems of different sizes, ranging from 11760 to 105840 atoms, and the separation between dislocations ranging from 2.8nm to 12.9nm. We found the atomistic results follow the straight line predicted by elasticity theory (Eq. 6-3). From a linear fit we find the core energy to be E_c=0.544 eV/b and the elastic modulus K=44.64 GPa.

Using our QMSC force field we can calculate the atomic energy associated with each atom. If we define the core as the six atoms with higher energy per partial, we obtain the core energy of each partial as 0.248eV/b, which agrees well with the core energy we got from elastic method (the difference may come from the stacking fault energy between two partials). The core shape of the partials is planar and its length is around 10Å along (111) plane.

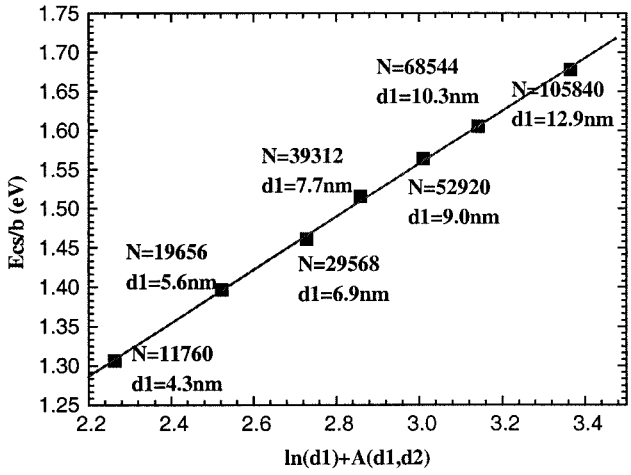

Figure 6-3 Total energy as a function of $\ln[d_1/r_c+A(d_1,d_2)]$ for simulation cells of different sizes. The number of atoms in each simulation is shown.

We define the position of the partial as the atom with the highest energy in the core, which leads to the equilibrium distance of two partials of 25Å. From elasticity theory the distance separating the two partials is given by [6-1]:

$$D_e = b^2(K_s-K_e/3)/\ 8\pi\gamma \qquad (6\text{-}4)$$

where K_s and K_e are anisotropic elastic energy factors for screw and edge components and γ is the stacking fault energy. The calculated D_e is 15.25 Å based on our Force Field values (C_{11}=231.6 GPa, C_{12}=161.5 GPa, C_{44}=99.85 GPa, γ=40mJ/m^2, a=3.46Å), less than the one obtained from the simulations. Similar behavior was found by Duesbery [6-7] and Rasmussen [6-8] in Cu.

6.3 Dislocation dipole annihilation: dissociation on the same plane

We studied dislocation motion, annihilation and cross-slip via dislocation dipole (two screws with opposite Burgers vectors) in a periodic simulation cell. Our dipole simulation cells contain 22050 atoms (15.03 nm along x direction and 9.11 nm along y direction). The orientations of the cell are: x direction along $<\bar{1}1\bar{2}>$, y direction along $<\bar{1}11>$, and z direction along <110>. The distance of the centers of two opposite sign screw dislocations was 9nm along x.

The simplest case is that two screws dissociate on the same sliding plane, $(1\bar{1}1)$ plane. The dissociation reactions are $\frac{1}{2}[110] \rightarrow \frac{1}{6}[121] + \frac{1}{6}[2\bar{1}\bar{1}]$ and $\frac{1}{2}[\bar{1}\bar{1}0] \rightarrow \frac{1}{6}[\bar{1}\bar{2}\bar{1}] + \frac{1}{6}[\bar{2}\bar{1}1]$. So the attraction force will cause two partials with opposite sign in the middle to annihilate first. Then a structure with a stacking fault between the other two opposite signed partials will form, so the attraction force between the partials and driving force for decreasing stacking fault energy will accelerate the annihilation process. At the end a perfect FCC crystal structure is recovered after annihilation.

6.4 Dislocation dipole annihilation: dissociation on two intersecting planes

A more interesting case, including dislocation motion, annihilation and cross-slip processes, is a dipole with dislocations dissociated on two intersecting planes. In this case, we have 1/2[110] dissociated on $(\bar{1}1\bar{1})$ plane, the reaction is $1/2[110] \rightarrow 1/6[121] + 1/6[2\bar{1}\bar{1}]$, and $1/2[\bar{1}\bar{1}0]$ dissociated on $(\bar{1}11)$ plane, the reaction is

$1/2[\bar{1}\bar{1}0] \rightarrow 1/6[\bar{2}11] + 1/6[\bar{2}\bar{1}\bar{1}]$. The angle between two sliding planes is 70.53°. Figure 6-4 shows four snapshots of the annihilation process by differential displacement maps. From the DD map, we can see that partial $1/6[\bar{1}\bar{2}1]$ (P3) moves on the $(\bar{1}11)$ plane towards the other dislocation (partials P1 and P2). P1 and P2 have to cross-slip before annihilating with P3, since neither of them has the opposite sign and can be simply canceled. Figures 6-4b and 6-4c show that the distance between P1 and P2 diminishes as P3 approaches them. Then P1 and P2 dissociate into the other two partials, 1/6[211] and 1/6[12-1], such that annihilation can occur between 1/6[-1-21] and [1/6][12-1] and the only partial left is 1/6[211]. As the result, in Figure 6-4d only two opposite signed partials and a stacking fault in between were left; they will annihilate easily due to attraction force and lead to a perfect FCC structure. In Figure 6-4e we show the total energy as a function of time; arrows mark the times associated with the snapshots in Figures 6-4a ~ 6-4d. When annihilation between partials happens (at times ~17ps and ~27ps), the total energy of the system dramatically decreases by ~0.5 eV/b; this is the energy of two partials, as calculated in section 6.2.

During the annihilation process, the screw dislocation ½<-1-10> crossed slip in order to annihilate with ½<110> since they were on different slip planes originally. The approaching of two partials and re-dissociation on the other slip plane are part of the cross-slip process. There is an energy barrier involved, which will be calculated in section 6.5.

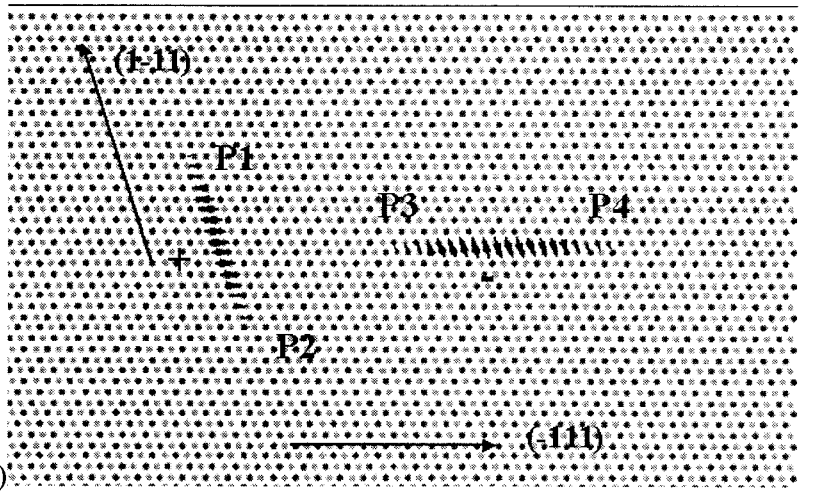

(a)

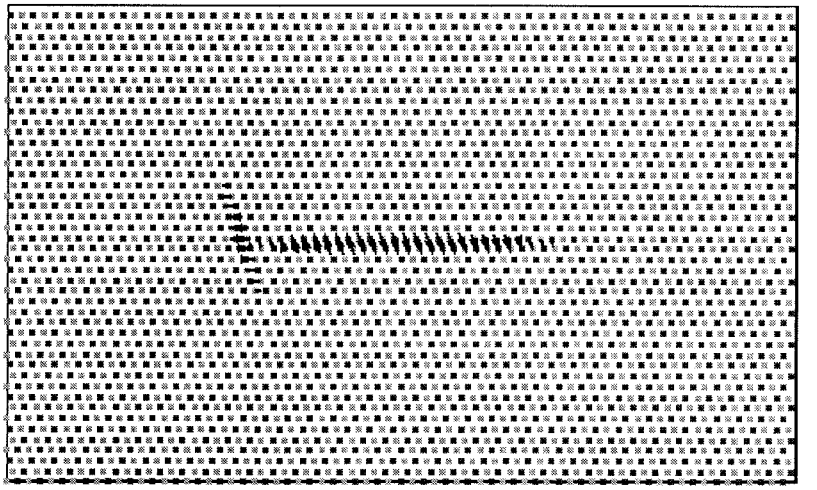

(b)

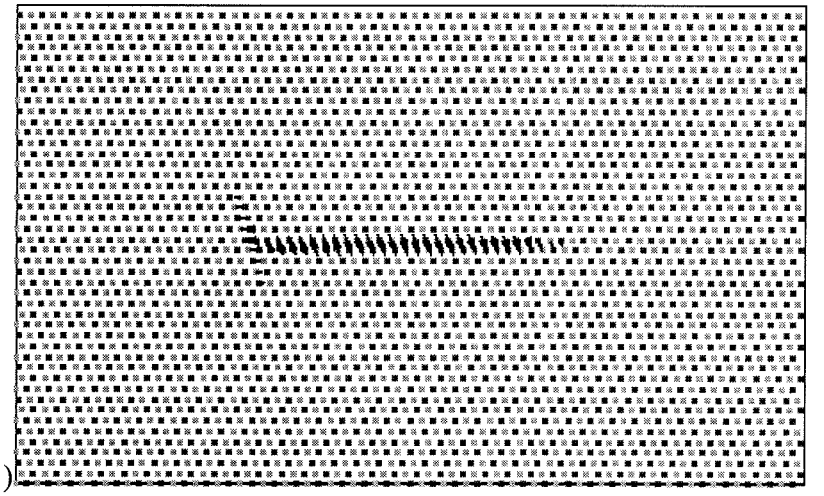

(c)

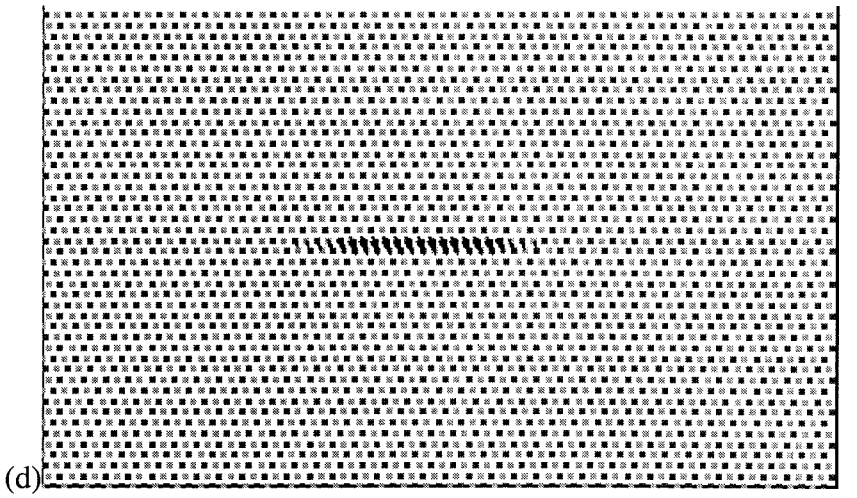

(d)

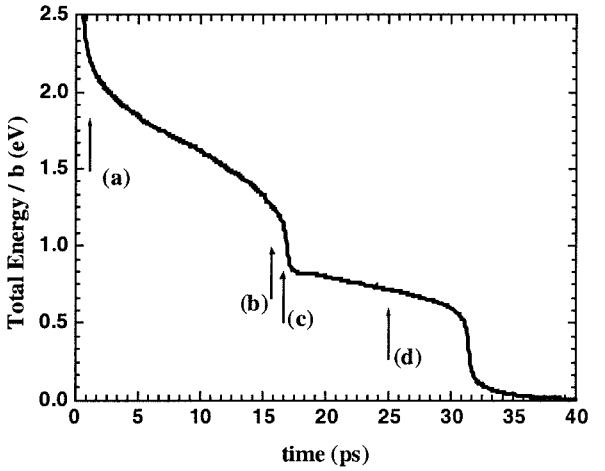

(e)

Figure 6-4 Dislocation dipole annihilation on intersecting slip planes. Differential displacement maps at different times: (a) t = 0ps, (b) t = 16ps, (c) t = 1.75ps, and (d) t = 25ps. (e) shows the time evolution of the total energy of the system.

6.5 Cross-slip: dislocation dipole with dissociation on two parallel planes

An important parameter, related to cross-slip, is the minimum stable dipole distance of opposite signed screw dislocations dissociated on parallel planes; see

Figure 6-5a. In this configuration both dislocations need to cross-slip in order to annihilate.

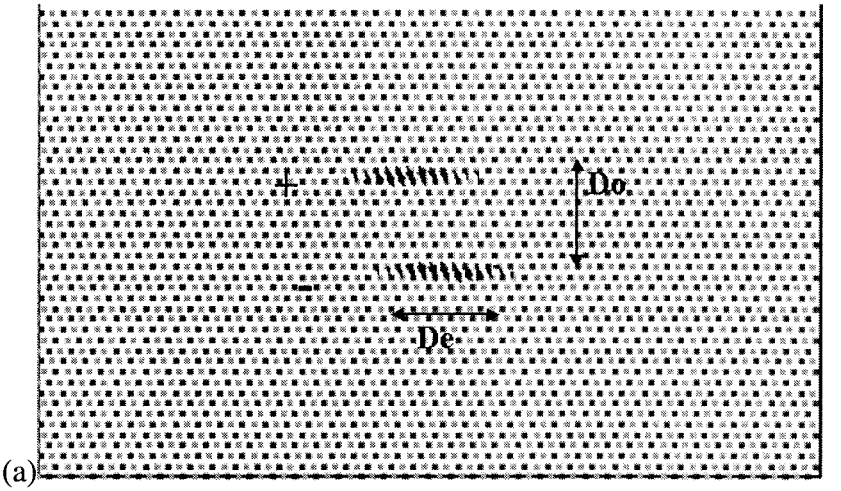

(a)

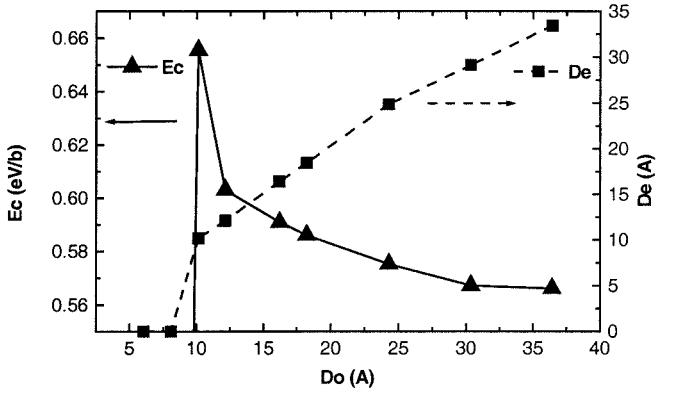

(b)

Figure 6-5 Dislocation dipole dissociated on parallel planes. (a) Differential displacement map of the system setup. (b) Core energy (left vertical axis) and separation between partials (right vertical axis) as a function of the distance between the planes.

When two partials are approaching each other, the energy will increase, which related to the energy barrier of the cross-slip process. So we calculated the structure and core energy of this configuration as a function of distance between the dissociation planes D_o.

In order to cross-slip, the two partials need to approach each other on their primary slip plane. After the distance between the partials (D_e) is less than a critical distance they can cross-slip. Both D_e and the core energy depend on D_o. In Figure 6-5b we plotted D_e and E_c as a function of D_o. As expected D_e decreases and E_c increases as the dislocations get closer. When the dipole separation Do is less than 8Å, the dislocations cross-slip and annihilate. We obtain the energy barrier for this cross-slip process to be 0.1eV/b.

6.6 Conclusions

We studied the 1/2a<110> screw dislocation in Ni, which dissociates into two partials separated by 25Å; the core energy is 0.5 eV/b. Using molecular dynamics we studied dislocation motion and annihilation.

The annihilation process of a screw dipole depends on how the two dissociation planes are configured. When the two dislocations dissociate into intersecting planes we find that one dislocation cross-slips in the presence of a third partial coming from the opposite signed dislocation.

We also studied two opposite signed dislocations dissociated in parallel planes as a function of the distance between the planes. We find that the separation between the partials decreases and the core energy increases as the two dissociation planes

become closer. When the dipole separation is 8Å, the dislocations will cross-slip and annihilate, and the activation energy for such cross-slip process is 0.1 eV/b.

References:

[6-1] John P. Hirth and Jens Lothe, Theory of Dislocations, 2nd Edition, Krieger Publishing Company, Malabar (1982)

[6-2] M. Verdier, M. Fivel and I. Groma, Modeling simul. Mater. Sci. Eng. **6**, 755 (1998)

[6-3] S. Swaminarayan, R. Lesar, P. Lomdahl and D. Beazley, J. Mater. Res. **13** (1998) 3478

[6-4] T. Rasmussen, T. Vegge, T. Leffers, O. B. Pedersen and K. W. Jacobsen, Phil. Mag. A **80**, 1273 (2000)

[6-5] J. Friedel, *Dislocation and mechanical properties of Crystals*, Wiley, New York (1957)

[6-6] B. Escaig, Dislocation Dynamics, McGraw-Hill, New York (1968)

[6-7] M.S. Duesbery, Modeling Simul. Mater. Sci. Eng. **6**, 35 (1998)

[6-8] Rasmussen, K.W. Jacobsen, T. Leffers and O.B Pedersen, Phys. Rev. B. **56**, 2977 (1997)

[6-9] M. S. Duesbery, N. P. Louat and K. Sadananda, Acta Metall. Mater. **40**, 149 (1992)

[6-10] Y. Qi, T. Cagin and W. A. Goddard III, Computer Aided Materials Design, submitted

[6-11] T. Cagin et al., Materials Research Society Symposium Proceeding **554**, 367 (1998); also A. P. Sutton and J. Chen, Phil. Mag. Lett. **61**, 139 (1990); H. Rafii-Tabar and A. P. Sutton, Phil. Mag. Lett. **63**, 217 (1991)

[6-12] C. H.Woo and M. P. Puls, Philos. Mag. **35** (1977)

[6-13] J. E. Sinclair, P. C. Gehlen, R. G. Hoaland and J. P. Hirth, J. Appl. Phys. **49**, (1978)

[6-14] S. J. Zhou, D. L. Preston, P. S. Lomdahi and D. M. Beazley, Science **279**, 1525(1998)

[6-15] S. Ismail-Beigi and T.A. Arias, Phys. Rev. Lett. **84**, 1499 (2000)

[6-16] V. Vitek, R. C. Perrin and D. K. Bowen, Phil. Mag. **21**, (1970)

Chapter 7 Friction Anisotropy at Ni(100)/(100) interface

7.1 Introduction

Macroscopic friction follows Amonthon's Law, which states that the frictional force *f* needed to slide one object laterally over another is proportional to the normal load L, and the constant, $\mu=f/L$, is the dynamic friction coefficient [7-1]. When two solid bodies are placed together in dry contact, they also exhibit static friction, that no relative motion occurs until a threshold force is exceeded. The ratio of Fs, the force needed to initiate motion between objects at rest, and the load L, is defined as the static friction coefficient. However, the origin of this type of friction is not understood. The analytic theories indicated that static friction should vanish at two clean, incommensurate crystal surfaces due to the lack of periodicity, and is maximum when surfaces are commensurate [7-2][7-3]. These models only focus on intrinsic factors, such as interactions between constituent atoms, while the other factors such as surface roughness, fractures, plastic deformations, and contaminants are not considered.

Recently, Ko and Gellman studied friction anisotropy at Ni(100)/Ni(100) interfaces [7-4]. They found the static friction coefficient between two clean Ni(100) surfaces was $\mu=8.6\pm2.5$, and it reached a minimum, $\mu=2.5\pm1$, when two surfaces were mis-orientated by 45 degrees. Even though the reason for this anisotropy is not clear, the static friction at mis-oriented interface didn't vanish. This result also conflicts with the Hirano *et al.*'s measurement on mica surfaces, where they found the friction force anisotropy strongly depends on the "lattice misfit angle" [7-5].

Robbins et al. have used MD simulations to study the origin of static friction anisotropy and proposed a simple model that the absorption of "third body," such as small hydrocarbon molecules, can cause the static friction of two macroscopic objects [7-6]. But the experiments on Ni(100)/Ni(100) interface were carried out in a highly controlled ultrahigh vacuum environment (UHV) and carefully showed that no impurities are present on the surface (as measured by AES) and that the surfaces were well ordered (as measured by LEED). However, the surface is not atomic flat after mechanical polish in the experiment. Such that under dry sliding condition, the surface roughness and dislocations generated during sliding should be considered in the model. The object of this study is to understand the origin of friction anisotropy and the difference between prediction of analytic theory and experimental results.

We carried out a series of Non Equilibrium Molecular Dynamics (NEMD) simulations for sliding of Ni(100) interfaces under a constant force, which is designed to mimic the experimental conditions. The details of the calculations are described in section 7.2. In our study we analyze the effect of surface roughness, by comparing the differences in both static friction coefficients and dynamic friction coefficients due to atomic flat and rough surfaces. These results are presented in section 7.3, and the significance of the current simulation results and comparison with experimental results are discussed in section 7.4.

7.2 Simulation methods development

7.2.1 Calculation methods

We used the quantum modified Sutton-Chen(QMSC) type many-body force field (FF) to describe the interactions of Ni. The parameters for this FF were determined to match the experimental properties of bulk Ni (density, cohesive energy, compressibility, elastic constants, and phonon dispersion). In doing the fitting, we included the zero point motion of the vibrations [7-7]. This QMSC FF has previously been used to study structural transitions between various phases of Ni, Cu and other face centered cubic metals [7-8].

In our molecular dynamics simulation, we first prepare the sample, by relaxing the up and lower slabs of Ni for 20ps at 300K respectively to reach equilibrium, then bringing the two slabs of material together for another 20ps relaxation. During these relaxations, constant temperature and constant volume molecular dynamics (ThN MD) [7-9] was used. And the sample is non-periodic along z axis, but periodic along x and y directions, to mimic two thin films.

After the sample is fully relaxed, external forces are applied to simulate the sliding process. Figure 7-1 shows the y projection of the 2D Periodic Cell (x and y periodic, z non-periodic) used for the steady state NEMD tribology simulations. Z direction is parallel to <001> direction in Ni, and x, y directions are chosen based on the orientation of the sliding experiments. In all the models, there are 7 layers of (001) planes in both slabs. Two rigid slabs, where all atoms move as a unit, are defined at the top and bottom, with each slab containing $N_r = 6$ layers of atoms. At each time step, all the atoms in the rigid slab were imposed an external force of Fs, which is in the +x direction for the top slab and in the –x direction for the bottom slab. The top layer in the top rigid slab and bottom layer in the bottom slab are

constrained not to move in the z direction, to simulate the sample under compression, such that the sample is actually fixed in the length along z direction. The central two slabs, each with $N_f = 1$ layer of atoms, are fully flexible and allowed to move freely under the force field. The rigid slabs are thermostated to a fixed temperature T=300K (isokinetic energy by scaling the velocity). The flexible slabs are treated adiabatically. The normal force $\langle F_n \rangle$ per atom is calculated from the average compression stress times the contact area and divided by the number of atoms. The average of total lateral force on the top rigid slab per atom is calculated as $\langle f_x \rangle$, which is summed over all atoms of the top rigid slab and averaged over time and the number of atoms. And it should be equal and opposite to the lateral force on the bottom rigid slab.

We apply the external force until two slabs start sliding with respect to each other. The minimum force needed to initiate motion is defined as Fc, such that the static friction coefficient is defined as

$$\mu_s = 2F_c / \langle F_n \rangle \qquad (7\text{-}1)$$

where F_n is the normal load.

However, the average atomic net forces $\langle f_x \rangle$ in the upper and lower slabs are not equal to applied force after the two pieces started to move. This difference is caused by the frictional force, f, on the interface.

$$f = F_s - \langle f_x \rangle \qquad (7\text{-}2)$$

We validated that the relative acceleration of two bodies is due to the net force, such that $a=2\langle fx \rangle/m$, where m is the atomic mass. From the ratio between the frictional force and normal load, the dynamic friction coefficient can be calculated as

$$\mu_d = 2f / \langle F_n \rangle. \qquad (7\text{-}3)$$

The unit of force is (kJ/mol)/nm/atom = $1.66*10^{-12}$N/atom in this chapter.

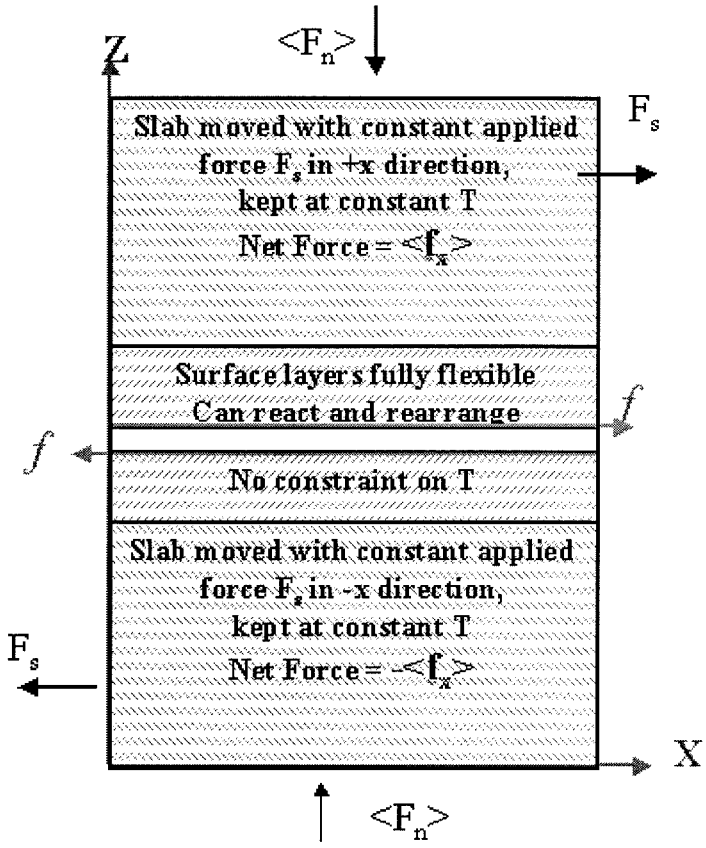

Figure 7-1 Projection along y direction of a 2D periodic (along x and y directions) cell for Tribosimulations (steady state nonequilibrium molecular dynsmics). Fs is the applied external force on two moving slabs with 6 layers of atoms. *f* is the frictional force during the sliding of two slabs, and <Fn> is the normal load on z direction.

7.2.2 Orientations and mismatch angels on interface

We have examined here the effect of orientation on both the dynamic and static coefficient of friction for three orientations of the bottom rotated with respect to the top, as shown in Figure 7-2:

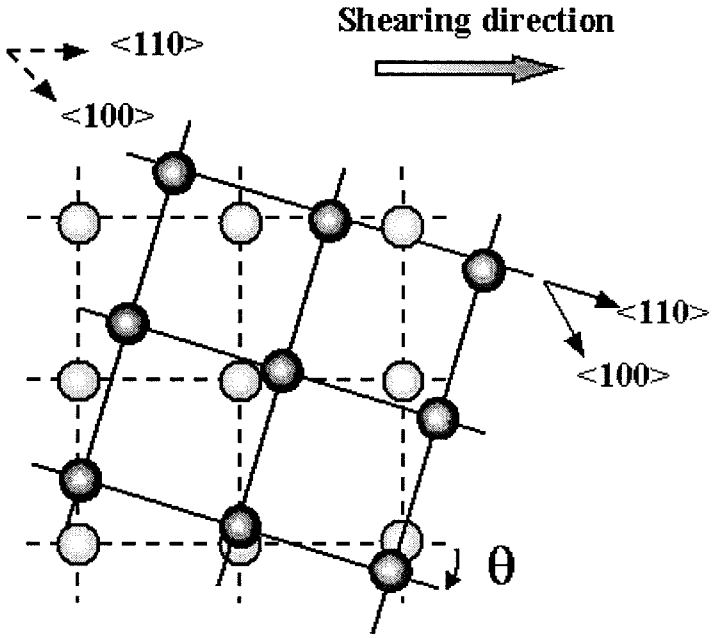

Figure 7-2 Schematic diagram showing the lattice mismatch of Ni(100) sample surfaces in simulations. The dark circles are lattice of upper slab and light circles are lattice of lower slab, θ is the lattice misorientated angle between upper and lower slabs. The sliding direction is controlled along x direction of simulation cell.

- θ=0° corresponds to the case where both surfaces are aligned. This system is expected to have a very high coefficient of friction, particularly for the static friction in perfect crystal case. In this case, the direction of sliding is taken as the <110> direction for both slabs, the same as the experiment. For each slab, the simulation size is $7\sqrt{2}a$ X

$7\sqrt{2}a$ X 14a along x,y and z directions respectively, while the total number of atoms in the system is N=5488.

- θ=45° corresponds to the case of the maximally misoriented surface, where the <110> axis of the lower surface matches the <100> direction of the top surface. In this case, the direction of sliding is taken as the <100> direction of the upper slab and <110> for lower slab. Since we applied periodic boundary condition along x and y directions, the sizes for both slabs should be equal on these two directions. In this case we choose 10aX10aX7a for lower slab, and $7\sqrt{2}a$ X $7\sqrt{2}a$ X7a for upper slab, then stretch the upper slab to 1% tension strain to reach 10a. Such that the misorientation causes the lattice mismatch too, while we minimized this mismatch such that it can be ignored. The total number of atoms in this system is 5544.
- θ=29.7° (We denote it as θ=30° for simplicity) where the x direction is <110> for lower slab and <-3 11 0>for upper slab. To minimize the lattice mismatch, we choose $4\sqrt{2}a$ X $4\sqrt{2}a$ X7a for lower slab and $\sqrt{130}a/2$ X $\sqrt{130}a/2$ X7a for upper slab, then stretch the upper slab to 0.7% compression strain to reach the same length of lower slab. The number of atoms in simulation cell is 1806.

7.2.3 Surface roughness

We constructed three surface structures, then the flat and rough surfaces were used for all orientations.

- The perfect interface, where each surface was atomically flat and clean. When the surfaces start with the atoms of the top and bottom surface aligned (θ=0°), these layers are slipped with respect to a single crystal.
- The random rough interface, where 25% of the atoms at the interface of each surface were randomly deleted. Here the top and bottom surfaces were treated individually.
- The step rough interface. In θ=0° case, we also made a step with a depth of 2 layers of atoms at the interface to make it rough; the simulation data was similar to that of random rough surface.

To obtain the same sliding condition as the experiment, the sliding direction was always along x, while the lattice misorientation angel kept constant during sliding.

7.3 Results and discussion

We have studied flat and random rough surfaces for θ=0°, 45° and 30°. The various cases considered here are summarized in Table 7-1. The applied force Fs, net atomic force <fx>, friction force *f*, and normal force <fn> are defined as in section 7.2.2. The velocity and acceleration are calculated from relative displacement along x direction, between the center of mass of upper and lower slabs.

Table 7-1 Summary of results from NEMD simulations of friction on Ni (100)/Ni (100)

Orientation	Applied Fs	<fx>	Friction *f*=Fs-<fx>	<fn> got from stress	velocity or acceleration	Friction Coefficients μs or μd
θ=0°; flat	5.04	0		0	v=0	
	15.13	0.07	15.13	0.55	v=0	
	20.17	3.035	17.14	2.95	a=0.09 2<fx>/m=0.10	μs≅13.67
	25.2	7.59	17.61	6.36	a= 0.246 2<fx>/m=0.258	μd=5.54
θ=0°; rough	5.04	0	5.04	0.52	v=0	
	10.08	0	10.08	0.89	v=0	
	12.6	0.62	11.98	1.43	v=0.1	μs=17.6
	15.13	3.32	11.81	2.71	a=0.12 2<fx>/m = 0.11	μd=8.71
	25.2	9.2	16	3.97	a=0.35 2<fx>/m = 0.31	μd=8.06
θ=30°; flat	0.029	0	0.029		V=0	
	0.057	0.006	0.051	2.55		μs=0.044
	0.144	0.104	0.04	2.7		μd=0.03
	0.288	0.105	0.183	2.85		μd=0.13
θ=30°; rough	1.44	0	1.44		V=0	
	2.88	0	2.88		V=0	
	4.32	0.15	4.17	0.65		μs=13.3
	5.76	0.26	5.5	0.77		μd=14.3
θ=45°; flat	0.05	0	0.05	1.20	v=0	
	0.255	0.130	0.125	1.19	v=0.082	μs= 0.428
	0.509	0.273	0.236	1.21	a=0.009 2<fx>/m=0.009	μd=0.39
	2.55	1.31	1.24	1.23	a=0.0487 2<fx>/m = 0.045	μd=2.02
	5.09	2.96	2.13	1.22	a=0.111 2<fx>/m = 0.101	μd=3.49
θ=45°; rough	0.509	0	0.509	1.28	v=0	
	2.55	0.06	2.49	1.24	v=0.25m/s	μs=4.11
	5.09	0.75	4.34	1.52	a=0.025 2<fx>/m = 0.026	μd=5.71

7.3.1 Perfect interface (θ=0° and θ=45°)

Figure 7-3 shows the relative displacement in x direction between upper and lower slabs for the Ni (100)/Ni(100) atomic flat interface. 7-3a is for perfect alignment (θ=0°), and 7-3b is for the θ=45° misorientation. Here F_s is the applied force to the rigid slabs.

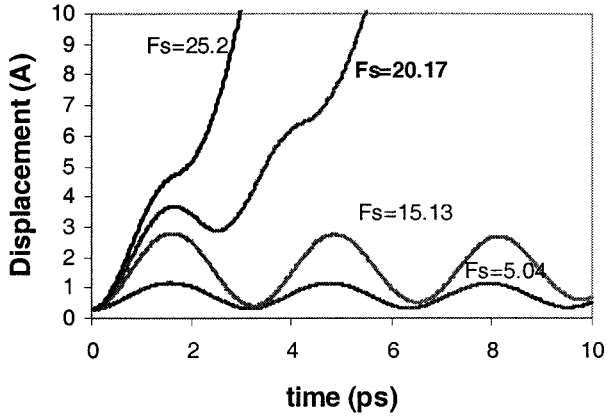

(a)

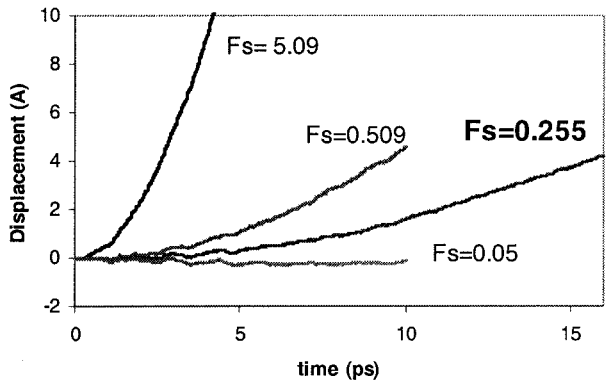

(b)

Figure 7-3 Relative displacement in x direction between upper and lower slabs for Ni(100)/Ni(100) perfect flat interface. (a) for θ=0° aligned case, Fc=20.17 (b) for θ=45° misorientation interface, Fc=0.255.

For $\theta=0°$ we observe oscillatory motion when $F_s=15$ and lower, indicating that this force is less than F_c. There is no such oscillation on $\theta=45°$ misoriention case. The force initiates the motion for $\theta=0°$ is 20; however, the minimal force for $\theta=45°$ is only about 0.255. Clearly, the friction on misoriented interface is much less than (only 1.2% of) the force needed for $\theta=0°$.

Figure 7-4 shows the snapshots of the atomic structure of the systems whose motion behaviors are plotted in Figure 7-3. Figure 7-4a is for $\theta=45°$ misorientation with an applied force of $F_s=0.255$ after 10ps, and Figure 7-4b is for perfect alignment ($\theta=0°$) with $F_s=20.17$ after 5ps.

In the perfect alignment case($\theta=0°$), we noticed that two pieces of materials collapse into one piece when they are brought into contact, and after the interfacial spacing below a critical distance, which was also observed in Ni(100) by using equivalent crystal method and called adhesion avalanche [7-10]. This lead to that the sliding is actually shearing a perfect crystal, and the "friction" is therefore very high. Actually, in the same condition of experiments, cold-weld occurred at the interface, such that the shear force was so large that it approached the up limit of the tribometer, and the experiment had to stop. Thus for the case of perfect alignment ($\theta=0°$), sliding has to be a result of some disorder and plastic deformation generated on the interface during sliding. On the contrast, in the case with $\theta=45°$ the interface was kept flat during sliding.

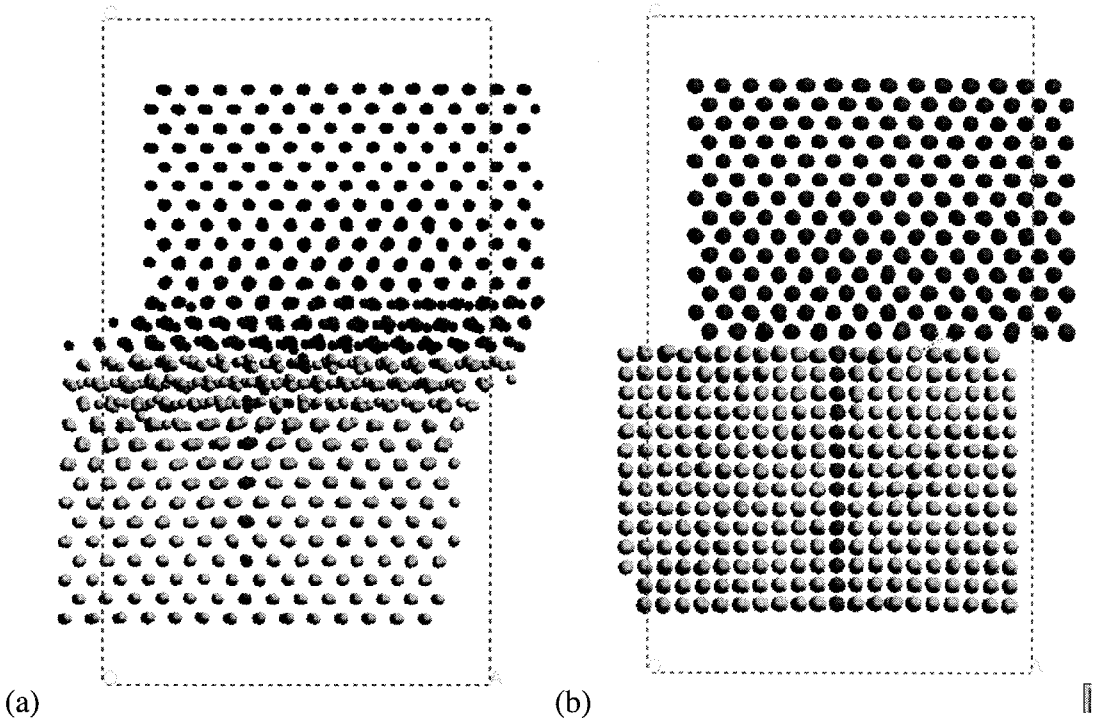

Figure 7-4 Snapshot of atomic structures of the sliding systems with Ni(100)/Ni(100) perfect flat interface, whose performances are plotted in Figure 7-3. (a) for perfect alignment (θ=0°) with applied force Fs=20.17 after 5ps (b) for θ=45° misorientation with Fs=0.255 after 10ps.

7.3.2 Rough interface (θ=0° and θ=45°)

Figure 7-5 shows the displacement in x direction of upper slabs for the Ni (100)/Ni(100) random rough interface. Figure 7-5a is for perfect alignment (θ=0°), and Figure 7-5b is for the θ=45° misorientation. For θ=0° we observe oscillatory motion for F_s = 10 and lower, indicating that these forces are less than F_c. The friction is less for the misoriented surface than for θ=0°, by a factor of 17.8%, which is about 20 times larger than the ratio on atomic flat interface.

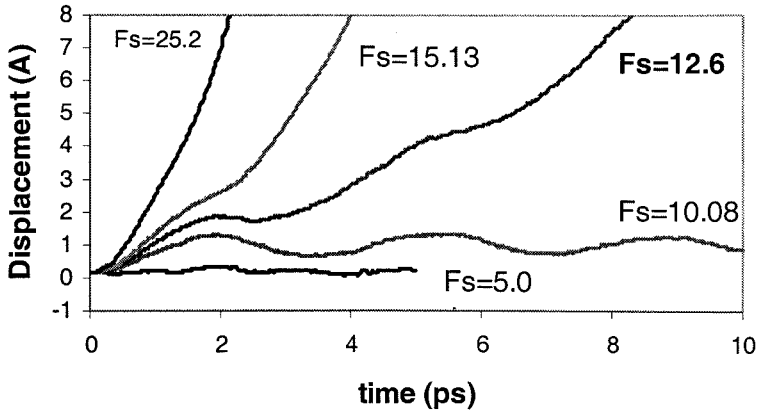

(a)

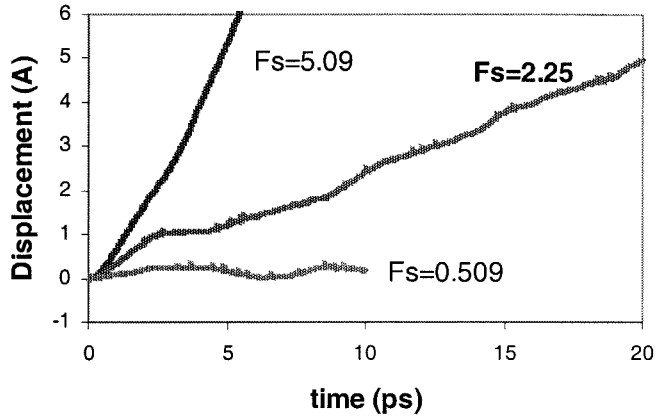

(b)

Figure 7-5 Relative displacement in x direction between upper and lower slabs for Ni(100)/Ni(100) random rough interface. (a) for θ=0° aligned case, Fc=12.6 (b) for θ=45° misorientation interface, Fc=2.25.

Figure 7-6 shows a snapshot of the atomic structure of the systems whose motion behavior is plotted in Figure 7-5 for the rough Interface. Upper curve is for θ=45° misorientation with an applied force of F_s=2.25 after 10ps. Lower curve is for perfect

alignment (θ=0°) with F_s=12.6 after 6ps. In both cases, the rough surface leads to disordering, even for θ=45°.

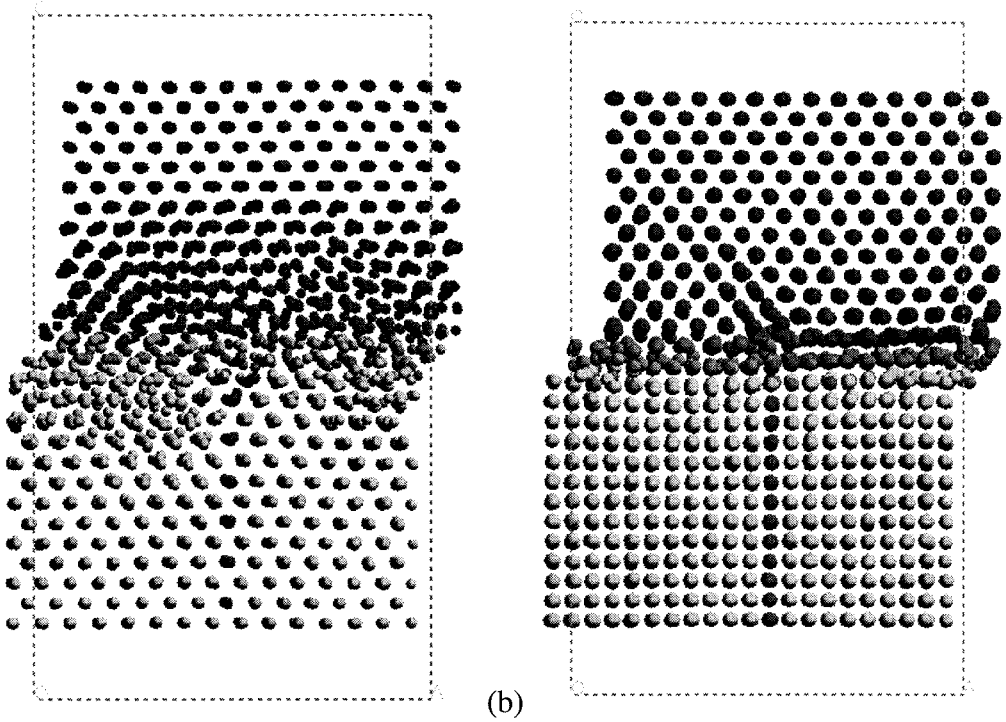

Figure 7-6 Snapshot of atomic structures of the sliding systems with Ni(100)/Ni(100) random rough interface, whose performances are plotted in Figure 7-5. (a) for perfect alignment (θ=0°) with applied force Fs=12.6 after 6ps; (b) for θ=45° misorientation with Fs=2.25 after 10ps.

7.3.3 Temperature effects

From the structure after the friction simulation, we see the middle layers are actually highly disordered (melting probably). A new simulation was done to use Hoover constant temperature method [7-9] control temperature for all the atoms in the system. This method is compared to the previous method where the atoms at the

interface (about 1 layer of atom on both slabs) are free to move and raise temperature and the atoms in the rigid layers are fixed at a constant temperature. Figure 7-7 showed three models; all have two pieces material perfectly aligned (θ=0°). The top dark line corresponds to a model, which has a step on the surface (step rough interface) and no temperature control on the atoms at the interface. The second light line comes from a model, which has 25% of atoms at interface randomly deleted (random rough) and also no temperature control on interface. The bottom line corresponds to the model, which has temperature control over all the system and a step on the interface as well. The model with interface temperature fixed at 300K has a slower relative motion or a larger friction than the model with interface subject to adiabatic heating. This suggests that the temperature at the interface is very high in the first two models and helps the motion of sliding. More studies should be done on how to damp the thermal energy at the interface, which is an important factor of getting accurate friction coefficient. In our model, the heating up of the interfacial atoms may cause the temperature gap between the bulk region with fixed temperature and the fully relaxed interface region. A temperature gradient should be added to the later, according to the heat conductivity of the materials.

We also observed that different rough surface configurations with the no surface temperature controlling lead to similar motion behavior and similar frictional behavior. Thus, only one random rough surface structure is discussed in this study.

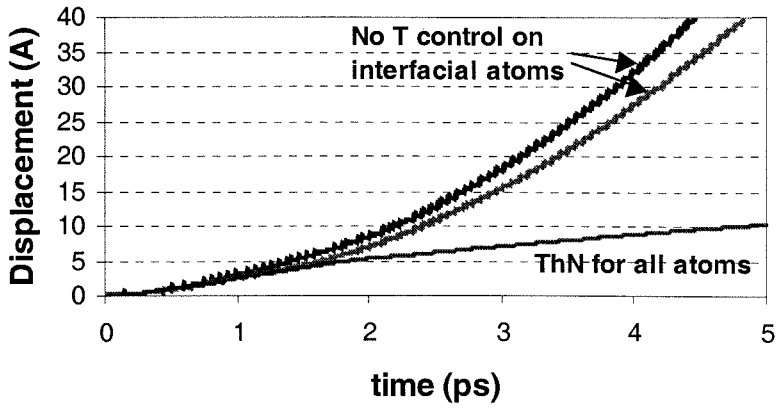

Figure 7-7 Displacement in different models to show the effects of temperature damping. The top two lines are from two models, where no temperature control on the interface atoms (about 1 layer of atoms on both slabs), or the interface, is subject to adiabatic heating. The top dark line corresponds to a model, which has a step rough interface, and the second light line comes from a model with random rough interface. The lowest line corresponds to simulation under Hover temperature damping over all the system, and the interface is step rough. The interface subject adiabatic heating leads to faster motion of two slabs or lower friction.

7.4 Discussion

7.4.1 Static friction coefficients

We found in the perfect alignment cases (θ=0°), both on flat and rough surface, below the Fc, there are oscillatory motion, but no such oscillation exists in the θ=45° misorientated sliding. Also as the applied force equals the critical force, Fc, there is a barrier at the beginning of motion (similar to the first peak in the oscillation) in the

θ=0° case but not in the θ=45° case. This is similar to the observation of "stick-slip" behavior in θ=0° sliding, but only slip motion in θ=45° sliding in experiments. The reason might be the lack of periodicity on the misorientated interface.

For the static frictional coefficients, with perfect atomic flat interface, simulations lead to $\mu \sim 14$ for θ=0°, $\mu \sim 0.04$ for θ=30°, and $\mu \sim 0.4$ for θ=45°. The static friction coefficient on flat misoriented interfaces (for both θ=30° and θ=45° cases) is very low compared to 0 degree alignment case, which agrees well with the analytic theories, which states that there is no static friction (close to zero in our simulation) on clean incommensurate interfaces.

However, the anisotropy behavior of static μ on clean flat Ni(100)/Ni(100) interface is not in agreement with the experiments by Gellman and Ko. The simulation has shown that on rough interface, the static frictional coefficients are $\mu \sim 17$ for θ=0°, $\mu \sim 13$ for θ=30°, and $\mu \sim 4$ for θ=45°. These results show that the roughness on the surface increases the static friction coefficient on misoriented surface at least by a factor of 10, but does not increase the value in the commensurate interface. And the static friction coefficient doesn't vanish on incommensurate interfaces (θ=30° and θ=45°); however, θ=45° does show minimum static friction coefficient. Even tough Gellman and Ko have shown that no impurities existed on the surface (as measured by AES) and the surfaces were well ordered (as measured by LEED), in the ultrahigh vacuum environment, the mechanical polished surface was not atomic flat, and plastic deformation can occur during dry sliding as well. Therefore, we believe the surface roughness and the disordering and other plastic

deformations caused during dry sliding are the main reasons for the observed anisotropy behavior on Ni(100)/Ni(100) interface.

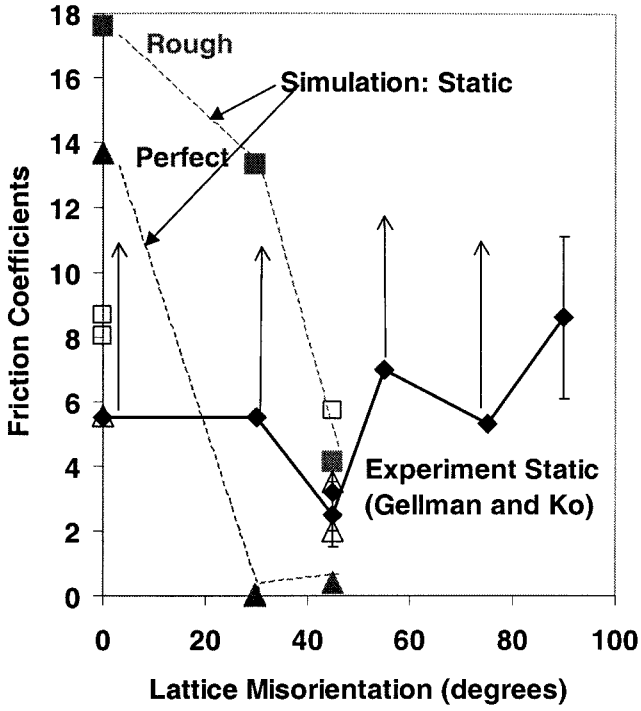

Figure 7-8 Friction coefficient as a function of the lattice misorientation angle between two Ni(100) surfaces. Solid diamonds are the experimental static friction coefficients measured by Gellman and Ko; the point and upward arrows represent the lower limit of the values. The solid symbols are static friction coefficients from simulation, and open symbols are dynamic friction coefficients. Squire patterns are for flat interface, and triangles are for rough interface.

The comparison between all MD calculations and the experimental data are plotted in Figure 7-8. Even the simulation results are not exactly the same as the experimental values; the anisotropy behavior as a function of misorientation angle are

similar. We could define the anisotropy factor as the ratio between the friction coefficients for misorientated interface and perfect aligned interface. Therefore, the experimental static anisotropy factor for θ=45° is 2.5±1 / 8.6±2.5 = 13% ~57% and for θ=30° is 5.5+ / 8.6±2.5 = 49%~92%. In our simulation, the static friction coefficients anisotropy factor on rough surface is 4.11/17.6 = 23% for θ=45° and 13.3/17.6 = 75% for θ=30°, all full into the range of experimental results. However, the static anisotropy factor on flat surface is 0.4/13.7 = 3% for θ=45° and 0.04/13.7=0.3% for θ=30°. The roughness increases the static anisotropy factor dramatically and close to experimental measurements. This implies another model of the origin of static friction: the roughness, disorder, and the plastic deformation on the interface can increase the static friction in the macroscopic objects.

7.4.2 Dynamic friction coefficients

In the experiments, the dynamics friction coefficient were also obtained but not reported in the paper. However, the authors said it would not change the overall conclusions from static frictional coefficient, regarding the orientation dependence of friction. In our simulation we calculated that for θ=0° the dynamic friction coefficients lead to μ_d ~ 5.5 for the flat surface and μ_d ~ 8.3 for the rough surface; whereas for the dynamic θ=45° case, we obtain μ_d ~ 2.5 for the flat surface and μ_d ~ 5.7 for the rough surface. The simulation values are comparable to the experimental values of μs ~ 8.5±2.5 for the θ=0° case and μs ~ 2.5±1 for the θ=45° case. The dynamic friction coefficient is 2.5/5.5 = 45% for θ=45° on flat surface, and is

5.7/8.3=68% on rough surface. Indeed, the factor of two drop in friction coefficient from $\theta=0°$ to $\theta=45°$ observed experimentally is captured by the dynamics calculations for the perfect case.

The close correspondence between the dynamic values from simulation with the "static" values for the experiments is tantalizing. We speculate that the experimental surfaces are probably more like our slightly disordered surfaces after doing the dynamic. This suggests that the experimental surface might have disorder and other plastic deformation in the top layer, just as we find in the dynamics sliding. We believe that disorder in just the top layer might still be compatible with the sharp LEED pattern observed experimentally. This suggests that in the simulation the surface must be rubbed (polished) to obtain surface like experimental "smooth surface." If so, then perhaps the theory and experiment are compatible. We plan to test this hypothesis in the future.

7.5 Conclusions

We illustrated the atomistic approach to tribology of metal surfaces by determining the friction for Ni(001)/Ni(001) interface as a function of misorientation angle. These results suggest that the roughness on the surface will increase the static friction coefficients on clean incommensurate Ni interface, not on commensurate interface, such that it explained the difference between the experimental results and the analytical models of less misfit angle's anisotropy dependence of static friction coefficients. Some degree of plastic deformation also occurs on the interface even for careful experiments on clean samples.

References:

[7-1] B. N. J. Persson, Sliding Friciton: Physical Principles and Applications, Springer (1998)

[7-2] Y. I. Frenkel and T. Kontorova, Zh. Eksp. Teor. Fiz. **8**, 1340, (1938), K. Shinjo and M. Hirano, Surf. Sci. **283**, 473, (1993)

[7-3] M. O. Robbins and E. D. Smith, Langmuir **12**, 4543, (1996)

[7-4] J. S. Ko and A. J. Gellman, Langmuir **16**; 8343 (2000)

[7-5] M. Hirano, K. Shinjo, R. Kaneko and Y. Murata, Phys. Rev. Lett. **67**, 2642 (1991)

[7-6] G. He, M. H. Muser and M. O. Robbins, Science **284**, 1650 (1999)

[7-7] T. Cagin, Y. Qi H. Li, Y. Kimura, H. Ikeda, W. L. Johnson and W. A. Goddard, III, Bulk Metallic Gasses, MRS Symp. Processing **554**, 43 (1999)

[7-8] Y. Qi, T. Cagin, Y. Kimura and W. A. Goddard III, Phys. Rev. B **59**, 3527 (1999); also A. P. Sutton and J. Chen, Phil. Mag. Lett. **61**, 139 (1990); H. Rafii-Tabar and A. P. Sutton, Phil. Mag. Lett. **63**, 217 (1991)

[7-9] W. G. Hoover, Phys. Rev. A **31**, 1695 (1985)

[7-10] J. R. Smith, G. Bozzolo, A. Banerjea and J. Ferrante, Phys. Rev. Lett. **63**, 1269 (1989)